Transfer matrix approach to thermodynamics and dynamics of one-dimensional quantum systems

Dissertation

zur Erlangung des Grades eines
Doktors der Naturwissenschaften
der Abteilung Physik
der Universität Dortmund

vorgelegt von
Jesko Sirker

Oktober 2002

Tag der mündlichen Prüfung	6. Dezember 2002
Vorsitzender und Prodekan	Prof. Dr. K. Wille
1. Berichterstatter	Prof. Dr. A. Klümper
2. Berichterstatter	Prof. Dr. W. Weber
Vertreter der promovierten wissenschaftlichen Mitarbeiter	Dr. K. Wacker

Contents

Chapter 1

Introduction

The last two decades have witnessed an emerging interest in the study of *strongly correlated electron systems* [1,2]. In such systems the Coulomb repulsion between the electrons is so strong that they cannot be considered separately. Instead the strong microscopic interactions lead to a macroscopic ensemble showing collective properties. This is quite different from the very successful standard model for metals, Landau's Fermi liquid theory, where the interacting model is continuously connected with the non-interacting, free fermion system. Low-energy properties of such a Fermi liquid are described by *independent quasiparticles* formed by electrons and holes in the vicinity of the Fermi wavevector and the interactions are only visible in a renormalization of the masses. The challenge to understand and describe also strongly correlated systems has moved into the center of interest in condensed matter physics due to the synthesization of a variety of transition metal oxides, organic metals and carbon based compounds showing strong correlation effects and new unexpected physical properties. Among these, the discovery of high-T_c superconductivity in the cuprates by Bednorz and Müller [3] in 1986 has been of fundamental importance. Although some basic properties of these materials have been identified shortly afterwards [4], a unified theory is still lacking. The parent compound of a cuprate superconductor is always a *Mott insulator* and superconductivity is created by doping. Whereas conductivity is blocked in a conventional insulator by Pauli's exclusion principle when the highest occupied band contains two electrons per unit cell, conduction in a Mott insulator is blocked instead by the Coulomb repulsion of the electrons. This occurs if the highest occupied band contains one electron per unit cell so that transport is only possible by creating double occupied sites. A strong enough repulsion can prevent that and splits the band into a filled lower and an empty upper band. The most important difference from a conventional insulator is that internal degrees of freedom such as spin and orbital remain still active. These are exactly the degrees of freedom being discussed in chapter 6 of this thesis. By adding holes to a Mott insulator, conductivity is restored because electrons can hop without involving double occupied sites. A model describing this situation is the t-J model discussed in chapter 5.

Another essential feature of the high-T_c superconductors is that the key structural unit is a CuO_2 plane and the interplane coupling is always very weak. Such *low-dimensional systems* with strong correlations are interesting from a general point of view, because their behaviour is most strongly affected by quantum effects. Mermin, Wagner and Hohenberg have shown for example that at finite temperature the fluctuations in a spin model around a ground state with ferromagnetic or antiferromagnetic long range order are in one and two dimensions too large to let such a state undestroyed [5,6]. The argument is applicable very generally; it depends on the density of states $\rho(\omega)$ of such fluctuations at low energies

ω:

$$\rho(\omega) \propto \omega^{(D-2)/2} \qquad \text{(D: dimension)}$$

As a consequence, correlation functions in such one- and two-dimensional systems are decaying exponentially $\sim \mathrm{e}^{-r/\xi}$ at finite temperature with a certain *correlation length* ξ. Apart from the CuO_2 planes in the cuprates many other compounds consisting of low-dimensional structures, like e.g. $CuGeO_3$ (spin chains), NaV_2O_5 (quarter filled ladders), $(VO)_2P_2O_7$ (dimerized spin chains or ladders) or YVO_3, where the interesting spin-orbital physics is constrained to chains in a more subtle way discussed in chapter 6.1, are known. This has led to a very fruitful interplay between theory and experiment.

One reason why high-T_c superconductivity is still an unsolved problem is that two-dimensional models are very hard to tackle analytically as well as numerically. In two dimensions there is a delicate balance between order and fluctuation. Although order can occur at $T = 0$, this order is often very sensitive to a small change in parameters leading to neighbouring ground states with different order parameters. If the *quantum phase transition* between these competing states is second order, the point separating the two phases is called a *quantum critical point* [7] characterized by a vanishing energy scale and a diverging characteristic length scale ξ. In one dimension (1D) the quantum fluctuations are so strong that they often preclude long-range order even at zero temperature. Nevertheless, the situation becomes easier because some quantum models exist which are exactly solvable by Bethe ansatz (BA) [8], including for example the fundamental Heisenberg, Hubbard, supersymmetric t-J and Kondo lattice model. However, it is often necessary and interesting to consider additional couplings (e.g. spin-phonon coupling, spin-orbit coupling, anisotropies, frustration) which destroy integrability. In such cases one needs approximate methods even in one dimension. In many analytical approaches, the so called *field theoretical methods*, the lattice model is replaced by a continuum model, which is permitted if $\xi \gg a_0$ with a_0 being the lattice constant. A big step forward in understanding strongly correlated systems and quantum critical phenomena has been the *renormalization group* (RG) invented by Wilson [9] and others in the seventies. The idea is to change the scale of the system in real or momentum space by certain transformations making it possible to access a critical point (non-trivial fixed point of the RG), where the correlation length ξ diverges, in a controlled way. Other important analytical methods include for example bosonization, conformal field theory (CFT), (modified) spin-wave and dynamical mean-field theory (DMFT).

A complementary possibility are numerical methods, which act on a lattice and therefore have the obvious advantage that lattice effects are not disregarded as in the field theoretical approach. To proceed numerically in a straightforward way, one has to write down the Hamiltonian for a linear system of length L in matrix form and to diagonalize this matrix on a computer. However, this method is restricted to relatively small systems because the size of the Hilbert space is increasing $\sim n^L$ with n being the dimension of the local Hilbert space. In practical computations the maximal system size is given today by $L \sim 16$ for a system with a two-dimensional local Hilbert space (e.g. spin-1/2 system).[1] One way to

[1] If only a few leading eigenvalues and not the complete spectrum are needed, it is possible to diagonalize

proceed to much longer systems is a truncation of the Hilbert space so that only the "most important states" are kept. After first successes for the Kondo model by Wilson using the so called numerical renormalization group (NRG) [10] where the m lowest eigenstates are retained in each RG step, it turned out that this truncation scheme depends on the special energy spectrum of the impurity problem in the representation Wilson has used and that it is not applicable for other 1D systems. A different way to truncate the Hilbert space has been proposed by White [11] who has used a *reduced density matrix* to choose the states in an optimal way. This *density matrix renormalization group* (DMRG) is today one of the most popular numerical methods to calculate ground-state properties and has successfully been applied to various 1D systems.

Although ground-state properties of 1D systems are an interesting task including quantum critical points (QCP) and quantum phase transitions, properties at non-zero temperature are of equal interest on their own. Topics which can be investigated include the behaviour of a system near a QCP, the transition from the high-T lattice into the quantum critical regime with temperature, entropy effects giving rise to various kinds of instabilities and the direct comparison with experiment which is also done at finite temperature. The field theoretical methods mentioned before are restricted to low temperatures where $\xi \gg a_0$ remains valid so that the calculation of thermodynamic quantities over a wide temperature range is only possible by BA in exactly solvable models or otherwise by numerical methods. The numerical methods - and one way to calculate thermodynamics by BA as well [12] - are based on the equivalence of a D-dimensional quantum system to a $D+1$-dimensional classical system. One of the most popular methods being applicable in principle in any dimension D is the *quantum Monte Carlo* (QMC) algorithm. In a first step a *Trotter-Suzuki decomposition* [13, 14, 15] and path-integral formulation in imaginary time τ is performed leading to a classical model on a lattice where the imaginary time is discretized in steps $\Delta\tau = \beta/M$ with β being the inverse temperature and M the so called *Trotter number*. On this lattice a sequence of configurations $\mathcal{C}$ is constructed such that in the limit of infinitely many configurations their distribution agrees with the correct Boltzmann distribution. Thermal averages of observables are obtained by a summation over the values $\mathcal{O}(\mathcal{C})$ of the observable $\mathcal{O}$ in the configuration $\mathcal{C}$ with the corresponding weight $W(\mathcal{C})$

$$\langle \mathcal{O} \rangle = \frac{1}{Z} \sum_{\{\mathcal{C}\}} W(\mathcal{C}) \mathcal{O}(\mathcal{C}) \ ,$$

where Z is the partition function. There exist many different update algorithms to proceed from a given configuration $\mathcal{C}$ to a new configuration $\mathcal{C}'$. The general principle is that a new configuration is proposed which differs by small local changes from $\mathcal{C}$ and that this configuration is accepted with a certain probability. One problem of QMC is that the weights $W(\mathcal{C})$ can take negative values ("negative sign problem"), which leads to a cancellation of positive and negative Monte Carlo samples and therefore to an exponential blow-up of the statistical errors when increasing the system size L and the inverse temperature β with fixed computational effort, especially for fermionic systems. Thus, in these cases QMC is often restricted to relatively small systems and high temperatures.

chains with $L \sim 40$ by applying the Lanczos or Davidson algorithm.

An alternative approach to calculate thermodynamic properties of 1D quantum systems is the *transfer-matrix DMRG* (TMRG), the method applied in the present thesis. This method has been proposed by Bursill *et al.* [16], has been significantly improved by Wang, Xiang [17] and Shibata [18] and extends the DMRG to finite temperatures. Analogous to QMC the quantum system is mapped to a two-dimensional classical system, where the second axis corresponds to a discrete imaginary time (inverse temperature) $\Delta\tau = \beta/M$. In a second step a so called *quantum transfer matrix* (QTM) for a fixed Trotter number M is formulated, which evolves along the spatial direction. The free energy and therefore the whole thermodynamics in the **exact thermodynamic limit** $L \to \infty$ is given solely by the largest eigenvalue of the transfer matrix. The DMRG algorithm is used to extend the transfer matrix in imaginary time direction (being equivalent to a decrease in temperature) with a fixed number of retained Hilbert space states. Compared to QMC, this method has the advantage of never suffering under the negative sign problem making it possible to calculate thermodynamic quantities also for fermionic systems. Additionally, the obtained results directly describe a system with infinite length. As a disadvantage one should mention that TMRG is not directly extendable to higher dimensional systems.

In chapter 2 the TMRG method is described in detail. Especially a novel Trotter-Suzuki mapping is proposed which has several advantages compared to the traditional (checkerboard-like) decomposition, which has been known for a long time and widely used in TMRG and QMC. Aspects concerning the numerical part are presented in chapter 3. To check the accuracy of the 2 algorithms, where one is based on the traditional checkerboard decomposition and the other on the novel mapping, and to show how powerful the method is, numerical data are compared with exact results in chapter 4. Here also the sources for numerical errors are studied in detail. In chapter 5 the one-dimensional t-J model at arbitrary temperature and filling is considered. 1D systems with interacting fermions are interesting from a theoretical and experimental point of view: theoretically it is known that interacting fermions in 1D are not described by Landau's theory of Fermi liquids, instead they represent what is called a Luttinger liquid [19]. Such systems show e.g. a power-law singularity at the Fermi level instead of a step-like singularity, no quasi-particle pole in the one-particle Green's function and a spin-charge separation. Some predictions of Luttinger liquid and conformal field theory are tested numerically. Another reason why the t-J model is of great interest is that it describes presumably the basic interactions in the copper oxygen planes of high-T_c superconductors and results for the 1D case may give hints for the 2D case. Furthermore, there exist also quasi 1D compounds with charge degrees of freedom (e.g. $Sr_{14-x}Ca_xCu_{24}O_{41}$, so called "telephone-number compounds") [20] which can be described by modified t-J models.
Whereas in most insulators the distribution of electrons around every atom is frozen in at the melting point and changes little down to zero temperature, there exist low-lying electronic states (termed "orbitals") in some transition metal oxides making it necessary to consider spin and orbital degrees of freedom on an equal footing [21]. In chapter 6.1 such a spin-orbital model is treated which is relevant for cubic vanadates [22]. After deriving the effective model with spin $S = 1$, results from numerical calculations for the 1D case are shown and their implications for the high-temperature phase of YVO_3 are discussed by taking also the interchain couplings into account. It turns out that almost

all experimentally observed properties can be explained semi-quantitatively within the considered 1D model. Another spin-orbital model with $S = 1/2$ is discussed in chapter 6.2. As a special point in parameter space this includes the SU(4) symmetric model which has 3 gapless excitations. Predictions by CFT and RG calculations [23, 24] are tested numerically. Additionally, the effect of symmetry breaking by marginal operators is studied, which leads to "spin-orbital separation" in analogy to spin-charge separation in a Tomonaga-Luttinger liquid.

A conceptional new approach to directly calculate real-time correlation functions at finite temperature is introduced in chapter 7. This resolves at least partly a fundamental problem of QMC and TMRG calculations: Because these methods act on a classical lattice the obtained correlation functions depend usually on imaginary time. Whereas it is possible to perform an analytical continuation to real times for exact results, this leads to an exponentially ill-posed problem if numerical errors are present and therefore to unreliable results. The novel approach is based on 2 independent Trotter-Suzuki mappings for temperature and real time and therefore eludes an analytic continuation. To test the approach, the longitudinal spin autocorrelation function in the XXZ-model at infinite temperature is considered in section 7.1. This provides not only a simple test, it is indeed an interesting problem on its own. In the last chapter a brief summary and outlook is given.

Publications based on this thesis:

J. Sirker, A. Klümper and K. Hamacher, *Ground-state properties of two-dimensional dimerized Heisenberg models*, Phys. Rev. B **64**, 134409 (2002).[2]

J. Sirker, A. Klümper, *Temperature driven crossover phenomena in the correlation lengths of the one-dimensional t-J model*, Europhys. Lett. **60**, 262 (2002).

J. Sirker, A. Klümper, *Thermodynamics and crossover phenomena in the correlation lengths of the one-dimensional t-J model*, Phys. Rev. B, in print (2002).

J. Sirker, G. Khaliullin, *Entropy driven dimerization in a one-dimensional spin-orbital model with* $S = 1$, submitted to Phys. Rev. Lett. (2002).

C. Ulrich, G. Khaliullin, J. Sirker, M. Reehuis, M. Ohl, S. Miyasaka, Y. Tokura and B. Keimer, *Orbital Peierls state in a magnetic insulator*, to be resubmitted to Phys. Rev. Lett. (2002).

[2]The numerical method presented here has been used in parts of this publication, however, the topic itself is not part of the thesis.

Chapter 2

Density Matrix Renormalization Group for Transfer Matrices (TMRG)

In general all thermodynamic quantities for a D-dimensional quantum system can be derived from the partition function

$$Z = \mathrm{Tr}\ \mathrm{e}^{-\beta H} = \sum_n \mathrm{e}^{-\beta E_n} \ , \tag{2.1}$$

where H is the Hamilton operator and E_n the corresponding eigenvalues. So to proceed in a straightforward way, one has to diagonalize the Hamiltonian of a given system. Although this is possible in 1D for certain models by Bethe ansatz, it is even in these cases difficult to study thermodynamic properties analytically. For other models which have to be diagonalized numerically this direct way is hopeless because the dimension of the Hilbert space increases exponentially with the system size. An alternative approach is given by the Trotter-Suzuki decomposition [13,14,15], where the D-dimensional quantum system is mapped onto a $D+1$-dimensional classical model (see Fig. 2.1). The classical model can be solved by formulating an appropriate transfer matrix.

2.1 The transfer matrix formalism

To introduce the transfer matrix concept we will first consider a very simple classical model, the ferromagnetic Ising chain

$$H = -J \sum_{i=1}^{L} \sigma_i^z \sigma_{i+1}^z - h \sum_{i=1}^{L} \sigma_i^z \tag{2.2}$$

with coupling $J > 0$ of Ising spins $\sigma^z = \pm 1$ in a magnetic field h where we assume periodic boundary conditions. The partition function for this model is given by

$$Z = \sum_{\{\sigma_i^z\}} \prod_{i=1}^{L} T_1(\sigma_i^z, \sigma_{i+1}^z) T_2(\sigma_i^z) \ , \tag{2.3}$$

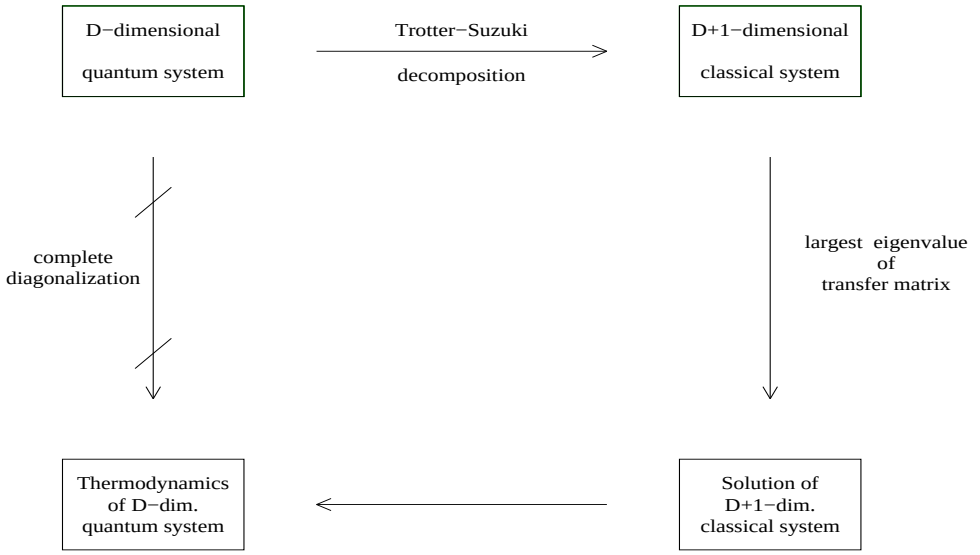

Figure 2.1: The figure shows the alternative way to calculate thermodynamics of a D-dimensional quantum system.

where $T_1(\sigma_i^z, \sigma_{i+1}^z) = \exp(\beta J \sigma_i^z \sigma_{i+1}^z)$ and $T_2(\sigma_i^z) = \exp(\beta h \sigma_i^z)$. The "trick" is now to interpret the two possible values of σ_i^z as index labeling the rows and columns of a 2×2-matrix [25]. This leads to

$$T_1 = \begin{pmatrix} \mathrm{e}^{\beta J} & \mathrm{e}^{-\beta J} \\ \mathrm{e}^{-\beta J} & \mathrm{e}^{\beta J} \end{pmatrix} \quad , \quad T_2 = \begin{pmatrix} \mathrm{e}^{\beta h} & 0 \\ 0 & \mathrm{e}^{-\beta h} \end{pmatrix} \tag{2.4}$$

and the partition function is converted into a trace over a matrix product

$$Z = \mathrm{Tr}\,(T_1 T_2)^L = \mathrm{Tr}\,(T_2^{1/2} T_1 T_2^{1/2})^L = \epsilon_1^L + \epsilon_2^L \tag{2.5}$$

where $T_1 T_2$ or the symmetrized form $T_2^{1/2} T_1 T_2^{1/2}$ is called a *transfer matrix*. Here ϵ_1 and ϵ_2 are the eigenvalues of the symmetric matrix

$$T_2^{1/2} T_1 T_2^{1/2} = \begin{pmatrix} \mathrm{e}^{\beta(J+h)} & \mathrm{e}^{-\beta J} \\ \mathrm{e}^{-\beta J} & \mathrm{e}^{\beta(J-h)} \end{pmatrix} , \tag{2.6}$$

which are given by

$$\epsilon_{1,2} = \mathrm{e}^{\beta J} \cosh(\beta h) \pm \sqrt{\mathrm{e}^{2\beta J} \sinh^2(\beta h) + \mathrm{e}^{-2\beta J}} \, . \tag{2.7}$$

For zero magnetic field this simplifies to $\epsilon_1 = 2\cosh(\beta J)$ and $\epsilon_2 = 2\sinh(\beta J)$. The free energy density f at temperature T is therefore given by

$$f = -\frac{T}{L} \ln Z = -\frac{T}{L} \ln(\epsilon_1^L + \epsilon_2^L) \, . \tag{2.8}$$

For simplicity, we consider only $h = 0$ and perform the thermodynamic limit $L \to \infty$:

$$\begin{aligned} f &= -\frac{T}{L}\ln\{2^L[\cosh^L(\beta J) + \sinh^L(\beta J)]\} \\ &= -\frac{T}{L}\ln\{2^L \cosh^L(\beta J)[1 + \underbrace{\tanh^L(\beta J)}_{\substack{L\to\infty \\ \longrightarrow 0}}]\} \\ &\overset{L\to\infty}{\longrightarrow} -T\ln\{2\cosh(\beta J)\} = -T\ln\epsilon_1 \ . \end{aligned} \tag{2.9}$$

The free energy in the thermodynamic limit is determined solely by the largest eigenvalue of the transfer matrix.

Next, we will calculate the two-point spin correlation function

$$\left\langle \sigma_i^z \sigma_j^z \right\rangle = \frac{1}{Z}\sum_{\{\sigma_i^z\}} \sigma_i^z \sigma_j^z \mathrm{e}^{-\beta H} \ , \tag{2.10}$$

which can be formulated again as a trace over a matrix product

$$\left\langle \sigma_i^z \sigma_j^z \right\rangle = \frac{1}{Z}\mathrm{Tr}\left(T_1^i \sigma^z T_1^{j-i} \sigma^z T_1^{L-j} \right) \ . \tag{2.11}$$

In the basis where T_1 is diagonal (eigenstates of σ^x), we find

$$\left\langle \sigma_i^z \sigma_j^z \right\rangle = \frac{1}{Z}\mathrm{Tr}\left\{ \begin{pmatrix} \epsilon_1^i & 0 \\ 0 & \epsilon_2^i \end{pmatrix} \begin{pmatrix} 0 & 1 \\ 1 & 0 \end{pmatrix} \begin{pmatrix} \epsilon_1^{j-i} & 0 \\ 0 & \epsilon_2^{j-i} \end{pmatrix} \begin{pmatrix} 0 & 1 \\ 1 & 0 \end{pmatrix} \begin{pmatrix} \epsilon_1^{L-j} & 0 \\ 0 & \epsilon_2^{L-j} \end{pmatrix} \right\} \tag{2.12}$$

leading to

$$\left\langle \sigma_i^z \sigma_j^z \right\rangle = \frac{\epsilon_1^{L-j+i}\epsilon_2^{j-i} + \epsilon_2^{L-j+i}\epsilon_1^{j-i}}{\epsilon_1^L + \epsilon_2^L} \ . \tag{2.13}$$

In the thermodynamic limit $L \to \infty$ this simplifies to

$$\left\langle \sigma_i^z \sigma_j^z \right\rangle = \left(\frac{\epsilon_2}{\epsilon_1}\right)^{j-i} = \tanh^{j-i}(\beta J) \tag{2.14}$$

or by defining $r = ja_0$ with a_0 being the lattice constant

$$\langle \sigma^z(0)\sigma^z(r)\rangle = \mathrm{e}^{-|r|/\xi} \tag{2.15}$$

with the *correlation length*

$$\frac{1}{\xi} = \frac{1}{a_0}\ln\left(\frac{\epsilon_1}{\epsilon_2}\right) = \frac{1}{a_0}\ln\coth(\beta J) \ . \tag{2.16}$$

The correlation length ξ is determined by the ratio of leading to next-leading eigenvalue of the transfer matrix.

From Eq. (2.16) we see that $\xi/a_0 \sim \exp(2\beta J)/2 \gg 1$ for $\beta J \gg 1$. Only in this situation

are continuum descriptions allowed and do the concepts of scaling and universality become useful.[1]

Now we will discuss more generally how a 1D quantum system is transformed to a 2D classical system and how an appropriate transfer matrix can be chosen to solve the classical model. However, it will turn out that the Ising model is an extremely useful toy model and the derived results remain more or less valid. Starting point is an arbitrary Hamiltonian H of a 1D quantum system with length L, periodic boundary conditions and nearest-neighbour interactions

$$H = \sum_{i=1}^{L} h_{i,i+1} \; . \tag{2.17}$$

First, we want to discuss the more traditional mapping which was suggested by Suzuki [15] and then applied to various systems to perform QMC or TMRG calculations (see X. Wang and T. Xiang in [26]). The Hamilton operator in Eq. (2.17) is decomposed into a part which contains the interactions starting on an even site (H_e) and another part which contains the interactions starting on an odd site (H_o). By discretizing the imaginary time, the partition function is given by

$$Z = \mathrm{Tr}\, \mathrm{e}^{-\beta H} = \lim_{M\to\infty} \mathrm{Tr} \left\{ \left[\mathrm{e}^{-\epsilon H_e} \mathrm{e}^{-\epsilon H_o} \right]^M \right\} \tag{2.18}$$

with $\epsilon = \beta/M$, β being the inverse temperature which is fixed here and M an integer Trotter number.[2] For a mapping with a finite ϵ one would expect an error of the order $\sim \mathcal{O}(\epsilon)$, but astonishingly the error is in fact only of the order $\sim \mathcal{O}(\epsilon^2)$ (see appendix A). By inserting $2M$ times the identity operator a *lattice path-integral representation* of the partition function is derived:

$$\begin{aligned} Z &= \sum_{\{s_k^i\}} \langle \alpha_1 | \, \mathrm{e}^{-\epsilon H_o} \, | \alpha_2 \rangle \, \langle \alpha_2 | \, \mathrm{e}^{-\epsilon H_e} \, | \alpha_3 \rangle \times \cdots \\ &\quad \times \langle \alpha_{2M-1} | \, \mathrm{e}^{-\epsilon H_o} \, | \alpha_{2M} \rangle \, \langle \alpha_{2M} | \, \mathrm{e}^{-\epsilon H_e} \, | \alpha_1 \rangle \end{aligned} \tag{2.19}$$

Here the state $|\alpha_k\rangle = |s_k^1\rangle \otimes |s_k^2\rangle \otimes \cdots \otimes |s_k^L\rangle$ with $k \in [1, 2M]$ and s_k^i being local basis states. Because H_o, H_e are sums of commuting terms we get

$$\exp(-\epsilon H_e) = \prod_{i=\mathrm{even}} \exp(-\epsilon h_{i,i+1}) \quad , \quad \exp(-\epsilon H_o) = \prod_{i=\mathrm{odd}} \exp(-\epsilon h_{i,i+1})$$

and the partition function becomes a matrix product

$$\begin{aligned} Z &= \sum_{\{s_k^i\}} \left(\tau_{1,2}^{1,2} \tau_{1,2}^{3,4} \cdots \tau_{1,2}^{L-1,L} \right) \left(\tau_{2,3}^{2,3} \tau_{2,3}^{4,5} \cdots \tau_{2,3}^{L,1} \right) \cdots \\ &\quad \left(\tau_{2M-1,2M}^{1,2} \tau_{2M-1,2M}^{3,4} \cdots \tau_{2M-1,2M}^{L-1,L} \right) \left(\tau_{2M,1}^{2,3} \tau_{2M,1}^{4,5} \cdots \tau_{2M,1}^{L,1} \right) \end{aligned} \tag{2.20}$$

[1] This will be discussed in more detail in chapter 5 on the basis of the t-J model.

[2] So $M \to \infty$ means also $\epsilon \to 0$.

where

$$\tau_{k,k+1}^{i,i+1} = \left\langle s_k^i s_k^{i+1} \right| \mathrm{e}^{-\epsilon H_{e,o}} \left| s_{k+1}^i s_{k+1}^{i+1} \right\rangle \tag{2.21}$$

is a local Boltzmann weight denoted in a graphical language by a shaded plaquette (see Fig. 2.2). The lower index represents the position in imaginary time whereas the upper index corresponds to the real space position. A possible choice for a transfer matrix is given by

$$\hat{T}_L = \left(\tau^{1,2}\tau^{3,4}\cdots\tau^{L-1,L}\right)\left(\tau^{2,3}\tau^{4,5}\cdots\tau^{L,1}\right) \tag{2.22}$$

with $Z = \operatorname{Tr}\hat{T}_L^M$. This transfer matrix evolves along the imaginary time direction (row-to-row transfer matrix). Because we want to perform the thermodynamic limit exactly and extend the transfer matrix numerically in imaginary time direction rather than in spatial direction, it is more convenient to rearrange the Boltzmann weights and to formulate a column-to-column transfer matrix (so-called *quantum transfer matrix* (QTM))

$$T_M = \left(\tau_{1,2}\tau_{3,4}\cdots\tau_{2M-1,2M}\right)\left(\tau_{2,3}\tau_{4,5}\cdots\tau_{2M,1}\right) = T_1\,T_2 \tag{2.23}$$

evolving along the spatial direction, so that the partition function is given by

$$Z = \operatorname{Tr} T_M^{L/2} = \sum_\mu \Lambda_\mu^{L/2} \tag{2.24}$$

with Λ_μ being the eigenvalues of T_M. This QTM for the classical model has checkerboard structure as shown in the left part of Fig. 2.2. It is also obvious from the graphical representation that the transfer matrix T_M is not symmetric. If T_1 and T_2 are symmetric and semi-positive, it is possible to symmetrize T_M analogously to the transfer matrix of the Ising chain (see Eq. (2.5)). However, this symmetrized form of the transfer matrix is useless for numerical computations because it involves additional matrix products and also enhances the computer memory space needed to store these matrices. Additionally the conditions stated above are often not fulfilled for physically interesting models (e.g. spin models with a nonzero magnetic field) and it is therefore impossible in these cases to symmetrize the transfer matrix. To determine eigenvalues and eigenvectors of non-symmetric matrices accurately is numerically much more complicated than for symmetric matrices which occur in ordinary DMRG calculations and is one of the main difficulties in TMRG algorithms. Details will be discussed in the next chapter.

The transfer matrix T_M for the classical model derived by the traditional mapping is unnecessarily wide as the repeat length of the classical system is 2. This leads to several disadvantages discussed in detail later on. Here we will introduce a novel Trotter-Suzuki mapping [27] where the partition function is expressed by

$$Z = \lim_{M\to\infty} \operatorname{Tr}\left\{\left[T_1(\epsilon)T_2(\epsilon)\right]^{M/2}\right\} \quad \text{with} \quad T_{1,2}(\epsilon) = T_{R,L}\exp\left[-\epsilon H + \mathcal{O}(\epsilon^2)\right] \tag{2.25}$$

instead of Eq. (2.18). $T_{R,L}$ are the right- and left-shift operators, respectively. Detailed calculations (see appendix A) show that the error of the mapping due to a finite ϵ is again only of the order $\sim \mathcal{O}(\epsilon^2)$ so that this mapping is a priori as well suited for numerical calculations as the traditional one. The received classical lattice has alternating rows

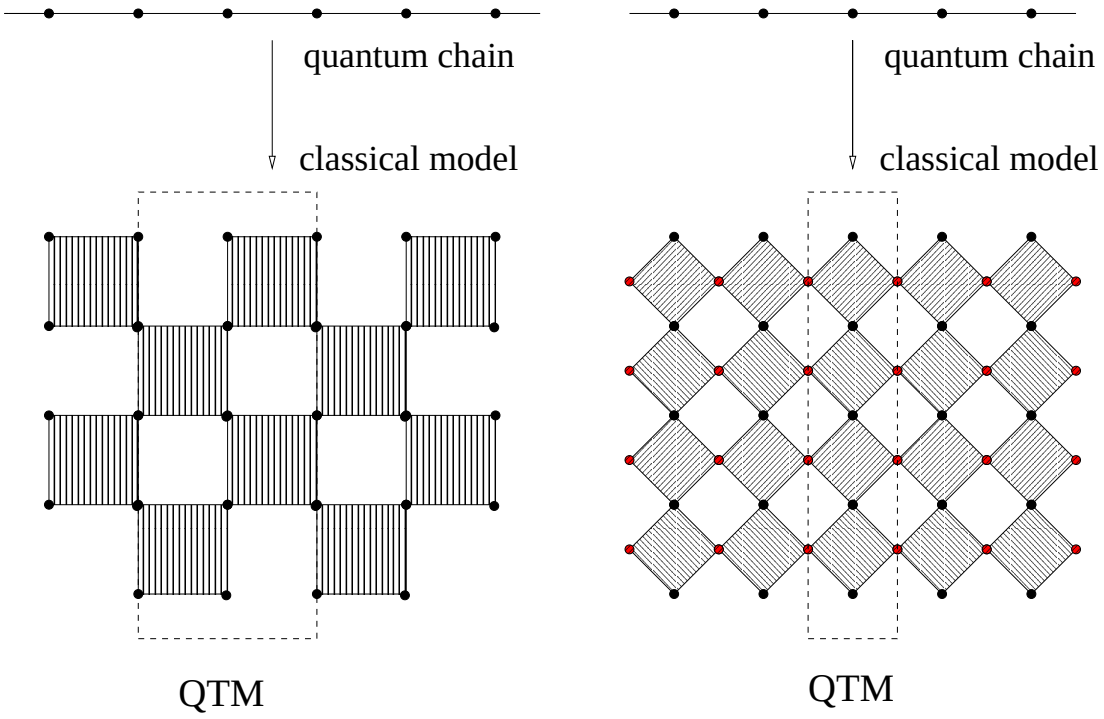

Figure 2.2: The left part shows the usual Trotter mapping of the 1D quantum chain to a 2D classical model with checkerboard structure where the vertical direction corresponds to imaginary time. All lattice points of the classical model belong to the physical lattice at different imaginary time steps and the QTM is a two-column transfer matrix. The right part shows the alternative mapping as described in the text. The classical model has alternating rows and additional lattice points in a mathematical auxiliary space. The QTM in this formulation is only one column wide. In both figures the shaded plaquettes denote the same Boltzmann weight.

and additional lattice points in a mathematical auxiliary space but allows to formulate a QTM which is only one column wide as shown in Fig. 2.2. The derivation of this QTM is completely analogous to the one given before and the shaded plaquettes in Fig. 2.2 denote the same Boltzmann weight. The partition function with this new QTM, $\tilde{T}_M$, is given by

$$Z = \mathrm{Tr}\, \tilde{T}_M^L = \sum_\mu \tilde{\Lambda}_\mu^L \; . \tag{2.26}$$

Next, we will investigate the spectra of the two QTMs at infinite temperature where a local Boltzmann weight reduces to (see Fig. 2.3)

$$\tau(s_1, s_2 | s_1', s_2') = \delta_{s_1,s_1'} \delta_{s_2,s_2'} \; . \tag{2.27}$$

As shown in Fig. 2.4 the relations

$$\begin{array}{rclcrcl} T_M^2 & = & n^2\, T_M & , & \tilde{T}_M & = & n\, \tilde{T}_M \\ \mathrm{Tr}\, T_M & = & n^2 & , & \mathrm{Tr}\, \tilde{T}_M & = & n \end{array} \tag{2.28}$$

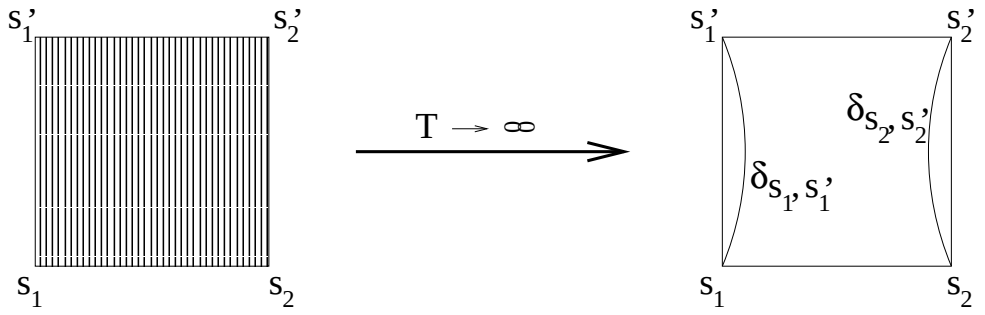

Figure 2.3: The Boltzmann weight (plaquette interaction) in the limit $T \to \infty$.

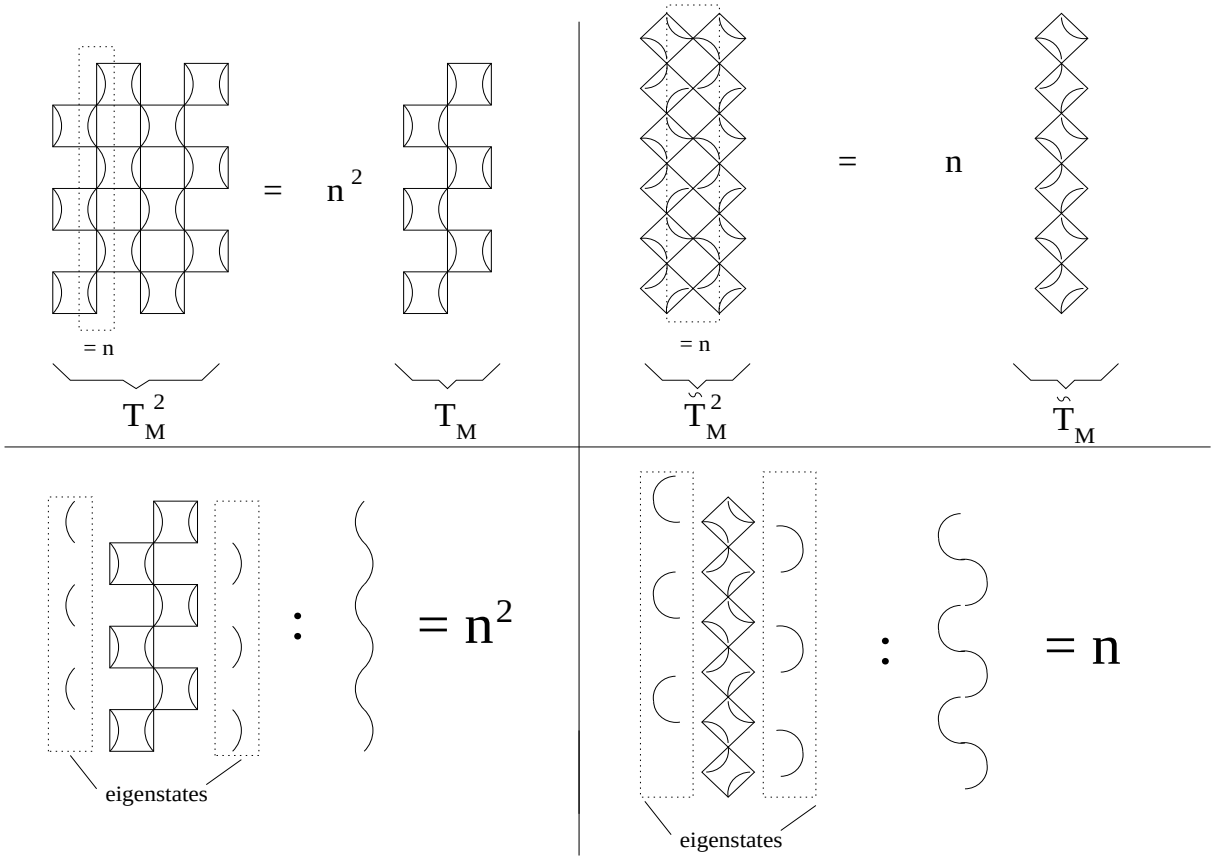

Figure 2.4: The relations for T_M^2 (upper part) and Tr T_M (lower part) are depicted graphically for the traditional QTM (left part) and the novel QTM (right part).

for the old QTM (left relations) and new QTM (right relations) are easy to prove. Here n denotes the number of possible values of the classical variable s_k^i. The upper relations lead to $\Lambda = n^2 \ \vee \ \Lambda = 0$ ($\Lambda = n \ \vee \ \Lambda = 0$) for the eigenvalues of the old (novel) QTM at infinite temperature, whereas the lower relations show additionally that the largest eigenvalue is given by $\Lambda_0 = n^2$ ($\Lambda_0 = n$) and all other eigenvalues are zero in both cases. The gap between the leading and next-leading eigenvalues of the QTM becomes smaller with decreasing temperature. However, we expect that the gap vanishes only at

zero temperature because a vanishing gap indicates a diverging correlation length (see Eq. (2.16) or (2.34)), i.e. a critical point or a certain kind of long range order which are expected to be present in a 1D quantum system only at zero temperature. This has been proved by Mermin and Wagner [5] for ferro- or antiferromagnetic order in 1D Heisenberg models. Therefore the free energy at non-zero temperature with fixed Trotter number M is determined in the thermodynamic limit solely by the largest eigenvalue of the QTM

$$\begin{aligned} f_{\infty,M} &= -T \lim_{L\to\infty} \frac{1}{L} \ln Z = -T \lim_{L\to\infty} \frac{1}{L} \ln \left\{ \sum_{\mu} \Lambda_{\mu}^{L} \right\} \\ &= -T \lim_{L\to\infty} \frac{1}{L} \ln \left\{ \Lambda_0^L \left[1 + \underbrace{\left(\frac{\Lambda_1}{\Lambda_0}\right)^L}_{\substack{L\to\infty \\ \longrightarrow 0}} + \underbrace{\left(\frac{\Lambda_2}{\Lambda_0}\right)^L}_{\substack{L\to\infty \\ \longrightarrow 0}} + \cdots \right] \right\} \\ &\overset{L\to\infty}{\longrightarrow} -T \ln \Lambda_0 \ . \end{aligned} \tag{2.29}$$

Note that this is the free energy of a system with dimension $\infty \times M$, i.e. there are still finite size corrections of the order $\sim \mathcal{O}(\epsilon^2)$ present. The additional limit $\epsilon \to 0$ in Eq. (2.29) yields the desired result for the quantum chain because the limits $L \to \infty$ and $\epsilon \to 0$ are interchangeable as shown by Suzuki [15]. The formula (2.29) is valid for the novel QTM whereas T has to be replaced by $T/2$ for the checkerboard QTM.[3] In principle, all other thermodynamic quantities can be derived from the free energy by numerical derivatives. However, for some quantities (e.g. magnetization or particle number) it is easier to calculate them directly in the following way. Let us consider the thermal average of a local operator $O_{1,2}$ acting at sites 1 and 2, which commutes with the local Hamiltonian $h_{i,i+1}$:

$$\begin{aligned} \langle O_{1,2} \rangle &= \lim_{L\to\infty} \frac{1}{Z} \mathrm{Tr} \left(O_{1,2} \mathrm{e}^{-\beta H} \right) = \lim_{L\to\infty} \frac{1}{Z} \mathrm{Tr} \left(T_M(O_{1,2}) T_M^{L-1} \right) \\ &\to \frac{\left\langle \Psi_0^L \right| T_M(O_{1,2}) \left| \Psi_0^R \right\rangle}{\Lambda_0} \end{aligned} \tag{2.30}$$

Here $\left\langle \Psi_0^L \right|$ and $\left| \Psi_0^R \right\rangle$ are the right and left eigenvectors, respectively, belonging to the largest eigenvalue Λ_0 of T_M. The modified transfer matrix is given by

$$T_M(O_{1,2}) = \left(\tau_{1,2}(O_{1,2}) \tau_{3,4} \cdots \tau_{2M-1,2M} \right) \left(\tau_{2,3} \tau_{4,5} \cdots \tau_{2M,1} \right) \tag{2.31}$$

with

$$\tau_{1,2}(O_{1,2}) = \left\langle s_1^1 s_1^2 \right| O_{1,2} \mathrm{e}^{-\epsilon\, h_{1,2}} \left| s_2^1 s_2^2 \right\rangle \ . \tag{2.32}$$

[3] All following relations are valid for the novel QTM. For the checkerboard QTM L has to be replaced by $L/2$ leading sometimes to an additional factor $1/2$ but leaving the formulas otherwise unchanged.

In a similar way it is also possible to receive a formula for a two-point correlation function

$$\begin{aligned}
\langle O_1\, O_r\rangle &= \frac{\left\langle \Psi_0^L\right| T_M(O_1) T_M^{r-1} T_M(O_r) \left|\Psi_0^R\right\rangle}{\Lambda_0^{r+1}} \qquad (2.33)\\
&= \langle O_1\rangle \langle O_r\rangle + \sum_{\substack{n\\ n\neq 0}} \frac{\left\langle \Psi_0^L\right| T_M(O_1) \left|\Psi_n^R\right\rangle \left\langle \Psi_n^L\right| T_M(O_r) \left|\Psi_0^R\right\rangle}{\Lambda_0 \Lambda_n} \left(\frac{\Lambda_n}{\Lambda_0}\right)^r \\
&= \langle O_1\rangle \langle O_r\rangle + \sum_{\substack{n\\ n\neq 0}} \underbrace{\frac{\left\langle \Psi_0^L\right| T_M(O_1) \left|\Psi_n^R\right\rangle \left\langle \Psi_n^L\right| T_M(O_r) \left|\Psi_0^R\right\rangle}{\Lambda_0 \Lambda_n}}_{M_n} \mathrm{e}^{-r/\xi_n}\, \mathrm{e}^{\mathrm{i}k_n r}
\end{aligned}$$

where the *correlation lengths* ξ_n and *wavevectors* k_n are given by

$$\xi_n^{-1} = \ln\left|\frac{\Lambda_0}{\Lambda_n}\right| \quad , \quad k_n = \arg\left(\frac{\Lambda_n}{\Lambda_0}\right) \ . \qquad (2.34)$$

Note that Eq. (2.33) gives an expansion of the correlation function (CF) of the form $\langle O_1\, O_r\rangle - \langle O_1\rangle \langle O_r\rangle = \sum_n M_n\, \mathrm{e}^{-r/\xi_n}\, \mathrm{e}^{\mathrm{i}k_n r}$ with *matrixelements* M_n. The long distance behaviour is dominated by the correlation length (CL) ξ_α belonging to the largest eigenvalue Λ_α ($\alpha \neq 0$) which satisfies the condition $M_\alpha \neq 0$.[4] Note also that several CLs ξ with the same wavevector k can appear in the asymptotic expansion displayed in Eq. (2.33). In the structure factor each term yields a (measurable) Lorentz function

$$S_n(k) = \frac{M_n}{2\pi} \int_{-\infty}^{\infty} dr\, e^{-|r|/\xi_n} e^{\mathrm{i}(k_n - k)r} = \frac{M_n}{\pi \xi_n} \frac{1}{(k-k_n)^2 + 1/\xi_n^2} \qquad (2.35)$$

with center at k_n, height $\sim M_n\, \xi_n/\pi$ and width $\sim 2/\xi_n$. The sharpest peak corresponds to the leading instability towards the onset of long range order and hence, a crossover in the leading CL indicates a change of the nature of the long range order. Using Eq. (2.35), it is possible to determine the CL, wavevector and matrixelement by neutron scattering experiments (see e.g. [28]) so that these quantities are not only of theoretical interest.
In addition, it is also possible to calculate imaginary time correlations $G(r,\tau)$ directly within the TMRG algorithm [26]. The fatal point is that the analytical continuation of imaginary time results with numerical errors to real times is an ill-posed problem leading to unreliable results. We will return to this point in chapter 7. What is calculated without fundamental problems are static CFs[5] defined by

$$G(r, z=0) = \int_0^\beta d\tau\ G(r,\tau) \ . \qquad (2.36)$$

This CF can be expressed by the largest eigenvalue and the corresponding left and right eigenvectors $\langle \Psi_0^L|$, $|\Psi_0^R\rangle$ of the QTM:

$$G(r, z=0) = \frac{\epsilon}{M \Lambda_0^{r+1}} \langle \Psi_0^L | \tilde{T}_M T_M^{r-1} \tilde{T}_M | \Psi_0^R\rangle \quad \text{with} \quad \tilde{T}_M = \sum_{k=0}^{M} T_M(A_{\epsilon\cdot k}) \qquad (2.37)$$

[4] We are interested in a few leading correlation lengths, i.e. in the asymptotic behaviour at large distances.

[5] Here static means $\omega = 0$, but it is also possible to calculate equal time correlation functions ($t = 0$)in a similar way .

for distances $r \geq 1$, where $T_M(A_{\epsilon \cdot k})$ denotes the usual transfer matrix T_M with the considered operator A added at imaginary time position $\tau = \epsilon \cdot k$. The static autocorrelation has to be treated separately

$$G(r=0, z=0) = \frac{\epsilon}{\Lambda_0} \langle \Psi_0^L | \hat{T}_M | \Psi_0^R \rangle \quad \text{with} \quad \hat{T}_M = \sum_{k=0}^{M} T_M(A_0, A_{\epsilon \cdot k}) \; . \tag{2.38}$$

After deriving the formulas for the CL and static CF, we can now discuss the disadvantages of the checkerboard decomposition in comparison to the novel mapping: (1) The wavevector k of a CF (see Eq. (2.34)) is not uniquely determined in the checkerboard decomposition , i.e. this QTM cannot distinguish between k and $k+\pi$; (2) the calculation of CFs (see Eqs. (2.37),(2.38)) is much more complicated, because even and odd as well as distance 1 have to be treated separately; (3) the cost of computer memory is unnecessarily large due to the repeat length of 2. This will be explained in detail in the next section. Unfortunately, there is also one disadvantage of the novel QTM one should mention. The left and right eigenstates of this non-symmetric matrix have to be calculated separately whereas this is not necessary for the checkerboard QTM due to additional symmetries. We will also discuss this point in detail in the next section.

2.2 The algorithm

In this section we will describe how the length of the transfer matrix in imaginary time direction can be extended iteratively using the DMRG scheme. With increasing Trotter number M the dimension of the transfer matrix grows exponentially and the task is to truncate this matrix in an optimal way so that even large Trotter numbers up to $M \sim 2000$ can be handled on a computer. For a Hamiltonian system the thermodynamic density matrix is usually defined by

$$\rho_{th} = \mathrm{e}^{-\beta H} \; . \tag{2.39}$$

In ordinary zero-temperature DMRG a chain of length L (so called *superblock*) is divided into two equal parts which are called *system block* S and *environment block* E. A *reduced density matrix* ρ_S is defined by performing a partial trace with respect to the environment: $\rho_S = \mathrm{Tr}_E \, \rho_{th}$. It has been shown that the eigenvectors of this matrix corresponding to the largest eigenvalues are in some sense the optimal set of system block states to represent the ground state in a reduced basis.[6] The transfer matrix is treated rather similarly to the quantum chain. We always take an even number of local Boltzmann weights, cut the transfer matrix T_M (superblock) in the middle and call one part system and the other environment block. A generalized density matrix in Trotter space is then defined by

$$\rho = T_M^L \tag{2.40}$$

[6]For details see [11] and Noack, White in [26].

which reduces in the thermodynamic limit to $\rho = \left|\Psi_0^R\right\rangle \left\langle\Psi_0^L\right|$ up to a normalization constant due to the gapped spectrum of T_M. A reduced density matrix is again defined by performing a partial trace with respect to the environment

$$\rho_S = \mathrm{Tr}_E \left|\Psi_0^R\right\rangle \left\langle\Psi_0^L\right| \ . \tag{2.41}$$

Note however that this matrix is not symmetric and it is therefore not clear whether the eigenvalues are semi-positive. Indeed a proof has been given only in a few special cases [26]. However, numerically we find that this is more or less true in all considered systems.[7] We want to emphasize that the "reduced density matrix" is only used to select the reduced basis and the results decide whether this truncation scheme is appropriate or not. Whether it is really a density matrix with a probability interpretation of its eigenvalues is a purely academic question, which is not important for the numerical approach. Taking this "problem" seriously, Bursill *et al.* [16] and others have suggested a symmetrized version

$$\rho^1_{symm} = \left|\Psi_0^R\right\rangle \left\langle\Psi_0^R\right| \ , \ \rho^2_{symm} = \left|\Psi_0^L\right\rangle \left\langle\Psi_0^L\right| \ \text{ or even } \rho^3_{symm} = \left|\Psi_0^R\right\rangle \left\langle\Psi_0^R\right| + \left|\Psi_0^L\right\rangle \left\langle\Psi_0^L\right| \ , \tag{2.42}$$

but these are no longer projection operators onto the ground state[8] leading to a bad representation of the ground state in the truncated Hilbert space and to an algorithm that breaks down rapidly after a relatively small number of RG steps. Therefore we will always use in our calculations the non-symmetric reduced density matrix defined in Eq. (2.41).

In practical computations the small parameter ϵ in the Trotter-Suzuki mapping (see Eqs. (2.18) and (2.25)) is fixed where $\epsilon = 0.025$ to 0.05 has turned out to be a suitable choice. The temperature is then given by $T \sim 1/\epsilon M$ and is decreased by an iterative algorithm where $M \to M + 1$. Here and in the following M denotes the number of local Boltzmann weights (plaquettes) in the system block. The complete QTM therefore consists of $2M$ plaquettes. In the following we discuss the algorithms for the checkerboard QTM (see a) below) as well as for the novel QTM (see b) below). Whereas the algorithm for the checkerboard QTM closely follows the one outlined by Wang, Xiang and Shibata [17, 18], we have formulated a modified one for the novel QTM, which takes advantage of the different transfer-matrix structure and allows us to reduce the required computer memory drastically. Note that it is also possible to formulate the algorithm for the novel QTM completely analogous to the traditional one, but in this case the same amount of memory is needed. In all steps and both algorithms the cases M even and odd have to be treated separately. In the following the column-to-column transfer matrices (QTMs) are shown in a 90°-rotated view.

1) We start by constructing an initial *system block* Γ containing M plaquettes so that a) $S^{M-1} \leq N < S^M$ or b) $S^M \leq N < S^{M+1}$ where S denotes the dimension of the local Hilbert space and N is the number of states which we want to keep within the

[7] Sometimes eigenvalue pairs with small imaginary parts occur as discussed in chapter 3.

[8] That means, e.g. $\left\langle\Psi_0^L\right| \rho^3_{symm} = a \left\langle\Psi_0^R\right| + b \left\langle\Psi_0^L\right| \neq \left\langle\Psi_0^L\right|$ with some normalization constants $a, b \neq 0$.

renormalization. The plaquettes are connected by a summation over the adjacent corner spins (structure of a tensor product).

a) 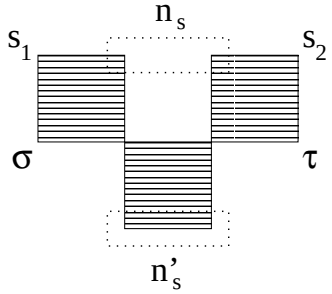

b) 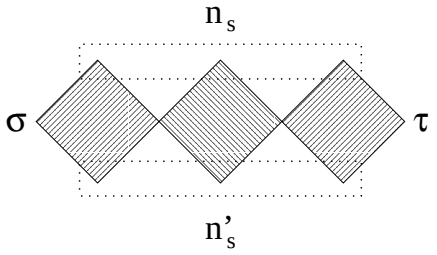

Each so called *block-spin variable* n_s, n'_s contains in the initial step a) $\tilde{N} = S^{M-1}$ or b) $\tilde{N} = S^M$ states. The a) $S^4 \cdot \tilde{N}^2$-dimensional array $\Gamma(s_1, n_s, s_2, \sigma, n'_s, \tau)$ or b) $S^2 \cdot \tilde{N}^2$-dimensional array $\Gamma(\sigma, n_s, \tau, n'_s)$ is stored.

2) a) The *superblock* T_{2M} is built by connecting the *system block* and the *environment block* by a τ-summation where the environment block is constructed analogously to the system block or is just given by a 180°-rotation of the system block if the local interaction is reflection symmetric, i.e. $h_{i,i+1} = h_{i+1,i}$. This is the case for all models considered here.

b) A plaquette is added to the system block to form the enlarged system block $\tilde{\Gamma}(\sigma, n_s, s_2, \tau, s'_2, n'_s)$ which is a $S^4 \cdot \tilde{N}^2$-dimensional array. The same is done for the environment block. If $h_{i,i+1}$ is real, the environment block can be constructed by a 180°-rotation and a following inversion of the system block. A reflection symmetry is **not** needed![9] The *enlarged blocks* are connected to form the superblock T_{2M+2}.

a) 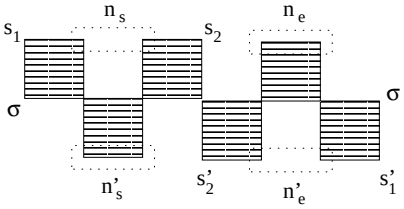

b) 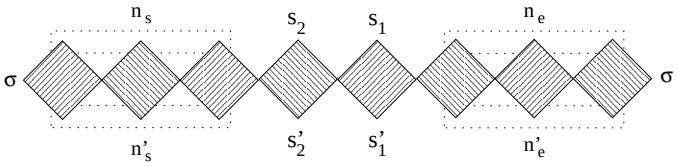

In both cases the superblock is closed periodically by a summation over all σ-states.

3) The largest eigenvalue Λ_0 and the corresponding left and right eigenstates

$$\left\langle \Psi_0^L \right| = \Psi^L(s_1, n_s, s_2, n_e), \quad \left| \Psi_0^R \right\rangle = \Psi^R(s'_1, n'_s, s'_2, n'_e)$$

of the superblock are calculated. The eigenvectors are normalized by $\left\langle \Psi_0^L | \Psi_0^R \right\rangle = 1$. If correlation lengths are needed, next-leading eigenvalues have to be calculated additionally.

[9] This might be interesting for models with next-nearest neighbour interactions where 2 sites are combined to a supersite in order to receive a local Hamiltonian $\tilde{h}_{i,i+1}$ containing only nearest neighbour interactions and being translationally invariant. However, $\tilde{h}_{i,i+1} \neq \tilde{h}_{i+1,i}$ making it necessary to store and renormalize the environment block explicitly within the checkerboard formalism. The new QTM allows it even in this case to construct the environment from the system block and therefore saves computer memory and computing time.

4) At the temperature a) $T = 1/\epsilon M$ or b) $T = 1/\epsilon(2M+2)$ the free energy, correlation lengths and other thermodynamic quantities are evaluated.

5) The density matrix is given by a) $\rho = T_{2M}^{L/2}/\mathrm{Tr}\ T_{2M}^{L/2}$ or b) $\rho = T_{2M+2}^{L}/\mathrm{Tr}\ T_{2M+2}^{L}$ and reduces in both cases in the thermodynamic limit to $\rho = \left|\Psi_0^R\right\rangle\left\langle\Psi_0^L\right|$ due to the gapped spectrum of the QTMs. A reduced density matrix is now calculated by performing a partial trace with respect to the environment

$$\begin{aligned}\rho_s(n_s', s_2'|n_s, s_2) &= \sum_{s_1, n_e} \left|\Psi_0^R\right\rangle\left\langle\Psi_0^L\right| \\ &= \sum_{s_1, n_e} \Psi^R(s_1, n_s', s_2', n_e)\Psi^L(s_1, n_s, s_2, n_e)\end{aligned}$$

and the complete spectrum of this non-symmetric matrix is determined. If the Hamiltonian has no spatial reflection symmetry, a second reduced density matrix ρ_e has to be calculated in case a) by performing a partial trace with respect to the system. The left (right) eigenstates of ρ_s corresponding to the *N largest eigenvalues* are used to construct a $N \times (S \cdot \tilde{N})$-matrix $V^L(\tilde{n}_s|n_s, s_2)$ ($V^R(\tilde{n}_s'|n_s', s_2')$) where $\tilde{n}_s$ ($\tilde{n}_s'$) is a new, renormalized block-spin variable. The eigenstates are normalized satisfying the orthonormality relation $(V^L)^T \cdot V^R = \mathbf{1}$.

6) a) The system block is enlarged by adding a plaquette to form the enlarged system block $\tilde{\Gamma}(s_1, n_s, s_2, \tau, \sigma, n_s', s_2', \tilde{s}_2')$ which is a $S^6 \cdot \tilde{N}^2$-dimensional array. The matrices V^L and V^R are used to truncate the Hilbert space and to receive new block-spin variables $\tilde{n}_s$, $\tilde{n}_s'$ taking only N possible values. If no spatial reflection symmetry is present, the same is done for the environment block.

b) The system block is renormalized by applying V^L and V^R. New block-spin variables $\tilde{n}_s$ and $\tilde{n}_s'$ are received.

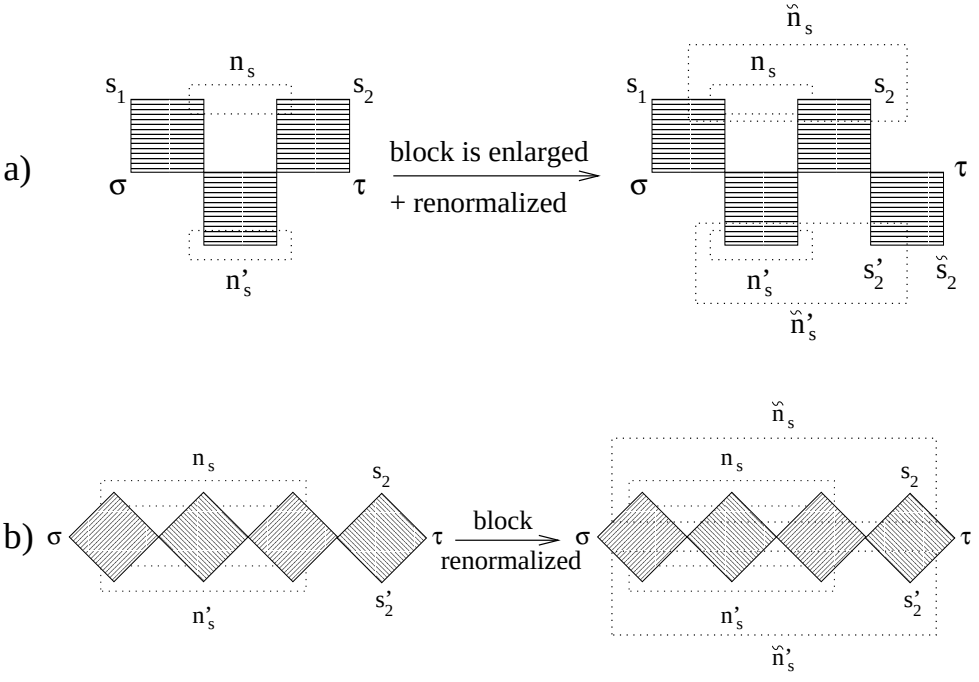

The renormalization to the new system block is given explicitly by

$$\begin{aligned}
\text{a)} \quad & \Gamma(s_1, \tilde{n}_s, \tau, \sigma, \tilde{n}'_s, \tilde{s}'_2) \\
= \quad & \sum_{n_s, s_2} \sum_{n'_s, s'_2} V^L(\tilde{n}_s | n_s, s_2) \tilde{\Gamma}(s_1, n_s, s_2, \tau, \sigma, n'_s, s'_2, \tilde{s}'_2) V^R(\tilde{n}'_s | n'_s, s'_2) \\
\text{b)} \quad & \Gamma(\sigma, \tilde{n}_s, \tau, \tilde{n}'_s) \\
= \quad & \sum_{n_s, s_2} \sum_{n'_s, s'_2} V^L(\tilde{n}_s | n_s, s_2) \tilde{\Gamma}(\sigma, n_s, s_2, \tau, s'_2, n'_s) V^R(\tilde{n}'_s | n'_s, s'_2) \ .
\end{aligned}$$

With the new system block the algorithm is repeated starting with step 2. All following steps remain unchanged, however, now the block-spin variables n_s, n'_s and n_e, n'_e can take N instead of $\tilde{N}$ values.

The main difference between the two algorithms explained above is that in step 2 the system and the environment block are connected to form the superblock for the checkerboard QTM whereas the **enlarged blocks** are used in the novel QTM. Therefore steps 5 and 6 take place on different size systems for the checkerboard QTM[10] whereas the size remains unchanged in these steps in the modified algorithm. One should mention that it is algorithm a) which is very much in spirit of the algorithm proposed by White [11] for the zero-temperature DMRG. However, the modified algorithm yields results with a comparable accuracy (see next chapter) with the advantage that the system and the enlarged system block are a factor S^2 smaller than in the traditional algorithm. This is very useful for systems with many local degrees of freedom as, for example, the spin-orbital model discussed in chapter 6.1 where $S = 6$. Note that it is not possible to reduce the dimension of the system block array in step 1 of algorithm a) further due to the left/right asymmetry of the checkerboard QTM. On the other hand it is possible to build a system block for the novel QTM in step 1 which contains 4 spins and two block spins as the system block for the checkerboard QTM.

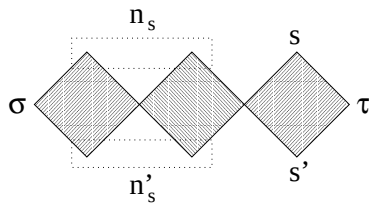

Starting with this system block, it is possible to proceed with the old algorithm a) where renormalization and real-space blocking take place at different size systems, but in this case the system and enlarged system block have the same dimensions as the blocks in the checkerboard formalism.

The computational effort is drastically reduced in most models due to *conserved quantities*. For example, the local Hamiltonian for the Heisenberg model conserves the total

[10]The reduced density matrix for a system block with size M calculated in step 5 is used to renormalize the enlarged system block with size $M + 1$ in step 6.

magnetization. Using the notation for a plaquette shown in Fig. 2.3 this conservation law reads

$$s_1 + s_2 = s_1' + s_2' \quad \text{or} \quad s_1 - s_1' = s_2' - s_2 \tag{2.43}$$

when looking into imaginary time direction. Similar conservation laws occur for the t-J model (spin and charge) and for the spin-orbital models (spin and orbital flavour). This leads to a *block structure* of the system, environment and superblock and also of the reduced density matrix. For example, a matrixelement of the checkerboard system block shown in step 1 of the algorithm is only nonzero if $s_1 + n_s - s_2 = -\sigma + n_s' + \tau$, where the quantum numbers for the block-spins n_s and n_s' have to be calculated and stored in each RG step.[11] Furthermore, the largest eigenvalue of the QTM in step 2 a) is located in the block with total quantum number

$$\mathcal{K} = s_1 + n_s - s_2 - n_e = s_1' + n_s' - s_2' + n_e' = 0 \tag{2.44}$$

and a similar equation holds for the novel QTM. This is obvious at infinite temperature where the eigenstates are depicted graphically in Fig. 2.4 and we expect that the largest eigenvalue remains in the $\mathcal{K} = 0$ block even at finite temperature since there is no level crossing in 1D. Therefore only the $\mathcal{K} = 0$ block has to be considered in step 3 of both algorithms. Another symmetry allows it to construct the left eigenvectors of the checkerboard QTM from the right eigenvectors (this is obvious at infinite temperature from Fig. 2.4) and vice versa in the following way

$$\Psi^L(s_1, n_s, s_2, n_e) = \Psi^R(s_1, n_e, s_2, n_s)\ . \tag{2.45}$$

This is very useful because the calculation of eigenvalues and eigenvectors of the QTM is the step taking most computational time in the whole algorithm. Therefore it is a serious disadvantage that the same is not possible in practical computations for the novel QTM. Regarding again the infinite temperature case shown in Fig. 2.4, it is obvious that one obtains the right eigenvector in this case if the left eigenvector is rotated by 180° as for the checkerboard QTM, but additionally a translation by one site in imaginary time direction is needed. However, it is not possible to perform such a translation within the TMRG algorithm because after a renormalization of the block-spins the information about a single site within a block is lost. To define a system block in the following way

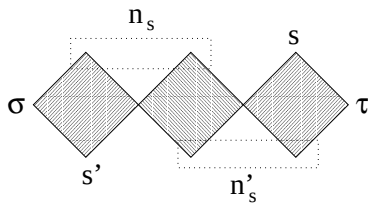

is also useless because it is not possible to perform iterative matrix-vector multiplications with the corresponding superblock. However, such multiplications are needed in step 3 of the algorithm to calculate the eigenvectors effectively as discussed in detail in the next chapter.

[11] The signs in the conservation law are different for even and odd numbers M. That is one reason why even and odd Trotter numbers have to be treated separately.

Chapter 3

Numerical Implementation

The algorithms discussed in the preceding chapter have been programmed using the language C.[1] First, we will discuss how the eigenvalues and eigenvectors can be calculated effectively in step 3 of the algorithm. Because we are dealing with a large but sparse matrix and only need a few leading eigenvalues and corresponding eigenvectors, routines like the power, the look-ahead Lanczos or the implicitly restarted Arnoldi method are well suited. Compared to complete diagonalizers they have the important advantage that only a matrix-vector multiplication is needed to determine the eigensystem in an iterative procedure. Therefore it is **not necessary to construct the superblock explicitly** saving an enormous amount of computer memory and computational time, because the dimension of the superblock is S^4N^4 compared to S^4N^2 (S^2N^2) for the system block of the traditional (novel) algorithm. Additionally, it is sufficient to regard only the $\mathcal{K} = 0$ block as explained before.[2] The matrix-vector multiplication is divided into two parts where system and environment block act consecutively on the vector. As an example we take the checkerboard QTM where system and environment block contain an odd number M of plaquettes. The matrix-vector multiplication $\Phi_f = T_{2M} \cdot \Phi_s$ is then performed in the following way

$$\begin{aligned} 1) \quad \tilde{\Phi}_s(n'_e, k_0, n_s, k_1) &= \sum_{s_1, s_2, n_e} \Gamma_e(s_1, n_e, s_2, k_0, n'_e, k_1) \Phi_s(s_1, n_s, s_2, n_e) \\ 2) \quad \Phi_f(s'_1, n'_s, s'_2, n'_e) &= \sum_{k_o, k_1, n_s} \Gamma_s(s'_1, n'_s, s'_2, k_0, n_s, k_1) \tilde{\Phi}_s(n'_e, k_0, n_s, k_1) \; . \end{aligned} \tag{3.1}$$

This multiplication routine is the basis element for all iterative diagonalization methods we have applied. To calculate a first approximation we usually begin with the simplest iterative scheme, the so called power method, which works in the following way. Starting point is a random vector $|\phi\rangle = \sum_i a_i |\Psi_i\rangle$ where $|\Psi_i\rangle$ are the eigenstates of T_{2M}. Now T_{2M} is applied k-times onto this vector

$$T_{2M}^k |\phi\rangle = \sum_i a_i \Lambda_i^k |\Psi_i\rangle = \Lambda_0^k \sum_i a_i \left(\frac{\Lambda_i}{\Lambda_0}\right)^k |\Psi_i\rangle \overset{k\to\infty}{\longrightarrow} a_0 \, \Lambda_0^k |\Psi_0\rangle \; , \tag{3.2}$$

[1] For the algorithm based on the checkerboard decomposition a program written by Rainer Raupach [29] has been used as a starting point. However, even in this case the program was completely changed. Many improvements have been made leading to higher accuracy, a reduction in needed memory by a factor $\sim N^2$ and a reduction in computation time by a factor $10 - 100$.

[2] If correlation lengths are needed with corresponding eigenvalues in other blocks, these blocks have to be calculated additionally and have to be diagonalized separately.

yielding an approximation for the eigenvector $|\Psi_0\rangle$ corresponding to the largest eigenvalue Λ_0. This vector is used as initial vector in ARPACK [30], which is a well tested package to solve large scale eigenvalue problems and is based on the implicitly restarted Arnoldi method. Again this routine needs only the matrix-vector multiplication in Eq. (3.1) to compute leading eigenvalues and eigenvectors. We apply ARPACK in addition to the power method for two reasons. First, the convergence of the power method depends on the ratio Λ_1/Λ_0 (see Eq. (3.2)), i.e. the correlation length (see Eq. (2.34)), and the number of iterations k needed to obtain Λ_0 and $|\Psi_0\rangle$ accurately increases therefore with decreasing temperature making the algorithm unfavorable at low temperatures. Second, we are also interested in next-leading eigenvalues and corresponding eigenvectors to calculate correlation lengths. These cannot be obtained with the power method in a simple manner.

A second diagonalization, the diagonalization of the reduced density matrix $\rho_s(n_s', s_2'|n_s, s_2)$, has to be performed in step 5 of the algorithms. This matrix again has a block structure and matrixelements are only nonzero if

$$n_s - s_2 = n_s' - s_2' \qquad \text{(checkerboard QTM with M odd)}\,, \tag{3.3}$$

where similar conservation laws hold in the other cases. Therefore we can calculate and diagonalize each block separately. Because the complete spectrum of the reduced density matrix is needed and each block is relatively small, standard LAPACK diagonalization-routines [31] for non-symmetric matrices (DGEEVX) are used. For several reasons explained in the following, this part is numerically very complicated and several "tricks" are needed to stabilize the algorithm and to obtain results with a sufficient accuracy.[3] One reason is that the magnitude of the eigenvalues decreases rapidly especially at high temperatures (see Fig. 3.1) so that parts of the spectrum become numerically indistinguishable from zero. The "eigenvectors" corresponding to these numerically vanishing eigenvalues are more or less random vectors so that the left and right eigenvectors belonging to different eigenvalues are no longer orthogonal. This problem is particularly serious for models with small or vanishing interactions (e.g. in the free spinless fermion model shown in the right part of Fig. 3.1) and might cause a breakdown of the algorithm after a few RG steps [32]. Another connected problem are pairs of complex conjugated eigenvalues which occur mostly for eigenvalues with a small magnitude. We have solved these problems in the following way:

1) Every block of the matrix ρ_s is balanced by multiplying each matrixelement with a large factor $A \sim 10^8$ and adding a constant factor $B \sim 1$ to the diagonal elements. The eigenvectors remain unchanged whereas the eigenvalues are shifted by $\Lambda \to A\Lambda + B$. This balancing enhances the accuracy of the diagonalization routine.

2) If complex conjugated pairs appear, it turns out that the imaginary part is always relatively small. We therefore take the real part as eigenvalue and the real and the

[3] R. Raupach has used MAPLE to diagonalize the reduced density matrix [29] because within this program it is principally possible to receive eigenvalues with arbitrary accuracy. However, this causes a slowing down of the algorithm by many orders of magnitude and makes it practically impossible to retain more than $N \sim 50$ states for a Heisenberg model.

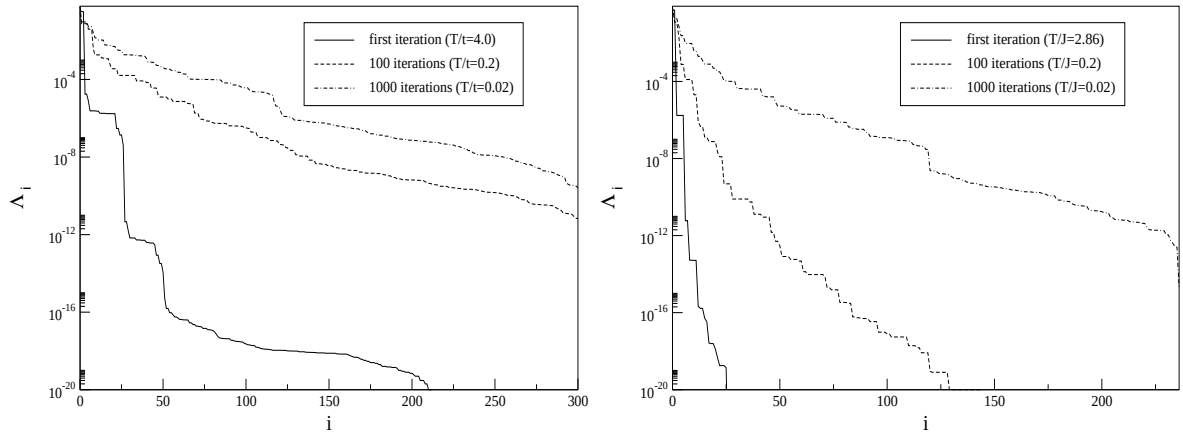

Figure 3.1: The eigenvalue spectra of the reduced density matrix for the supersymmetric t-J model (left graph) and the free spinless fermion model (right graph) at different iteration steps. The number of iterations is proportional to $1/T$.

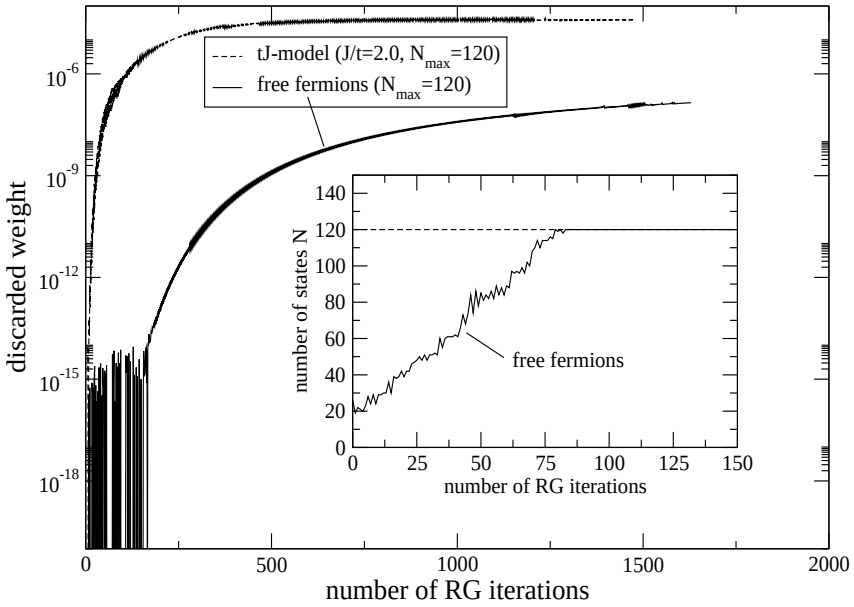

Figure 3.2: The main figure shows the *discarded weights* w_i defined by $w_i = 1 - \sum_{i=1}^{N} \Lambda_i$ where N is the number of states kept in each RG step. N is defined by the number of eigenvalues Λ_i being larger than 10^{-20}. The inset shows how the number of states N increases with decreasing temperature where $N_{max} = 120$ is chosen. Note that $N = N_{max}$ is set from the beginning for the t-J model.

imaginary part of the eigenvector separately as corresponding eigenvectors

$$\left\{ w_r \pm \mathrm{i} w_i \,;\, \left|\Psi_r^R\right\rangle \pm \mathrm{i} \left|\Psi_i^R\right\rangle \right\} \longrightarrow \left\{ w_r \,,\, \left|\Psi_r^R\right\rangle \,;\, w_r \,,\, \left|\Psi_i^R\right\rangle \right\} \ .$$

The left eigenvectors are chosen to fulfill the orthonormality relation

$$\left\langle \Psi_\sigma^L | \Psi_{\sigma'}^R \right\rangle = \delta_{\sigma,\sigma'} \quad \text{with} \quad \sigma,\, \sigma' = r, i \ .$$

3) We have to remember that the rapidly decreasing spectrum, especially for models with small interactions, is not a disadvantage, it is exactly what we want! It means that the largest-eigenvalue state of the QTM can be approximated by only a few eigenstates of the density matrix. It is unreasonable to keep states within the RG which do not contribute or with a contribution which is smaller than the numerical accuracy. We therefore keep only density-matrix eigenstates with eigenvalues $\Lambda > 10^{-20}$ which redefines the number of block-spin states N in each iteration. With decreasing temperature (increasing number of iterations) the eigenvalue spectrum of ρ_s becomes denser (see Fig. 3.1) so that more density-matrix eigenstates are needed to represent the largest-eigenvalue state of the QTM with the same accuracy. This leads to an increasing N with decreasing temperature where $N \leq N_{max}$ with a given maximal number N_{max} of retained states. The number of states N as a function of RG steps is shown in the inset of Fig. 3.2 for the supersymmetric t-J model and the free spinless fermion model. A measure for the truncation error in each RG step is given by the *discarded weight*

$$w_i = 1 - \sum_{i=1}^{N} \Lambda_i \ . \tag{3.4}$$

This quantity is shown for the supersymmetric t-J model and the free spinless fermion model in Fig. 3.2 where we have set $N_{max} = 120$.

The outlined method has turned out to be much more effective than keeping N constant and performing a reorthonormalization of the random vectors belonging to the small eigenvalues as done by Ammon *et al.* [32]. Finally, we want to mention that both algorithms never break down so rapidly as described in their paper, even in an implementation without the improvements explained before.

Chapter 4

Accuracy Analysis

In this chapter we will check the accuracy of the two described algorithms by comparing the numerics with exact results. There are two main sources for errors in TMRG calculations. First, there is the error due to the Trotter-Suzuki mapping of the quantum chain to the 2D classical model with a finite Trotter parameter ϵ (see Eqs. (2.18, 2.25)). The $\mathcal{O}(\epsilon^2)$-correction for the transfer matrices seems to lead to an error $\sim \mathcal{O}(\epsilon)$ in the partition function. However, in both mappings it turns out that the operator in this correction term is anti-Hermitian. Because the trace of an anti-Hermitian operator in a real representation yields zero (see appendix A for a detailed discussion), the linear correction in the partition function vanishes. Second, there is the error due to the truncation of the Hilbert space in each RG step. A certain estimate for this error is given by the discarded weight defined in Eq. (3.4). This quantity is relatively small at high temperatures (see Fig. 3.2) and increases with decreasing temperature when the spectrum of the reduced density matrix becomes denser (see Fig. 3.1). We therefore expect a dominating mapping error at high temperatures and a dominating truncation error at low temperatures.

The first model we want to consider are free spinless fermions on a lattice. This model is very simple and all quantities we are interested in can be calculated analytically. A brief discussion including all relevant formulas is given in appendix B. Although a model of free fermions is easy to treat from an analytical point of view, the TMRG algorithm cannot take any advantage of that and the numerical calculations are indeed harder than for interacting particles due to the rapidly decaying eigenvalue spectrum of the reduced density matrix as explained in the previous chapter. First, we will compare the two different algorithms by calculating the free energy according to Eq. (2.29). The deviations of the numerical from the exact result are shown in Fig. 4.1. In both cases the error is of the order 10^{-6} to 10^{-5} over a wide temperature range. Whereas the novel algorithm yields slightly better results for a moderate number (~ 1000) of RG steps, it becomes unstable at low temperatures (see inset of Fig. 4.1). This instability is due to the fact that left and right eigenstates have to be calculated separately in the novel algorithm so that the diagonalization-error is doubled[1] whereas Eq. (2.45) can be applied for the traditional algorithm. In both cases there is no variational principle for the free energy so that the numerical results might be larger or smaller than the exact result and crossings are possible. This explains the unexpected decrease of the error at low temperatures for the traditional algorithm where the numerical result just starts to cross the exact result

[1] A change of parameters in the diagonalization routine clearly shows that this is the main source for instability. Increasing the computational effort in this step we can significantly improve the results for the novel algorithm at low temperature. Here we apply in both cases the diagonalization routine with the same parameters to make the results comparable.

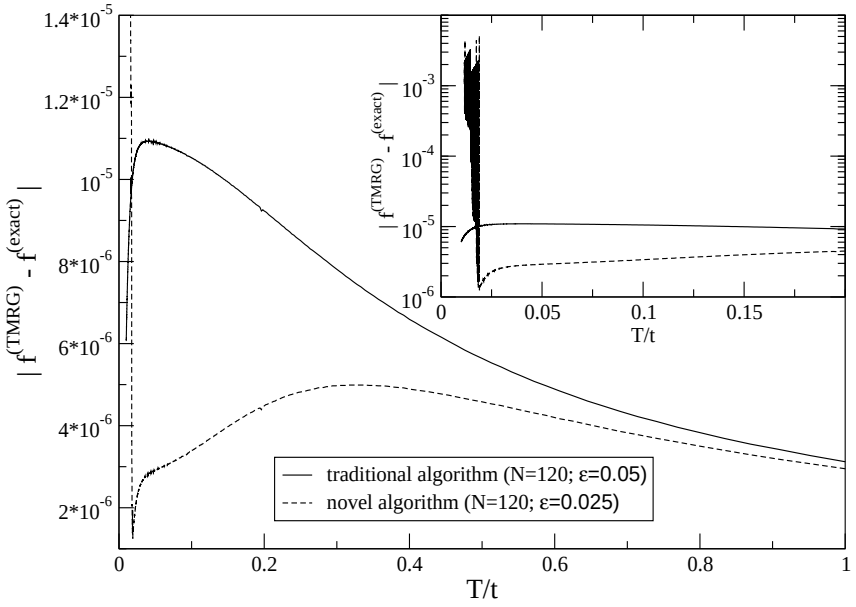

Figure 4.1: Deviations of the free energies calculated by TMRG from the exact result as a function of temperature. In both algorithms the number of states retained within the RG is set to $N = 120$. Remember that the novel algorithm evolves twice as fast as the traditional one. Therefore the Trotter parameter is set to $\epsilon = 0.05$ ($\epsilon = 0.025$) for the traditional (novel) algorithm so that each temperature is reached by the same number of RG steps. The inset shows an enlargement of the low temperature region.

from below.

Next, we will test our expectations about the scaling with ϵ and N numerically. In Fig. 4.2 (a) the accuracy of the free energy calculated with the traditional algorithm is shown as a function of ϵ for different temperatures T. The values for zero temperature are obtained by using

$$f = e_0 - \frac{\pi}{6} a \cdot T^2 \tag{4.1}$$

with parameters e_0, a for a fit of the data in the temperature region $T/t \in [0 : 0.02]$.[2] For $T/t = 1.0$, 0.5 and 0.1 the error is proportional to ϵ^2 showing that the mapping error is the dominant contribution. For temperatures $T/t \leq 0.05$ no clear scaling behaviour can be detected. Here the truncation error due to the RG procedure is dominant. In Fig. 4.2 (b) the same plot is shown for the novel algorithm. For $T/t = 1.0$, 0.5, 0.1 and roughly also for $T/t = 0.05$ we find again the expected ϵ^2-scaling. Note however that the error at low T and small ϵ, where this scaling is no longer detectable, is one or two orders of magnitude larger than in the traditional algorithm due to the instabilities in the RG procedure for the novel algorithm. The strict scaling of the numerical data with ϵ^2 at high and intermediate temperatures can be used to extrapolate the numerical data and to minimize the errors. For example, by extrapolating the data produced by the traditional

[2]The low temperature asymptotics is predicted by conformal field theory where $a = c/v = 1$ with central charge c and charge velocity v in agreement with a low temperature expansion of the exact result.

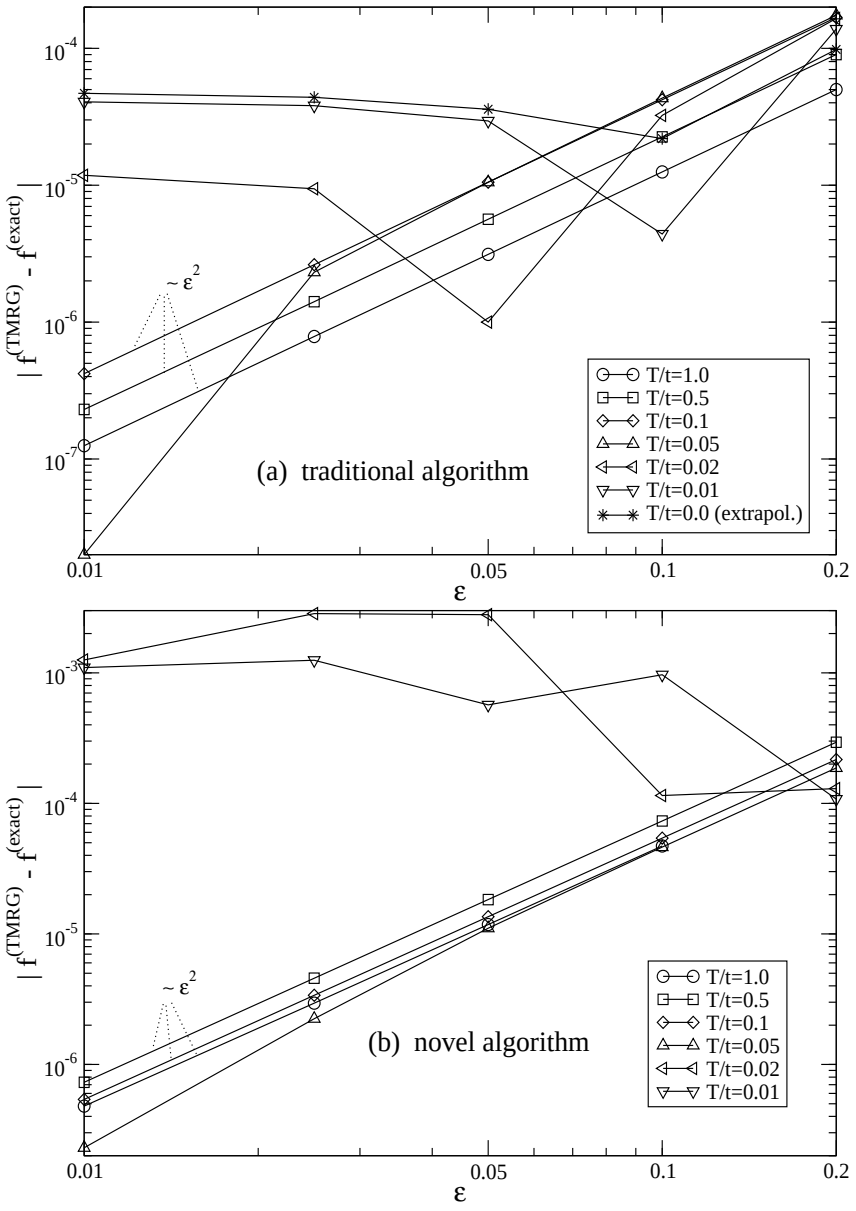

Figure 4.2: Deviations of the free energy calculated with the traditional (novel) algorithm from the exact result as a function of the Trotter parameter ϵ where $N = 60$ states are retained in the RG. The number of RG steps needed to reach the lowest numerically calculated temperature $T/t = 0.01$ increases from 500 (250) for $\epsilon = 0.2$ to 10000 (5000) for $\epsilon = 0.01$. Note that the error is proportional to ϵ^2 at high and intermediate temperatures whereas no clear scaling is detectable at low temperatures.

algorithm for $T/t = 1.0$, 0.5 and $T/t = 0.1$, estimates for the free energy with errors of the order 10^{-8} only, are obtained.

Next, we will investigate how the accuracy of the data depends on the number of states N retained in the DMRG procedure. In Fig. 4.3 the accuracy for different N is shown. For

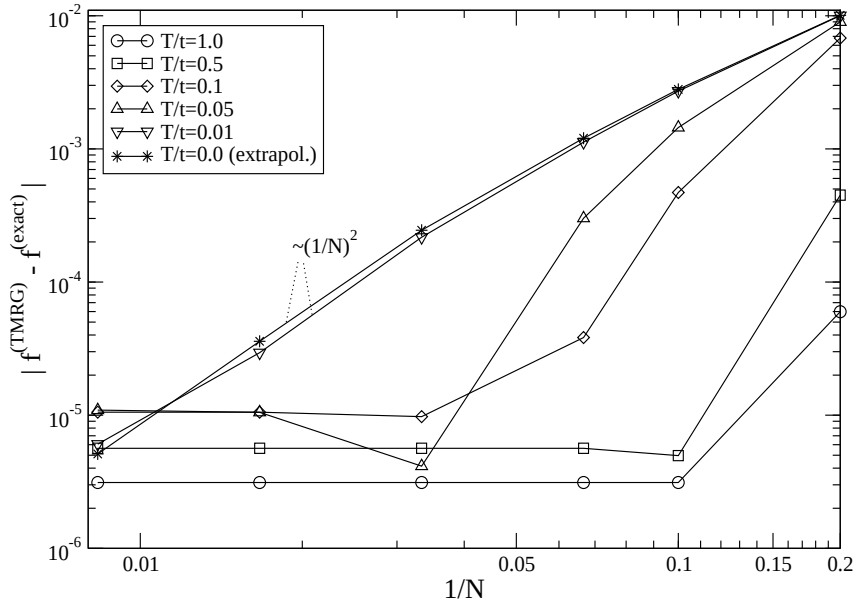

Figure 4.3: Accuracy of the free energy calculated with the traditional algorithm ($\epsilon = 0.05$) as a function of the number of RG-states N. The $T = 0$ data are again obtained by a fit using formula (4.1).

$T/t = 1.0$, 0.5, 0.1 and 0.05 the accuracy is improved with N but "saturates" at a certain level so that no further improvement is possible by increasing N. The saturation value is here given by the error due to the finite ϵ (compare with $\epsilon = 0.05$ in Fig. 4.2 (a)). The data for temperatures $T/t = 0.01$ and 0, on the other hand, show that the accuracy at low temperatures can be crucially improved by increasing N. The error scales in these cases roughly like $(1/N)^2$. It is really astonishing that the error remains smaller than 10^{-2} over the whole temperature range even with only 5 states retained, especially, because such a calculation costs less than 2 seconds computational time on a standard PC! In summary we have a competition between mapping and truncation error: A small ϵ minimizes the mapping error but it also enhances the number of RG steps necessary to reach a certain temperature and therefore enhances the error due to truncation and additionally also the computational time. The number of states N, on the other hand, determines the accuracy of the TMRG data at low temperatures.

For free spinless fermions it is also possible to calculate correlation lengths analytically. A brief overview is given in appendix B. In Fig. 4.4 we compare the numerical result for the density-density correlation length received by formula (2.34) with the exact result calculated by Eq. (B.12c). A good agreement is obtained with errors of the numerical data remaining smaller than 10^{-3} for temperatures down to $T/t \sim 0.1$. Additionally, it is possible to calculate analytically also the static density-density correlation function itself. For two characteristic temperatures we show in Fig. 4.5 results obtained by TMRG using Eqs. (2.37) and (2.38) in comparison to the exact result from a numerical evaluation of Eq. (B.9). The absolute error is largest for short distances and decreases exponentially

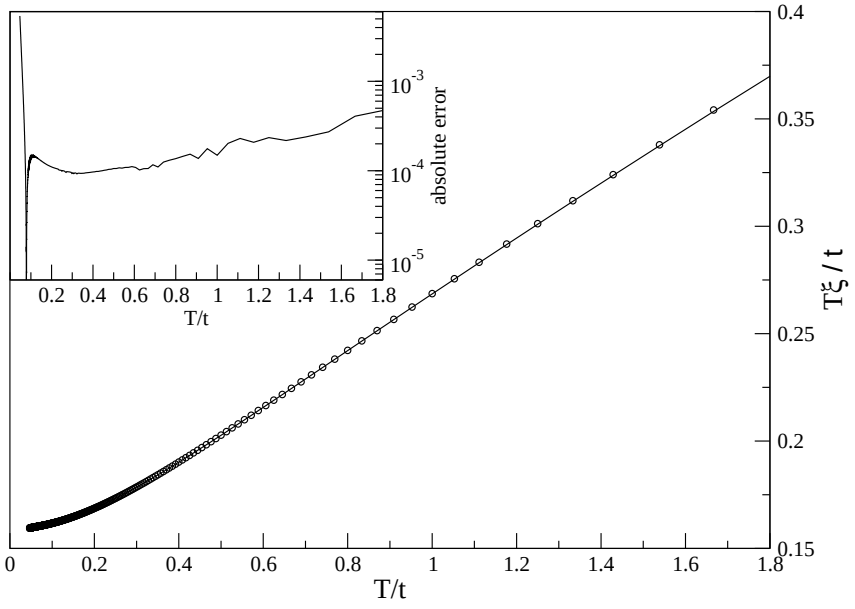

Figure 4.4: Exact result for the correlation length (line) compared to TMRG results (circles) with 120 states retained. The inset shows the errors of the TMRG results.

with distance. However, even at $T/t = 0.1$ the error remains for all distances smaller than 10^{-2} showing that TMRG yields useful results not only for the asymptotic behaviour of static correlation functions but also at short distances.

Next we will study results for the anisotropic Heisenberg (XXZ) model defined by

$$H = J \sum_i \left\{ S_i^x S_{i+1}^x + S_i^y S_{i+1}^y + \Delta S_i^z S_{i+1}^z \right\} \ . \tag{4.2}$$

By the Jordan-Wigner transformation this model can be mapped onto the spinless fermion model and the noninteracting case considered before is obtained for $\Delta = 0$. We can therefore test how the accuracy of TMRG changes when we go from the free to the interacting spinless fermion model. It is possible to calculate the free energy and the leading correlation length analytically also in the general case with nonzero Δ. However, the methods are much more involved and are based on the Bethe ansatz which is applied to a QTM similar to the one used in the novel TMRG algorithm. This results in a nonlinear integral equation for the leading and next-leading eigenvalues of the QTM which yield the free energy and correlation lengths using Eq. (2.29) and Eq. (2.34) completely analogous to TMRG [33]. Here we choose $\Delta = 0.5$ and first compare the numerical and exact results for the free energy. In Fig. 4.6 the deviations from the exact result are shown. Note that $\epsilon = 0.05$ is chosen in both algorithms contrary to the calculations for the free case (see Fig. 4.1) where $\epsilon = 0.025$ is used in the novel algorithm. Therefore the novel algorithm needs only 1000 steps to reach the lowest temperature $T/t = 0.01$ and instabilities do not occur. On the other hand the larger ϵ enhances the errors of the novel algorithm at higher T/t due to the larger mapping error. Comparing the results obtained by the traditional

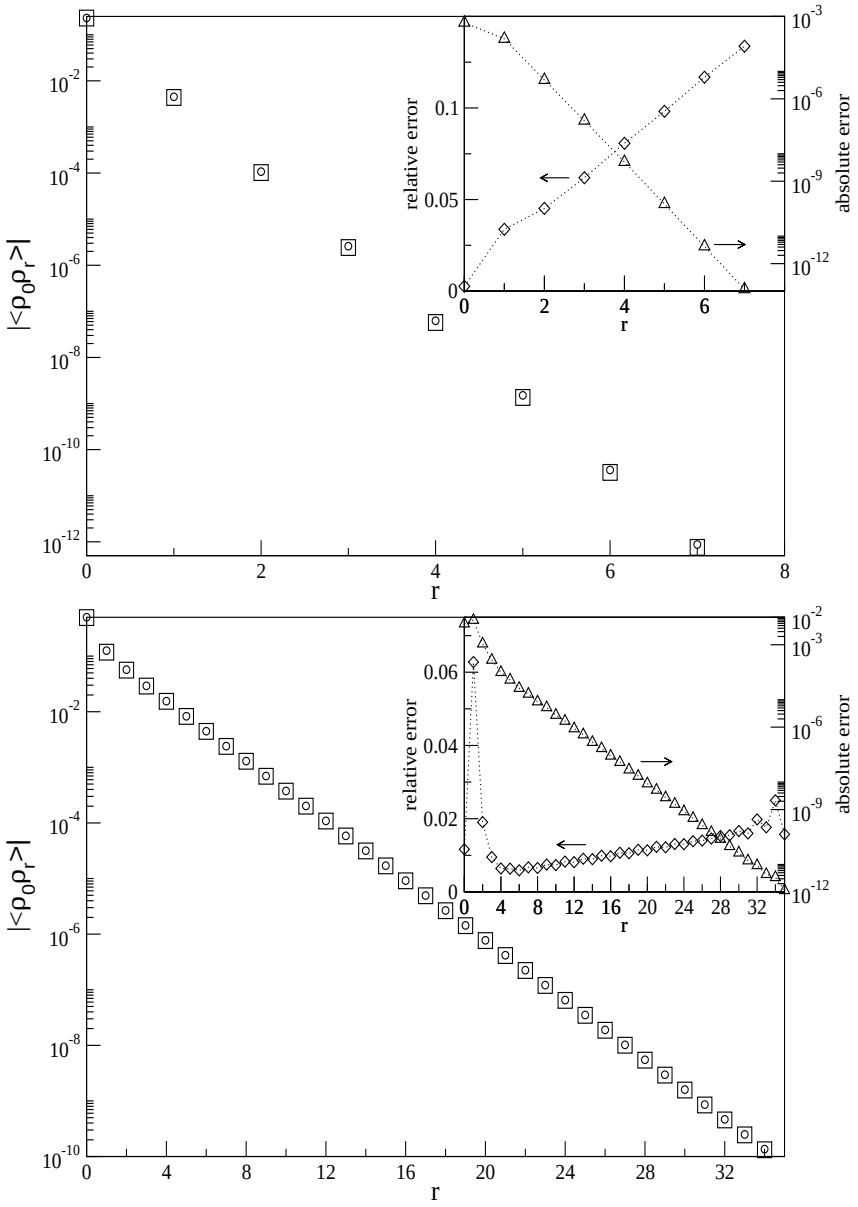

Figure 4.5: The upper (lower) graph shows the static density-density correlation function for free spinless fermions at $T/t = 1.0$ ($T/t = 0.1$) calculated by Eq. (B.9) (circles) and by TMRG (squares) with $N = 120$ states retained. The correlation function shows in both cases commensurate oscillations with $k = \pi$. Note that non-oscillating parts do not contribute due to the integration in imaginary time direction (see detailed discussion in subsection 5.1.2). The insets show the absolute errors (triangles) and the relative errors (diamonds) of the TMRG results. The lines are guides to the eye. A fit of the asymptotics yields $\xi = 0.2670 \pm 0.0005$ ($\xi = 1.6155 \pm 0.0008$) for $T/t = 1.0$ ($T/t = 0.1$) in good agreement with the estimate from the direct calculation of the correlation length in Fig.4.4 where $\xi = 0.2673$ ($\xi = 1.6161$).

algorithm in the free (Fig. 4.1) and in the interacting case (Fig. 4.6), it turns out that the error in the interacting case is only slightly larger and remains of the same order.

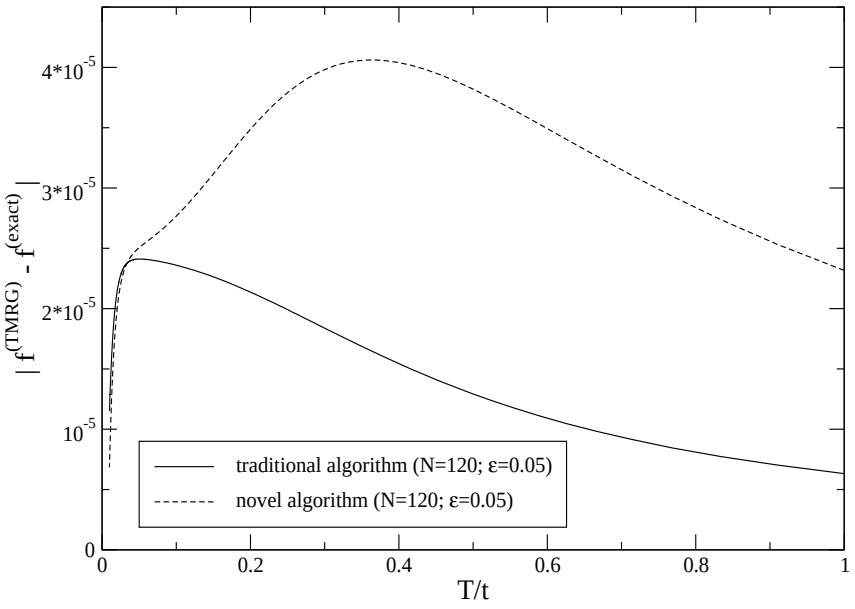

Figure 4.6: Deviations of the free energies for the XXZ-model with $\Delta = 0.5$ calculated by TMRG from the exact result as a function of temperature. In both algorithms the number of states retained within the RG is set to $N = 120$. Contrary to Fig. 4.1 we have set $\epsilon = 0.05$ in both algorithms. Therefore $T/t = 0.01$ is reached by 2000 (1000) RG-steps in the traditional (novel) algorithm.

In Fig. 4.7 the leading density-density correlation length (longitudinal spin-spin CL in the spin picture) for $\Delta = 0.5$ is shown. The numerical result could be smaller or larger than the exact result but the absolute error remains of the order 10^{-3} over a wide temperature range. In the low-temperature regime the numerically calculated correlation length becomes typically too small meaning that the gap between leading and next leading eigenvalue of the QTM is overestimated (see Eq. (2.34)).

Summarizing, we have identified two main sources for errors in TMRG calculations: The mapping of the quantum chain to a 2D classical model with finite Trotter parameter ϵ leads to errors of the order ϵ^2 in the partition function and the free energy in both algorithms and dominates at high and intermediate temperatures. In the low-temperature regime the error due to the truncation of the Hilbert space becomes dominant and the accuracy of the numerical data is determined by the number of states N kept within the RG. Additionally, we have shown that the numerical errors are of the same order in the free and in the interacting case. In both cases we have settled that correlation lengths are determined accurately by the numerically calculated ratio of eigenvalues of the QTM. In the free fermion case we could show in addition that not only the asymptotics of correlation functions but also static correlation functions themselves are directly accessible within TMRG. In the first section of the next chapter we will compare again exact and numerical results for the supersymmetric t-J model which is also solvable by Bethe ansatz.

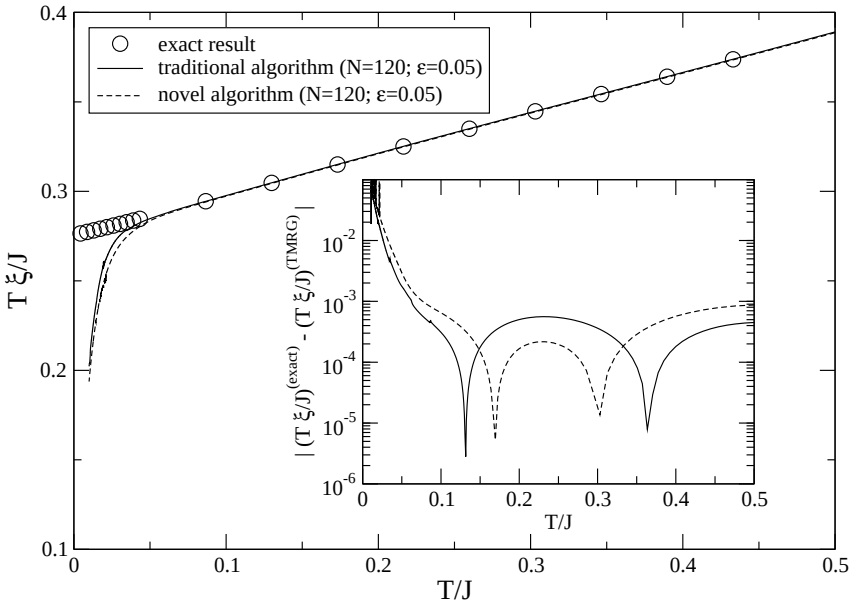

Figure 4.7: Correlation length for the XXZ-model with $\Delta = 0.5$. The exact result shows a linear behaviour of $T\xi$ in the displayed temperature range as expected from CFT. In the inset the deviations of the numerical results from a linear fit of the exact data are shown. Down to $T/J \approx 0.05$ the errors remain always smaller than 10^{-3} in both algorithms. The cusps in the logarithmic representation are caused by crossings of numerical and exact results.

Chapter 5

t-J Model

The t-J model is one of the most fundamental systems of strongly correlated electrons. The two-dimensional version has attracted much attention because it is believed that it describes the basic interactions in the copper-oxygen planes of high-T_c superconductors. For the one-dimensional (1D) t-J model much progress has been achieved by using various analytical and numerical techniques [34,35,36,37,38,39,40,41,42]. At the supersymmetric point $J/t = 2$ the model is solvable by the Bethe ansatz and ground state properties as well as the excitation spectra have been obtained exactly [36]. Because the two critical excitations of spin and charge type are separated, the properties can be described by two independent $c = 1$ Virasoro algebras. By a combination of finite-size results from the Bethe ansatz and conformal field theory (CFT) it is therefore also possible to calculate the critical exponents of algebraically decaying correlation functions [37, 38]. This explicitly shows that the t-J model at the supersymmetric point behaves as a Tomonaga-Luttinger liquid (TLL) for all electron densities. Thermodynamic quantities at this special point have been obtained by thermodynamic Bethe ansatz [43] as well as by a combination of a Trotter-Suzuki mapping leading to a quantum transfer matrix (QTM) and the Bethe ansatz [39]. Exact results are also available in the limit $J/t \to 0$ where the t-J model is equivalent to the Hubbard model with $U/t \to \infty$, showing again TLL behaviour [44]. It is therefore believed that the t-J model shows TLL properties for all $0 \leq J/t \leq 2$, which is supported by various numerical calculations [34, 35, 40, 41]. In these numerical works there is also general agreement that the t-J model phase separates for $J/t = 2.8$ to 3.5 depending on the electron density.

Already Ogata *et al.* [34] conjectured a third phase with a spin gap in the low-density region for $J/t > 2$. However, by calculating the spin susceptibility for an electron density $n = 1/3$ on small chains no evidence for a spin gap was found. Also the variational quantum Monte Carlo (QMC) calculations of Hellberg and Mele [35] could not confirm the appearance of a spin gap. By using the same method but other trial wave functions a phase with Luther-Emery (LE) properties was found by Chen and Lee [40] and Kobayashi *et al.* [41] at low densities and $2 < J/t < 3.1$. However, the obtained result strongly depends on the trial wave functions used in the calculations. Completely different phase boundaries with the spin-gap phase extending into the high density region have been obtained by Nakamura *et al.* [42], using a renormalization group treatment of the Tomonaga-Luttinger model under the assumption that the spin gap is caused by an attractive backward scattering process. They argue that the spin gap was underestimated in the numerical calculations because it is the result of a marginal operator leading to an exponentially small gap. The phase diagram of the one-dimensional t-J model obtained by these different methods is shown in Fig. 5.1.

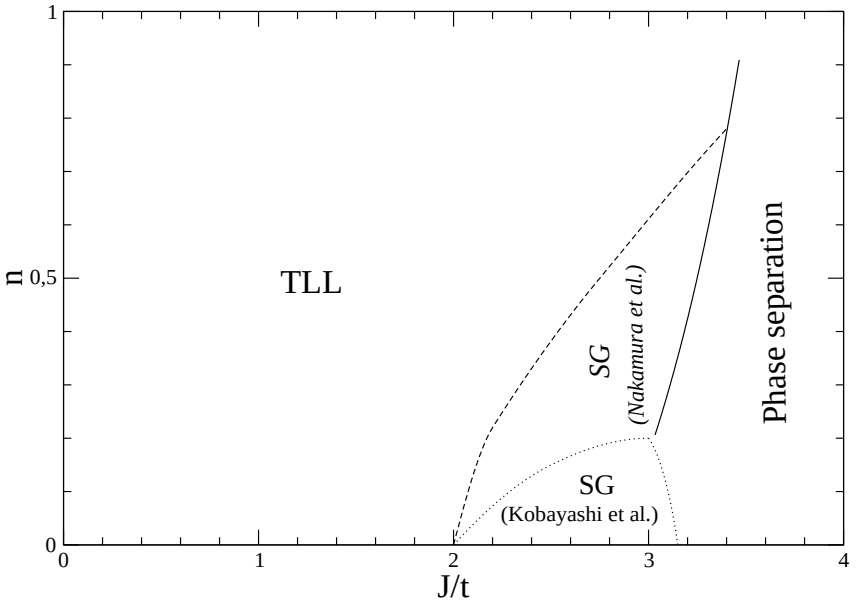

Figure 5.1: The figure shows a sketch of the t-J model phase diagram. Over a wide parameter region the model shows Tomonaga-Luttinger liquid (TLL) properties. Whereas general agreement exists about the boundary of the phase separated state (solid line), the boundaries of the spin gap (SG) phase are still controversial. The dashed line sketches the phase boundary obtained by Nakamura *et al.* [42] whereas the dotted line denotes the boundary obtained by Kobayashi *et al.* [41].

The aim of the work presented here is to examine thermodynamics of the one-dimensional t-J model in the whole J/t-parameter region. In particular, we are interested in the temperature dependence of correlation lengths. We use a grandcanonical description of the model, where the Hamiltonian is given by

$$H = -t\sum_{i,\sigma} P(c^\dagger_{i,\sigma}c_{i+1,\sigma}+c^\dagger_{i+1,\sigma}c_{i,\sigma})P+J\sum_i\left(\boldsymbol{S}_i\boldsymbol{S}_{i+1}-\frac{n_in_{i+1}}{4}\right)-h\sum_i S^z_i-\mu\sum_i n_i \quad (5.1)$$

with a magnetic field h, a chemical potential μ and P being the projection operator onto the Hilbert-subspace without double occupancy. Compared to alternative approaches like QMC calculations, which are difficult to perform due to the negative sign problem in fermionic systems, or field theoretical methods, which are restricted to the low temperature regime, the TMRG algorithm is particularly suited. The numerical calculations are again simplified as explained in section 2.2 (see especially Eq. (2.44)) due to the conservation laws for spin and particle number, or equivalently, for the number of particles with spin up ($N_\uparrow$) and spin down ($N_\downarrow$).

As in chapter 4, we will compare again the numerics with exact results. We start therefore in Sec. 5.1 with the supersymmetric point, where various thermodynamic quantities have been calculated by Jüttner *et al.* [39] using the Bethe ansatz. Because correlation lengths have not been obtained by BA yet, we compare the numerical results for correlation lengths and static correlation functions with CFT predictions by Kawakami and Yang

[37, 38] in detail. The t-J model is realized by the Hubbard model in the limit $U \gg t$ so that the case $J = 2t^2/|U| < t$ is physically very relevant. Results for $J/t = 0.35$, a value often used in literature, are given in Sec. 5.2. As already mentioned the t-J model phase separates for J/t large. The meaning of this in the grand-canonical ensemble is explained in Sec. 5.3. Without using any assumption about the ground state or the low energy effective theory, the existence of a LE phase is proved in Sec. 5.4 by calculating directly spin susceptibilities as well as spin-spin and density-density correlation lengths. In Sec. 5.5 we study the t-J model with an additional Ising-like anisotropy. The final section is devoted to a brief summary and some conclusions.

5.1 The supersymmetric point

In the following we always choose the same three chemical potentials corresponding in the low-temperature limit to a high, medium and low electron density (see Fig. 5.2) and calculate several thermodynamic quantities for comparison with Bethe ansatz results [39]. Obviously the particle density n at a given chemical potential depends on temperature.

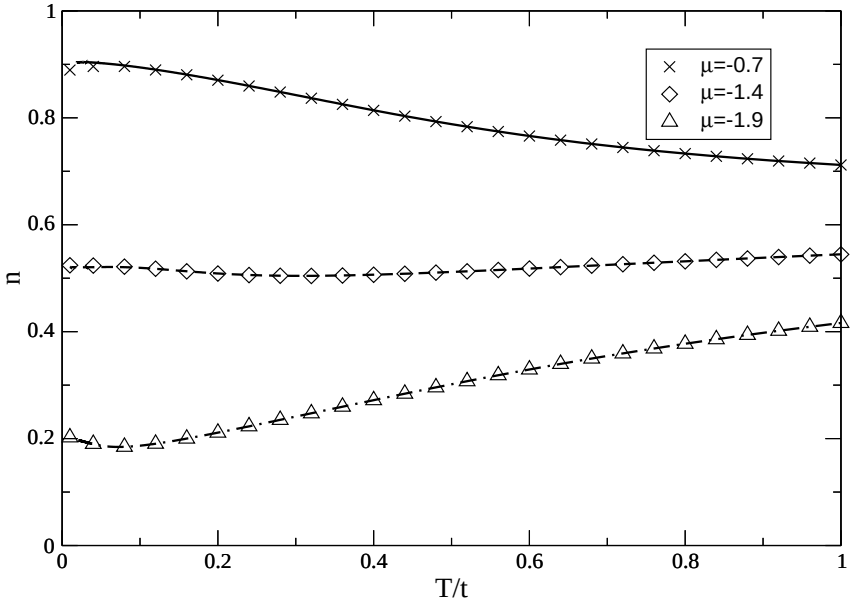

Figure 5.2: Temperature dependence of the density for three different chemical potentials. The lines are given by the TMRG results, whereas the symbols denote the results from the Bethe ansatz.

Counting the degrees of freedom per lattice site immediately implies $n = 2/3$ for any finite μ in the limit $T \to \infty$ whereas the density at finite temperature is given by $n = n(\mu, T)$. The free energies calculated with $N = 100$ states retained in the DMRG algorithm and $\epsilon = 0.05$ and their deviations from the exact results are shown in Fig. 5.3. In all three cases the accuracy is of the order 10^{-4} if $T/t > 0.1$. For lower temperatures $0.01 \leq T/t \leq 0.1$

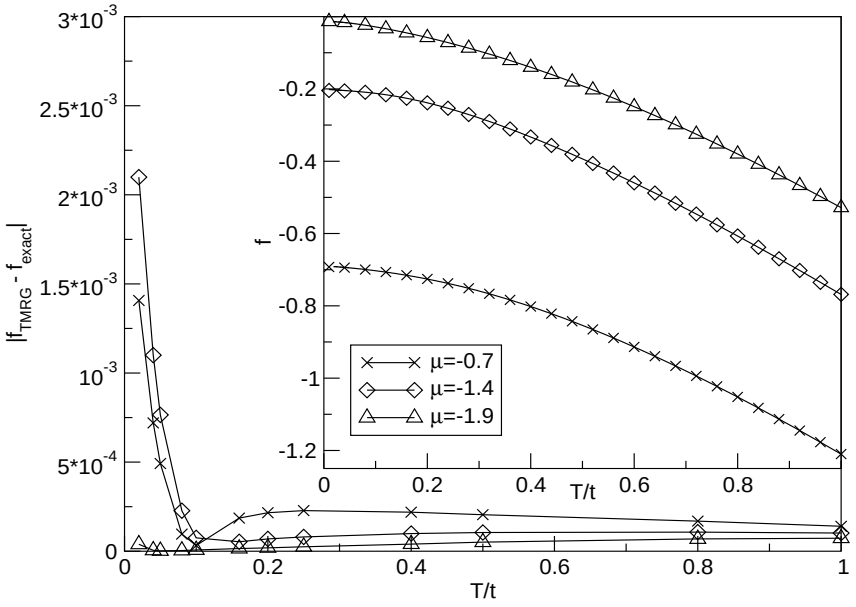

Figure 5.3: Deviation of the free energies calculated by means of TMRG in comparison to the exact results for different temperatures. The lines are guide to the eye. The inset shows the Bethe ansatz results (symbols) and the TMRG results (lines).

the errors for the medium and high electron density grow up to 10^{-3} whereas the error in the low density case remains of the same order. Note that the t-J model has a three-dimensional local Hilbert space (e.g. empty site, spin up, spin down as basis set) whereas it is only two-dimensional for the free spinless fermion model and XXZ-model considered in chapter 4. Therefore more states N are needed to obtain the same accuracy. However, the accuracy obtained with $N = 100$ states is sufficient for our purposes. From CFT it is known that the low-temperature asymptotics is given by

$$f = e_0 - \frac{\pi}{6}\left(\frac{c_s}{v_s} + \frac{c_c}{v_c}\right) T^2 \tag{5.2}$$

where $v_{s,c}$ are the velocities of the spinon and holon excitations, respectively. Here the central charges $c_{s,c}$ are equal to 1. According to Eq. (5.2) we have fitted the numerical data and tried to determine the errors of the fit parameters by a variation of the fit region from $T/t \in [0.01 : 0.02]$ to $T/t \in [0.01 : 0.05]$. The estimates for the ground-state energies e_0 coincide with the exact results with deviations that are slightly larger than the errors calculated by the fit procedure (see table 5.1). The remaining deviation is due to systematic errors. The parameter $1/v_s + 1/v_c$ is difficult to obtain from such a fit because the extent of the low-temperature region in which Eq. (5.2) is valid is very small (see Bethe ansatz results in Fig. 5.4), which makes it necessary to restrict the fit to the temperature region defined above. In such a small interval, however, a change of the parameter $1/v_s + 1/v_c$ by a factor of 2 corresponds to deviations in the fitted free energy of the order 10^{-3} only, so that the TMRG data are not accurate enough to determine this parameter. However, it is possible to calculate the velocities from TMRG by using the

μ	v_c	v_s	$(1/v_s + 1/v_c)^{\text{exact}}$	$(1/v_s + 1/v_c)^{\text{fit}}$
-0.7	0.526	2.778	2.261	3.90 ($\pm$ 0.61)
-1.4	1.061	1.713	1.526	2.90 ($\pm$ 0.64)
-1.9	0.579	0.657	3.249	3.66 ($\pm$ 0.14)

μ	e_0^{exact}	e_0^{fit}
-0.7	-0.69114	-0.6908 $\pm$ 0.0002
-1.4	-0.20373	-0.2033 $\pm$ 0.0002
-1.9	-0.01320	-0.0133 $\pm$ 0.0001

Table 5.1: Velocities $v_{s,c}$ and ground-state energies e_0 from the Bethe ansatz in comparison to values from a fit of the numerical data. The errorbars of e_0 and $1/v_s + 1/v_c$ correspond to the described variation of the fit region, but the errors for $1/v_s + 1/v_c$ are in fact much larger (see explanation in the main text).

results for the susceptibilities and correlation lengths to be discussed later on. We will not pursue this further because the estimation of v_s and v_c is not our main goal.

To calculate the specific heat c_n, we first have to calculate the entropy S. This can be done by using the relation $S = (u - f)/T$, where the inner energy u is directly calculated in the TMRG algorithm as a local expectation value (see Eq. (2.30)) or alternatively, by the numerical derivative $S = -\partial f/\partial T$. At first sight it seems better to calculate the entropy without using numerical derivatives, but a local expectation value directly involves the eigenvectors of the QTM which are generally less accurate than the corresponding eigenvalues. By comparing both results with the exact ones we have convinced ourselves that the numerical derivative leads to more accurate results. Because in the calculations only the chemical potential μ but not the particle density n can be fixed, we calculate the specific heat by using the thermodynamic relation

$$c_n = T \left(\frac{\partial S}{\partial T}\right)_n = T \left[\left(\frac{\partial S}{\partial T}\right)_\mu - \left(\frac{\partial n}{\partial T}\right)_\mu^2 \left(\frac{\partial n}{\partial \mu}\right)_T^{-1} \right] . \tag{5.3}$$

The second term is again evaluated using numerical derivatives. This procedure enhances the numerical errors, but we are able to reproduce the exact results within errors of the order 10^{-3} down to temperatures of $T/t \approx 0.2$ as shown in Fig. 5.4. The CFT result for the free energy, Eq. (5.2), leads to a linear temperature dependence of the specific heat at low temperatures with a coefficient given by $\pi(1/v_c + 1/v_s)/3$. The Bethe ansatz results clearly show this linear behaviour at very low temperatures, but within the TMRG this temperature region is not accessible because of the errors caused by the numerical derivatives used in Eq. (5.3).

To calculate the spin susceptibility χ_s, a small magnetic field $h = 10^{-2}$ is applied. From the resulting magnetization m the susceptibility at vanishing magnetic field is evaluated by

$$\chi_s\big|_{h=0} = \frac{m}{h} . \tag{5.4}$$

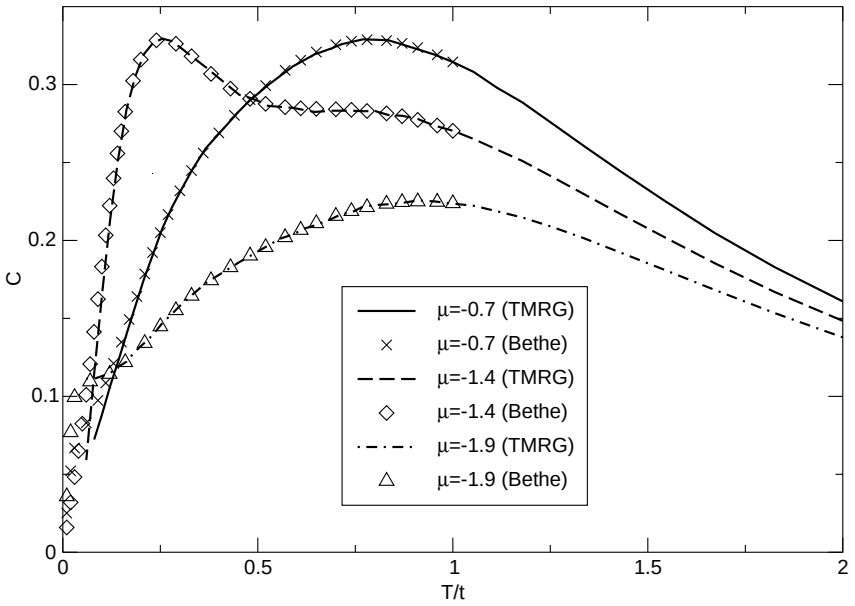

Figure 5.4: Specific heats as calculated by means of TMRG and Eq. (5.3) (lines) and exact results by Bethe ansatz (symbols). Note the two peak structure caused by spin-charge separation as explained in the text.

Similarly the charge susceptibility χ_c or compressibility is given by

$$\chi_c = \frac{\partial n}{\partial \mu} \,, \tag{5.5}$$

where again numerical derivatives are used and the variation of μ is typically of the order 10^{-2}. Here we are able to reproduce the exact results down to temperatures of $T/t = 0.01$ as shown in Fig. 5.5. The high temperature asymptotics of the spin susceptibility is given by the pure paramagnetic part $\chi_s(T \to \infty) \sim 2s(s+1)/9T$ which is easily understood when χ_s is expressed as a sum of two-point spin correlations. For $T = 0$ the spin susceptibility has a finite value as expected from the linear dispersion of the spinon excitations. Within CFT the zero temperature value is given explicitly by $\chi_s = 1/(2\pi v_s)$ in good agreement with the numerical results. The maxima at finite temperatures are determined by the band structure. The charge susceptibility is given in the same way as sum over two-point density-density correlations leading to the high-temperature asymptotics $\chi_c \sim 2/9T$. For $T = 0$ the charge susceptibility is again given by CFT as $\chi_c = \xi_c^2(Q)/(\pi v_c)$ with $\xi_c(Q)$ being the dressed charge. Note that the charge susceptibility is diverging for $T \to 0$ in the two limiting cases $n \to 0$ and $n \to 1$, because $v_c \to 0$ in both cases. The spin susceptibility χ_s shows different behaviour with divergence for $T \to 0$ only in the limiting case $n \to 0$ as only here $v_s \to 0$.

To summarize our numerical findings for c, χ_s and χ_c in a qualitative manner we may use a picture of the ground state as a "liquid" consisting of bound singlet pairs of electrons. Above this ground state there are two different elementary excitations. First, a momentum transfer onto any individual pair is possible by keeping the bound pair intact (holon

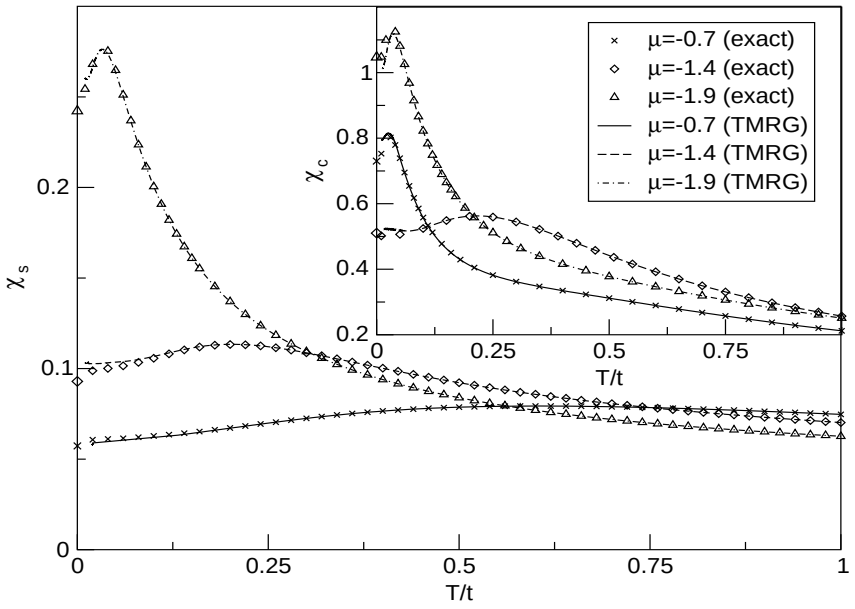

Figure 5.5: The main figure shows the spin susceptibilities, the inset the charge susceptibilities (compressibilities), where again lines denote the numerical results and symbols the exact ones. The symbols at $T = 0$ denote the CFT results in both graphs.

excitation). Second, a breaking of any bound pair into its components (electrons) with the two spin-1/2 objects coupling either to $S = 0$ or 1 (spinon excitation). Once the "free" electrons are produced by spinon excitations, they may acquire momentum and energy individually, which we refer to as incoherent single particle motion. Basically, any structure observed in the T-dependence of c, χ_s and χ_c can be attributed to the saturation of a particular type of excitation. In χ_s (χ_c) we see a finite temperature maximum at a temperature of the order of v_s (v_c). Note that the characteristic holon temperature is always lower than or equal to the spinon temperature. This is rather natural as the saturation of spinons is marked by the practical absence of pairs such that saturation of holon excitations must have occurred at lower or equal temperature. In principle, these structures are also visible in the specific heat. In most cases, however, only the spin-maximum is clearly noticeable. For generic densities the small holon-maximum disappears in the low temperature regime of $c(T)$ with rather steep slope due to the spinon-excitations. At lower densities the holon and spinon structures are located at similar temperatures. In all cases, the higher temperature region is dominated by a broad maximum due to incoherent single particle motion. The corresponding energies are of the order of spinon excitations at particle densities close to 1, in which case the structures merge.

5.1.1 Correlation lengths

For the correlation lengths of the supersymmetric t-J model no exact results are available yet.[1] However, in Fig. 4.4 we have shown that TMRG yields reliable results for the density-density correlation length of the free spinless fermion model down to temperatures $T/t \sim 0.1$. Because the free fermion model is hard to tackle within the DMRG scheme due to the rapidly decaying spectrum of the reduced density matrix, we believe that for the t-J model a similar or even better accuracy is obtained.

We now concentrate on the calculation of correlation lengths for the supersymmetric t-J model to study the crossover from the *high-T lattice* into the *quantum critical regime* determined by $T \ll t$. In the high-T lattice region we expect non-universal properties dependent on the microscopic Hamiltonian H whereas the quantum critical regime should show universal TLL properties. Respecting the selection rules, the density-density (d-d CLs) and longitudinal spin-spin correlation lengths (s-s CLs) are in the block of the QTM with unchanged quantum numbers $\Delta N_\uparrow = \Delta N_\downarrow = 0$, where $N_\uparrow$ ($N_\downarrow$) denotes the number of particles with spin up (down). To distinguish between them, the matrixelement M_n in Eq. (2.33) has to be calculated explicitly. With zero magnetic field and isotropic spin interactions, it turns out that M_n is either non-zero for the density or for the S^z operator so that all d-d and s-s CLs are different from each other. This is a consequence of the $SU(2)$ spin symmetry. If a magnetic field is applied, this symmetry is broken and less stringent selection rules apply so that all eigenvalues discussed above contribute to the s-s as well as to the d-d correlation function. On the other hand the singlet pair operator $P_i^s = c_{\uparrow,i+1} c_{\downarrow,i}$ changes the quantum numbers by $\Delta N_\uparrow = \Delta N_\downarrow = \pm 1$ and the eigenvalues corresponding to the singlet pair CLs are found in the block with these quantum numbers. The leading d-d and s-s CLs (times temperature) and the corresponding wavevectors for $J/t = 2.0$, $\mu = -1.4$ and zero magnetic field are shown in Fig. 5.6. Remember again that several CLs ξ with the same wavevector k can appear in the asymptotic expansion displayed in Eq. (2.33) and that each term yields a (measurable) Lorentz function in the structure factor as shown in Eq. (2.35).

At high temperatures the largest s-s CL is given by a real negative eigenvalue leading to π-oscillations. However, at a well defined crossover temperature $T_c \approx 0.8$ a real, positive eigenvalue becomes largest, which is associated with $k = 0$. Regarding only the largest spin CL this means that there is a non-analyticity at T_c. We want to point out that any thermodynamic quantity derived from the free energy is an analytic function at finite T. Phase transitions and corresponding singularities only occur at $T = 0$. However, quantities describing the *asymptotics of correlation functions* (i.e. CL) may show non-analyticities even at finite temperature. Such crossovers between CLs are characteristic for the non-universal high-T lattice regime whereas no crossovers are expected in the universal quantum critical regime described by CFT. The second largest spin CL is given at low temperatures by a pair of complex conjugated eigenvalues. Complex eigenvalues always appear in pairs, because the QTM is non-symmetric but real, and lead to incom-

[1] In principle, it is possible to obtain correlation lengths using Bethe ansatz by expanding the approach described in [39] to the next-leading eigenvalues of the QTM.

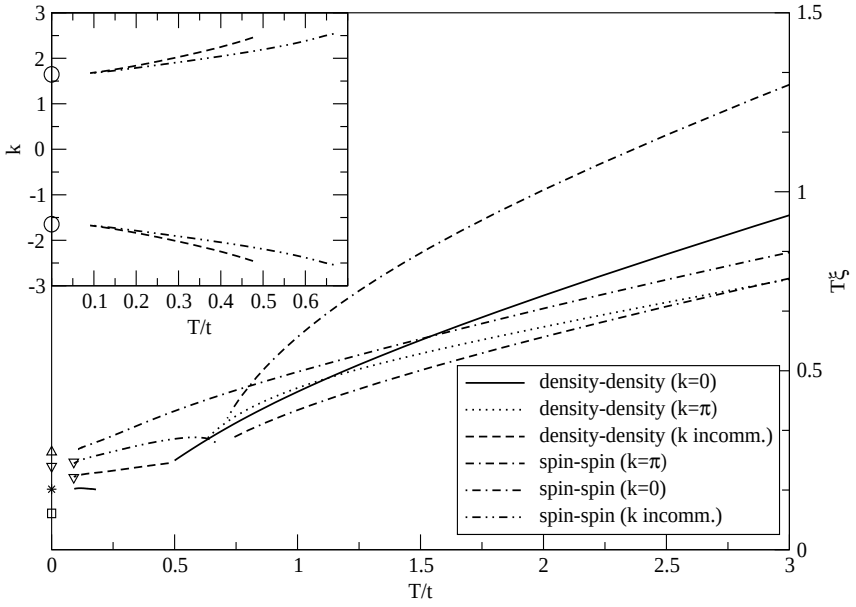

Figure 5.6: Temperature dependence of the leading d-d and s-s CLs for $J/t = 2.0$ and $\mu = -1.4$. The triangle up (star) gives the zero temperature result from CFT for the non-oscillating s-s (d-d) and the square that for the $4k_F$ part of the d-d. The triangle down at zero temperature denotes the CFT value for the $2k_F$ part of s-s and d-d, whereas the triangles down at $T/t = 0.1$ are given by CFT plus logarithmic corrections as described in the text. The inset shows the wavevectors k in the case of incommensurate oscillations. The circles denote the values for $k = \pm 2k_F$ at zero temperature as expected from CFT.

mensurate oscillations, i.e. $k \neq 0, \pi$. An incommensurate wavevector k is depending on temperature as seen in the inset of Fig. 5.6. The leading d-d CL shows no oscillations at high temperatures but is crossed at lower temperatures by a real, negative eigenvalue leading to π-oscillations before the non-oscillating part dominates again. Below $T_c \approx 0.5$ the largest d-d CL is given by a complex eigenvalue pair. The wavevector for this incommensurate part is again shown in the inset of Fig. 5.6.
It is illuminating to regard the free spinless fermion case again. For such a system the CLs have been calculated in appendix B and Eq. (B.12a) shows that a non-oscillating part and a part with $k = \pi$ arise, both with a CL given by $\xi^{-1} = 2\,\mathrm{arcsinh}(\pi T)$. Therefore the CLs at high temperature behave as $\xi^{-1} \sim \ln(T)$ consistent with the numerical results here because the interaction becomes irrelevant at temperatures $T \gg J$. In the low temperature limit it follows that $\xi^{-1} \sim 1/(2\pi T)$ which is expected from CFT when the velocity v and the scaling dimension x are equal to 1. The matrixelement for the CL is given by $M = 2/(\pi^2 + \beta^2)$ indicating that $M \to 0$ when $T \to 0$. This is reasonable because at zero temperature the CLs diverge and the matrixelements have to approach zero so that the series in Eq. (2.33) is not diverging but sums up to an algebraic function. The numerical results also show that the matrixelements $M_n \to 0$ if $T \to 0$. To understand the behaviour of the CLs at low temperatures in detail it is useful to regard the results from the Bethe ansatz and the finite-size scaling technique in CFT at zero temperature [37,38].

In general, a two-point correlation function of the *scaling fields* $\phi_{\Delta^\pm}(r,\tau)$ with *conformal weights* $\Delta^\pm$ is given by

$$\begin{aligned} & \langle \phi_{\Delta^\pm}(r,\tau)\phi_{\Delta^\pm}(0,0)\rangle \qquad (5.6a) \\ = & \frac{\mathrm{e}^{\mathrm{i}(2\pi-2k_{F\uparrow}-2k_{F\downarrow})D_c\, r}\ \ \mathrm{e}^{\mathrm{i}(2\pi-2k_{F\uparrow})D_s\, r}}{(r-\mathrm{i}v_c\tau)^{2\Delta_c^+}(r+\mathrm{i}v_c\tau)^{2\Delta_c^-}(r-\mathrm{i}v_s\tau)^{2\Delta_s^+}(r+\mathrm{i}v_s\tau)^{2\Delta_s^-}} \end{aligned}$$

where the conformal weights are determined by quantum numbers of the elementary excitations. Considering here only the case of vanishing magnetic field and using the notation of Ref. [37, 38], the conformal weights reduce to a simple form

$$\Delta_c^\pm(\boldsymbol{I},\boldsymbol{D}) = \frac{1}{2}\left(\frac{I_c}{2\xi_c(Q)} \pm \xi_c(Q)\left(D_c+\frac{D_s}{2}\right)\right)^2 + N_c^\pm \qquad (5.6b)$$

$$\Delta_s^\pm(\boldsymbol{I},\boldsymbol{D}) = \frac{1}{4}\left(I_s - \frac{I_c}{2} \mp D_s\right)^2 + N_s^\pm\,. \qquad (5.6c)$$

$\xi_c(Q)$ is the dressed charge which can be calculated explicitly by solving an integral equation and $(I_c, I_s, D_c, D_s, N_c, N_s)$ are quantum numbers of the excitation. To be specific, I_c counts the total number of holes, I_s the number of holes with respect to the up spins, D_c (D_s) the number of holons (spinons) being transferred from one Fermi point to the other and N_c (N_s) the number of charge (spin) particle-hole excitations. The Fermi momentum $k_{F\uparrow(\downarrow)}$ for up (down) spin electrons is given by

$$k_{F\uparrow(\downarrow)} = \frac{\pi}{2}(n \pm 2m) \qquad (5.6d)$$

where m is the magnetization. If no magnetic field is applied then $k_{F\uparrow} = k_{F\downarrow} = k_F$. As shown in Fig. 5.2 the density in the zero temperature limit for $\mu = -1.4$ is approximately $n_{T\to 0} \approx 0.524$ and therefore $k_F \approx 0.823$. In the inset of Fig. 5.6 the circles denote $k = \pm 2k_F$ at zero temperature indicating that the leading d-d and s-s CLs with incommensurate oscillations correspond to the $2k_F$-oscillating part. From Eq. (5.6a) we derive

$$\begin{aligned} \langle n(r)n(0)\rangle \ &= \ \text{const.} + A_0 r^{-2} + A_2 r^{-\alpha_c}\cos(2k_F r) \\ & \quad + A_4 r^{-\beta_c}\cos(4k_F r) \qquad (5.7a) \end{aligned}$$

for the equal-time d-d correlation, where A_i are matrixelements. The non-oscillating part is due to the lowest particle-hole excitation $(0,0,0,0,1,0)$, the $2k_F$ part due to a $(0,0,\pm 1,\mp 1,0,0)$ excitation, while the $4k_F$ part arises from the excitation $(0,0,\pm 1,0,0,0)$. Thus, the critical exponents can be calculated from Eq. (5.6b,5.6c) leading to

$$\alpha_c = 1 + \frac{\xi_c^2(Q)}{2} \qquad , \qquad \beta_c = 2\xi_c^2(Q)\,. \qquad (5.7b)$$

The equal-time s-s correlation has the same form as Eq. (5.7a), but the constant as well as the $4k_F$ part are absent and the matrixelements are different. The critical exponent of

the $2k_F$ part is the same but the corresponding excitation is now $(0,0,0,\pm1,0,0)$.[2] As shown in Ref. [37, 38] the dressed charge $\xi_c(Q)$ varies between $\sqrt{2}$ for $n=0$ and 1 at half-filling. Thus, α_c is always the smallest critical exponent and therefore the $2k_F$ parts of the correlation functions dominate at zero temperature.

The results for the correlation functions shown here are absolutely consistent with TLL theory when the identification

$$K_\rho = \frac{\xi_c^2(Q)}{2} \tag{5.8}$$

is used. For the Tomonaga-Luttinger model it is also possible to calculate multiplicative logarithmic corrections to the algebraic terms of Eq. (5.7a), which are not directly accessible within Bethe ansatz and CFT. It turns out that the $2k_F$ parts of the d-d and the s-s correlation have different logarithmic corrections given by $\ln^{-3/2} r$ ($\ln^{1/2} r$) for the d-d (s-s) correlation [45].

The asymptotics of correlation functions at small finite temperature can still be obtained from conformal invariance by the usual mapping of the complex plane onto a strip of width $1/T$ with periodic boundary conditions. Eq. (5.6a) is then replaced by

$$\begin{aligned} & \exp\left[\mathrm{i}(2\pi - 2k_{F\uparrow} - 2k_{F\downarrow})D_c r\right] \ \exp\left[\mathrm{i}(2\pi - 2k_{F\uparrow})D_s r\right] \\ \times \ & \left(\frac{\pi T}{v_c \sinh(\pi T(r - \mathrm{i}v_c\tau)/v_c)}\right)^{2\Delta_c^+} \left(\frac{\pi T}{v_c \sinh(\pi T(r + \mathrm{i}v_c\tau)/v_c)}\right)^{2\Delta_c^-} \\ \times \ & \left(\frac{\pi T}{v_s \sinh(\pi T(r - \mathrm{i}v_s\tau)/v_s)}\right)^{2\Delta_s^+} \left(\frac{\pi T}{v_s \sinh(\pi T(r + \mathrm{i}v_s\tau)/v_s)}\right)^{2\Delta_s^-} . \end{aligned} \tag{5.9}$$

For $r \gg 1$ this equation can be further simplified and we finally obtain

$$\begin{aligned} & \langle \phi_{\Delta^\pm}(r,\tau)\phi_{\Delta^\pm}(0,0)\rangle \\ = \ & \left(\frac{2\pi T}{v_c}\right)^{2x_c} \left(\frac{2\pi T}{v_s}\right)^{2x_s} \exp\left[-2\pi T\left(\frac{x_c}{v_c} + \frac{x_s}{v_s}\right) r\right] \\ \times \ & \exp\left[\mathrm{i}(2\pi - 2k_{F\uparrow} - 2k_{F\downarrow})D_c r\right] \ \exp\left[\mathrm{i}(2\pi - 2k_{F\uparrow})D_s r\right] \\ \times \ & \exp\left[2\pi T\mathrm{i}(\Delta_c^+ - \Delta_c^-)\tau\right] \exp\left[2\pi T\mathrm{i}(\Delta_s^+ - \Delta_s^-)\tau\right] , \end{aligned} \tag{5.10}$$

with *scaling dimensions* $x_{c,s} = \Delta_{c,s}^+ + \Delta_{c,s}^-$. Thus, all CLs diverge in the low temperature limit as

$$\xi = \frac{1}{2\pi T\left(\frac{x_c}{v_c} + \frac{x_s}{v_s}\right)} = \frac{\gamma}{T} \tag{5.11}$$

where the coefficient $\gamma = v_s/2\pi$ ($\gamma = v_c/2\pi$) for the non-oscillating part of the s-s (d-d) CL,

$$\gamma = \frac{2v_c}{\pi\left(2\frac{v_c}{v_s} + \xi_c^2(Q)\right)} \tag{5.12a}$$

[2]The excitations $(0,0,\pm1,\mp1,0,0)$ and $(0,0,0,\pm1,0,0)$ lead to the same critical exponent but they can be distinguished by applying a magnetic field because the first shows $2k_{F\downarrow}$-oscillations whereas the second oscillates with $2k_{F\uparrow}$.

for both $2k_F$ parts whereas

$$\gamma = \frac{v_c}{2\pi\xi_c^2(Q)} \tag{5.12b}$$

for the $4k_F$ part of the d-d CL. Contrary to zero temperature the answer to the question which part dominates depends not only on the scaling dimensions $x_{s,c}$ but also on the velocities $v_{s,c}$! In Fig. 5.6 the values for these γ's are denoted by symbols at $T = 0$ showing good agreement for the non-oscillating parts between the numerics and the CFT results. The $4k_F$-oscillating d-d CL is so small that it is difficult to be obtained numerically. From Eq. (5.12a) the $2k_F$ s-s and d-d CLs are expected to be equal in the low-temperature limit. However, the numerical result shows that they are well separated even at the lowest accessible temperatures. This is a consequence of the different logarithmic corrections stated above. Quantitatively we can regard a multiplicative logarithmic term $\ln^\alpha r$ as an effective, distance dependent correction of the scaling dimension:

$$x' = x - \frac{1}{2}\frac{\ln(\ln^\alpha r)}{\ln r} \tag{5.13}$$

The relevant length scale is given by the correlation length at the considered temperature, $r \approx \xi(T)$. Using this correction together with Eq. (5.11) leads to splitting of the $2k_F$ s-s and d-d CL at finite temperature and to an excellent agreement with the numerical results (see triangle downs in Fig 5.6).

Next, we regard the singlet pair CLs shown in Fig. 5.7. The CL leading over the entire

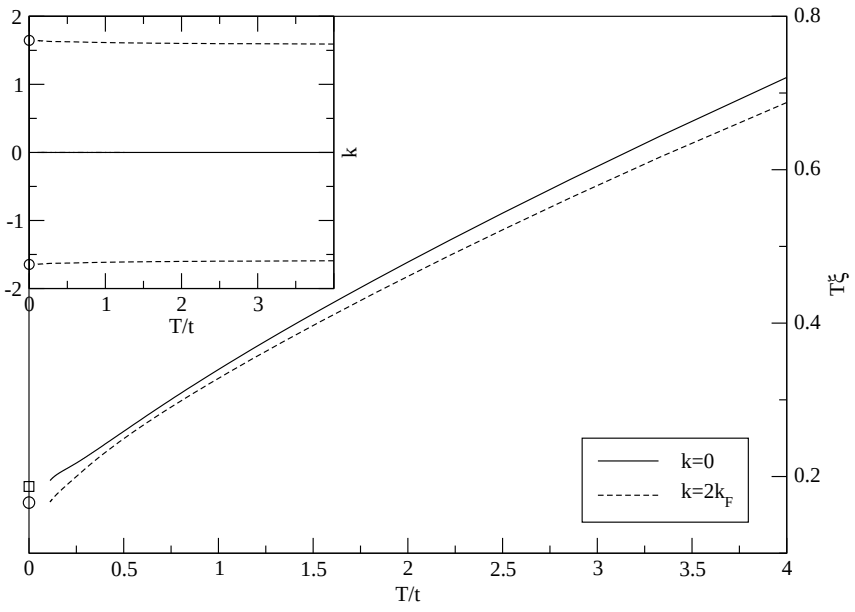

Figure 5.7: Leading singlet pair correlation lengths for $J/t = 2.0$ and $\mu = -1.4$. The square at $T = 0$ denotes the CFT result for the non-oscillating part, the circle that for the $2k_F$ part. The inset shows the corresponding wavevectors.

temperature range is non-oscillating, whereas the next-leading shows incommensurate

oscillations. Again the zero temperature result from Eq. (5.6d) identifies this contribution as the $2k_F$ part. The form of the algebraically decaying singlet pair correlation $P_s(r,0)$ at zero temperature is given by CFT

$$P_s(r,0) = C_0 r^{-\delta_p} + C_2 r^{-\epsilon_p} \cos(2k_F r) \,. \tag{5.14a}$$

The non-oscillating term is due to the excitation $(2,1,\pm 1/2,\mp 1,0,0)$ leading to an exponent

$$\delta_p = 1 + \frac{2}{\xi_c^2(Q)} \tag{5.14b}$$

and the $2k_F$ part due to the excitation $(2,1,\pm 1/2,0,0,0)$ leading to

$$\epsilon_p = \frac{2}{\xi_c^2(Q)} + \frac{\xi_c^2(Q)}{2} \,. \tag{5.14c}$$

Thus, the coefficient γ in Eq. (5.11) is now

$$\gamma = \frac{v_c}{\pi \left(\frac{2}{\xi_c^2(Q)} + \frac{v_c}{v_s} \right)} \tag{5.15a}$$

for the non-oscillating part, whereas

$$\gamma = \frac{v_c}{\pi \left(\frac{2}{\xi_c^2(Q)} + \frac{\xi_c^2(Q)}{2} \right)} \tag{5.15b}$$

for the $2k_F$ part. The value for the non-oscillating part is again in good agreement with the numerical results whereas the numerically accessible temperature range is not sufficient to compare the $2k_F$ part with CFT (see symbols in Fig. 5.7).

To illustrate the dependence of the leading s-s and singlet-pair CL on electron density, there are plots for three different chemical potentials in Fig. 5.8. The s-s CL is largest for the Heisenberg case ($n = 1$) and gets suppressed, as expected, with an increasing concentration of holes. On the other hand the singlet-pair CL is nearly independent of the particle density. The s-s CL shows a non-analyticity at a temperature T_c, where the $k = \pi$ part is crossed by the non-oscillating part. With increasing particle density this non-analyticity is shifted to lower temperatures and disappears for chemical potentials $\mu > -0.47$. Therfore no singularity is visible in the Heisenberg limit of the t-J model. T_c as a function of the chemical potential shows an algebraic behaviour. A very similar phenomenon is described in Ref. [33], where the s-s CL of the 1/2-XXZ chain in a magnetic field is investigated. In this case the magnetic field plays the same role as the chemical potential here. However, the singularity there is associated with a crossover from commensurate oscillations at $T > T_c$ to incommensurate oscillations at $T < T_c$. Recently, temperature dependent CLs have also been studied analytically in a generalized Hubbard model related to the supersymmetric t-J model [46].

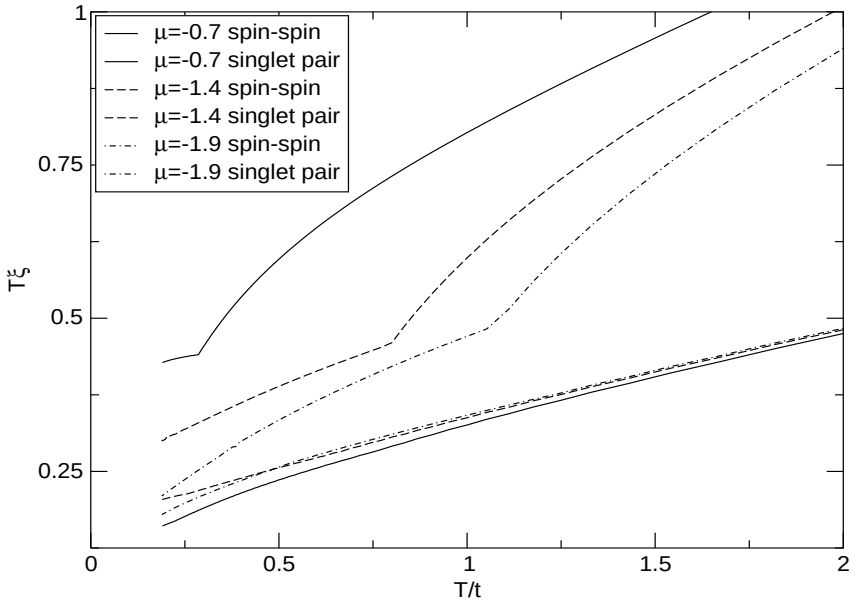

Figure 5.8: The three upper curves show the spin correlation lengths, the other three the singlet pair-pair correlation lengths.

5.1.2 Static correlation functions

Next, we want to calculate static correlation functions as defined in Eqs. (2.36), (2.37), (2.38) with the TMRG algorithm. Note that the static correlation function is calculated to higher accuracy than the equal-time correlation due to the τ-integration. Because the spatial CLs are identical in both cases except for the trivial correlations caused by particle-hole excitations which have vanishing matrixelements in the static case, it is sufficient to concentrate on the static correlations.

To understand why particle-hole excitations do not contribute to the static correlation functions, we have to regard again the CFT result in Eq. (5.10). It is obvious that the long distance asymptotics is independent of imaginary time τ if $\Delta_c^+ = \Delta_c^-$ and $\Delta_s^+ = \Delta_s^-$. This is the case for the $2k_F$-parts of the s-s and d-d correlation. However, for a particle-hole excitation $\Delta_c^+ - \Delta_c^-$ or $\Delta_s^+ - \Delta_s^-$ is a non-zero integer and therefore

$$\int_0^\beta d\tau \; e^{2\pi T \mathrm{i}(\Delta_{c,s}^+ - \Delta_{c,s}^-)\tau} = \frac{e^{2\pi \mathrm{i}(\Delta_{c,s}^+ - \Delta_{c,s}^-)} - 1}{2\pi T \mathrm{i}(\Delta_{c,s}^+ - \Delta_{c,s}^-)} = 0 \; . \tag{5.16}$$

We would like to mention again that the TMRG results are reliable even at short distances r as shown for the free fermion case in chapter 4 giving additional information not covered by the correlation length alone.

In Fig. 5.9 (Fig. 5.10) the static longitudinal s-s correlation function for $J/t = 2.0$, $\mu = -1.4$ and $T = 2.0$ ($T = 0.1$) is shown. From Fig. 5.6 we expect π-oscillations of the correlation function for $T = 2.0$ and $2k_F$-oscillations for $T = 0.1$ because the non-oscillating part does not show up in a static correlation function as explained before. By

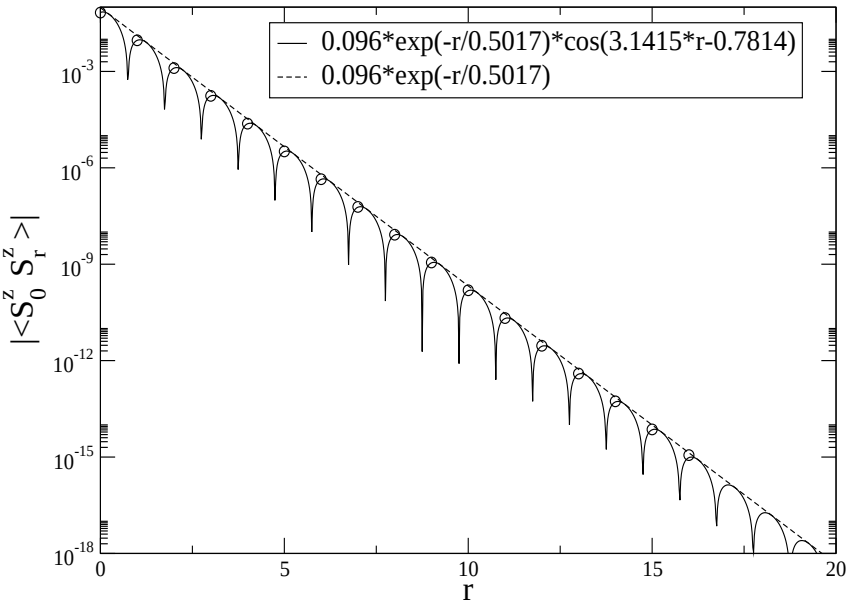

Figure 5.9: Static longitudinal s-s correlation function at $T = 2.0$ showing π-oscillations. The dotted line denotes an envelope corresponding to the exponential decay. The solid line is a guide to the eye.

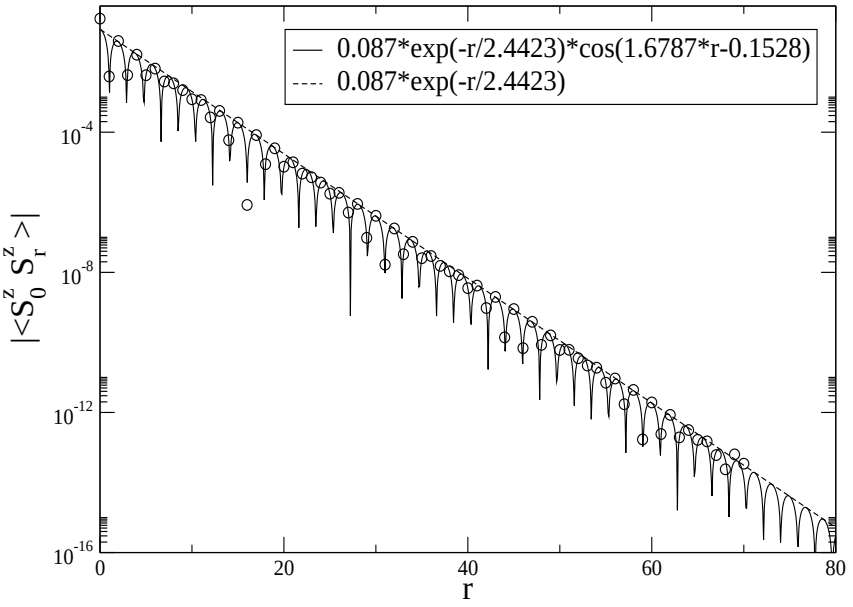

Figure 5.10: Static longitudinal s-s correlation function at $T = 0.1$ showing incommensurate oscillations. The dotted line denotes an envelope corresponding to the exponential decay. The solid line is a guide to the eye.

using $\langle S_0^z S_r^z \rangle = A \exp(-r/\xi) \cos(kr + \delta)$ as a fit function we have estimated the CLs as well as the wavevectors for both temperatures directly from the correlation functions (see

legends in Fig. 5.9 and Fig. 5.10). In both cases the results coincide within errors of the order 10^{-4} with that obtained by using directly the eigenvalues of the QTM. The perfect coincidence of the CLs estimated directly from the eigenvalues and that from a fit of the correlation function is not astonishing. In both cases the same QTM is used in the numerics where several eigenvalues are calculated directly using diagonalization routines in the first case whereas only the largest eigenvalue and the corresponding eigenvectors are needed to calculate the correlation function by some time-consuming matrix-vector multiplications in the second case. However, it provides a good consistency check of the numerics.

5.2 The physically relevant region

As mentioned in the introduction the t-J model is a simplification of the Hubbard model obtained in the limit $U \gg t$. Thus, one is especially interested in the case where the spin exchange coupling $J = 2t^2/|U|$ is smaller than the hopping t. The TMRG is applicable for any value of J/t with almost the same accuracy and our algorithm remains stable even in the limiting cases $J/t \ll 1$ or $J/t \gg 1$. Problems as reported by Ammon *et al.* [32] never occurred in our algorithm. To be specific, we never observed that the algorithm breaks down after performing only a few or more RG steps although we have retained up to 240 states to calculate the correlation lengths accurately. In the following calculations we set $J/t = 0.35$, a value often used in the literature.

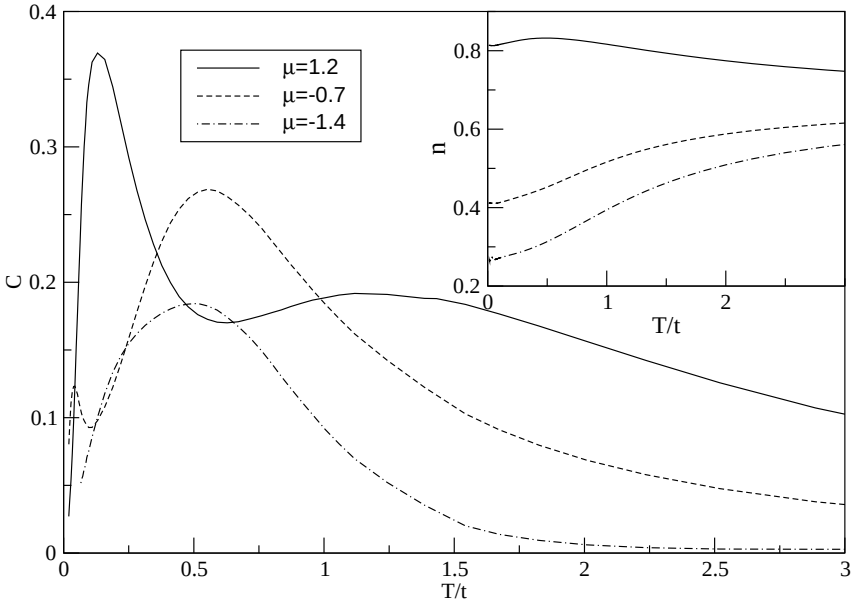

Figure 5.11: Specific heat for $J/t = 0.35$ and three different chemical potentials corresponding in the low temperature limit to a high ($\mu = 1.2$), medium ($\mu = -0.7$) and low ($\mu = -1.4$) electron density. Note again the two-peak structure due to spin-charge separation. The inset shows the temperature dependence of the densities $n(\mu, T)$ for the same chemical potentials.

When we regard the specific heat shown in Fig. 5.11, a two-peak structure is again obvious in the high and medium density case and there seems to be a linear regime consistent with TLL theory although we have noticed in the supersymmetric case that numerical errors grow up for low temperatures. The structure of the spin and charge susceptibilities (see Fig. 5.12) also looks rather similar to the supersymmetric case. The arguments

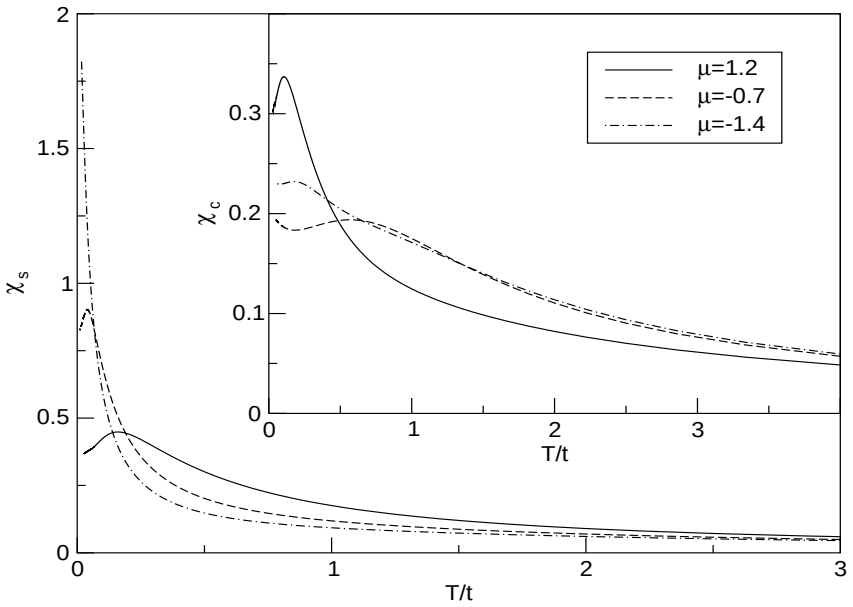

Figure 5.12: Susceptibilities and compressibilities for the three different chemical potentials and $J/t = 0.35$.

given for the high and low temperature regime of the susceptibilities are also applicable here. It is easy to understand that the absolute values of the spin susceptibility are now larger because the weaker antiferromagnetic coupling J less efficiently suppresses a ferromagnetic alignment of spins. In principle, the qualitative discussion of c, χ_s and χ_c is very similar to that of the integrable case. There are, however, two modifications. First, in the charge susceptibility for low densities we observe two maxima. We do not have any simple explanation of this fact. Note that a similar observation has been made for the Hubbard chain. Second, due to the different energy scales of spinon and incoherent single particle motion at any density there are two maxima in $c(T)$ even at densities close to 1.

We also calculated again several s-s and d-d CLs as shown in Fig. 5.13. The CLs are now often difficult to distinguish and the crossing of CLs is "smoother" and shifted to higher temperatures when compared with the supersymmetric case. This clearly shows that the spin-exchange interaction is responsible for the various crossovers of CLs and in appendix B we show that all crossovers vanish for free spinless fermions. It is also striking that incommensurate oscillations are now present even at high temperatures. The leading s-s CL shows oscillations which are identified by Eq. (5.6d) as $2k_F$ whereas one of the d-d CL shows $4k_F$ oscillations. The other d-d CL from Fig. (5.13) is non-oscillating and leading in the low-temperature limit. These kinds of oscillations are expected from TLL theory

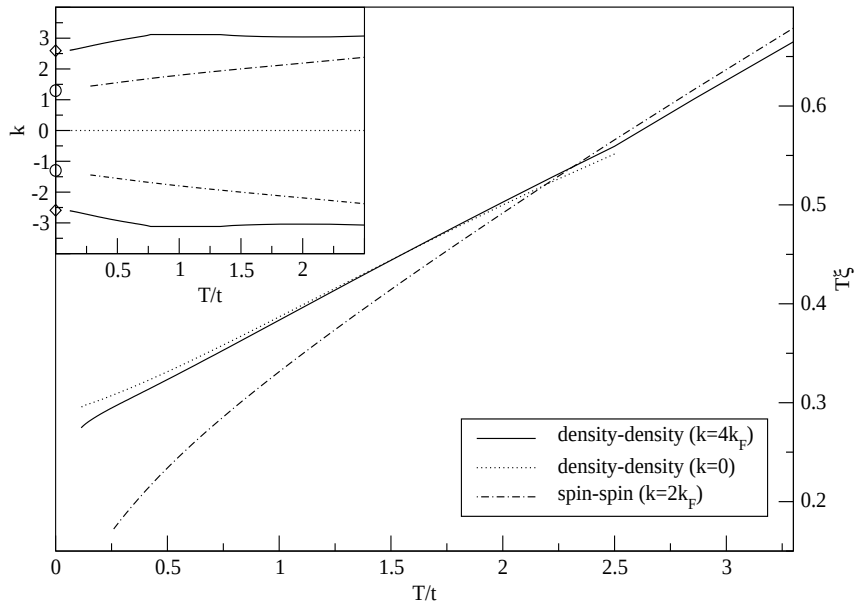

Figure 5.13: S-s and d-d CLs for $J/t = 0.35$ and $\mu = -0.7$. The inset shows the corresponding wavevectors. The circles (diamonds) denote the CFT result for $\pm 2k_F$ ($\pm 4k_F$).

(see Eq. (5.7a)) and we also note that the CLs seem to diverge again as $\xi \sim 1/T$ for low temperatures. This provides additional evidence that the t-J model at $J/t = 0.35$ belongs to the same universality class (TLL) as the supersymmetric model.

5.3 Phase separation

At J/t large, the attractive Heisenberg interaction in Eq. (5.1) dominates the kinetic energy term. In a canonical ensemble the model therefore phase separates into a high density and a low density region in order to optimize the Heisenberg energy. In our grand-canonical description of the model, however, there remains a competition between the chemical potential term and the Heisenberg exchange energy. If we ignore the kinetic energy completely - what is exact if total phase separation occurs - a simple picture evolves. Because the ground state energy of a spin-1/2 Heisenberg chain per particle is given by $-J \ln 2$, we expect in the limit $T \to 0$ an empty state if $\mu < -J \ln 2$ and a state with $n = 1$ if $\mu > -J \ln 2$. Therefore phase separation can only be present at one special point characterized by $\mu \approx -J \ln 2$. In the Figures 5.14(a), 5.14(b), 5.14(c) the density at a constant temperature is shown as a function of the chemical potential for three different parameters J/t. Fig. 5.14(a) shows that at $J/t = 3.1$ the compressibility $\partial n/\partial \mu$ in the limit $T \to 0$ is not diverging, indicating that the phase separated region is not reached yet. At $J/t = 3.3$ (Fig. 5.14(b)) the density jumps from $n = 0$ to $n \approx 0.8$ at $\mu \approx -J \ln 2$ in the limit $T \to 0$ as expected for the phase separated region. The phase separation is here between the empty and an electron rich state. At $J/t = 3.5$ we find full phase

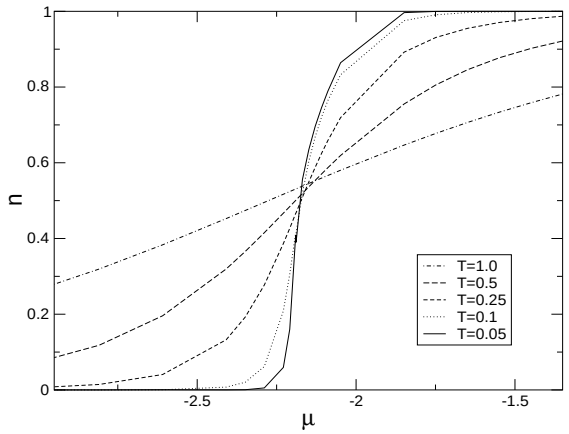

(a) $J/t = 3.1$

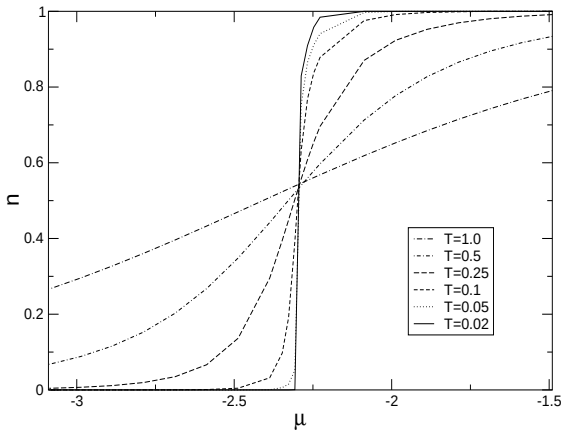

(b) $J/t = 3.3$

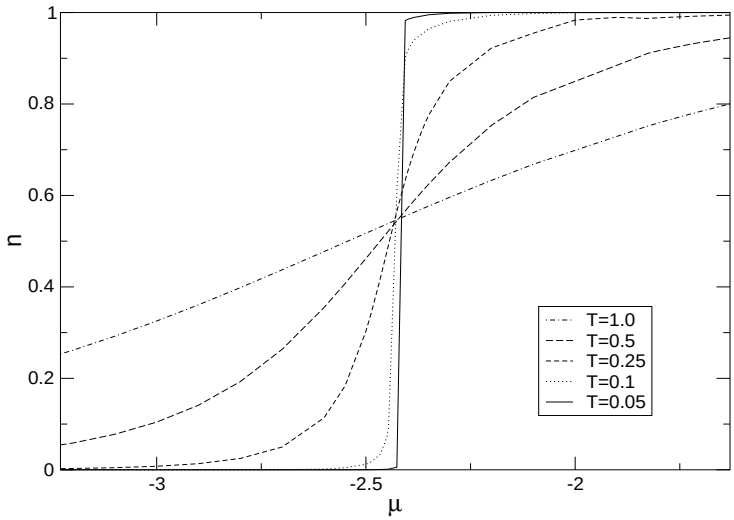

(c) $J/t = 3.5$

Figure 5.14: The figures show the density as a function of the chemical potential for fixed temperatures T in units of t. Note that the lines connect a finite number of data points.

separation, indicated by the jump of the density from 0 to 1 for $T \to 0$ (see Fig. 5.14(c)). Our calculations confirm that the fully phase-separated state is destroyed by introducing holes into the Heisenberg chain island as stated by Ogata *et al.* [34].

5.4 Luther-Emery phase

As already mentioned in the introduction (see Fig. 5.1) a phase with a spin gap is expected at least for low densities and values of J/t close to phase separation. Because we expect the spin gap to be caused by a marginal operator leading to an exponentially small gap, the TMRG is not suited to determine the phase boundaries. However, in regions where the spin gap is larger than the lowest accessible temperature, the TMRG can show the existence of such a phase without using any additional assumptions. A spin gap is directly visible in the spin susceptibility going to 0 for $T \to 0$. Therefore, we have calculated

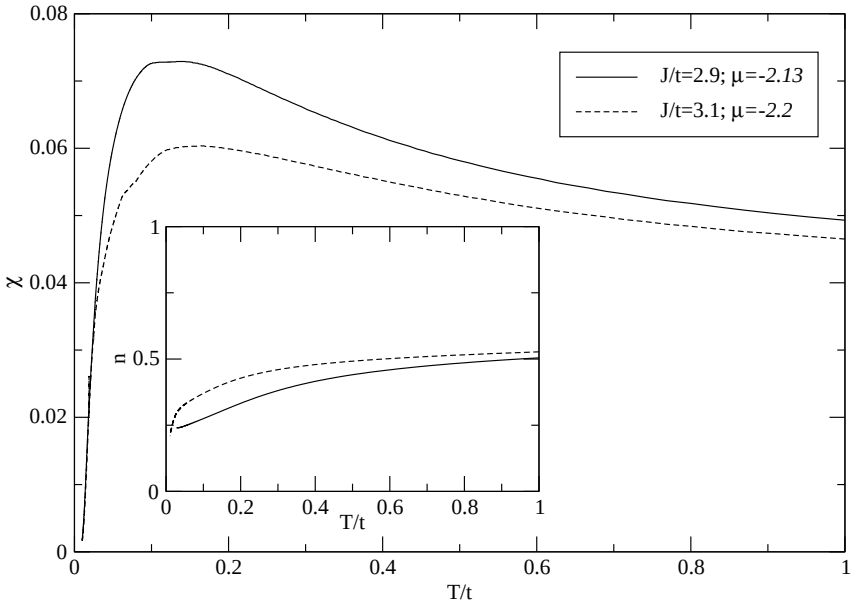

Figure 5.15: Spin susceptibilities for two different parameter sets $(J/t, \mu)$, both showing a spin gap of the order $\Delta \sim 0.05$. The inset shows the temperature dependence of the corresponding densities.

the spin susceptibility for two different values of J/t close to phase separation and have chosen chemical potentials so that the density is given by $n \approx 0.2$ for low temperatures (see Fig. 5.15). In both cases a very small spin gap appears. The quadratic dispersion of a gapped 1D system leads to $\chi \sim \exp(-\Delta/T)/\sqrt{T}$ for the low-temperature asymptotics. Using this function for a fit of the numerical data, we find $\Delta = 0.05 \pm 0.01$ in both cases.

Another proof of LE-properties of the t-J model is given by the calculation of s-s and d-d CLs. In Fig. 5.16 these CLs are shown as usual as temperature times CL versus temperature. A spin gap is connected with finite s-s CLs ξ_s and we therefore expect that $T \cdot \xi_s \to 0$ for $T \to 0$. On the other hand the d-d CLs ξ_n are not affected and should still diverge as $\xi_n \sim 1/T$ for low temperatures. This picture seems to be consistent with the numerical results. However, we are not able to present numerical data for lower temperatures, which could support this scenario further.

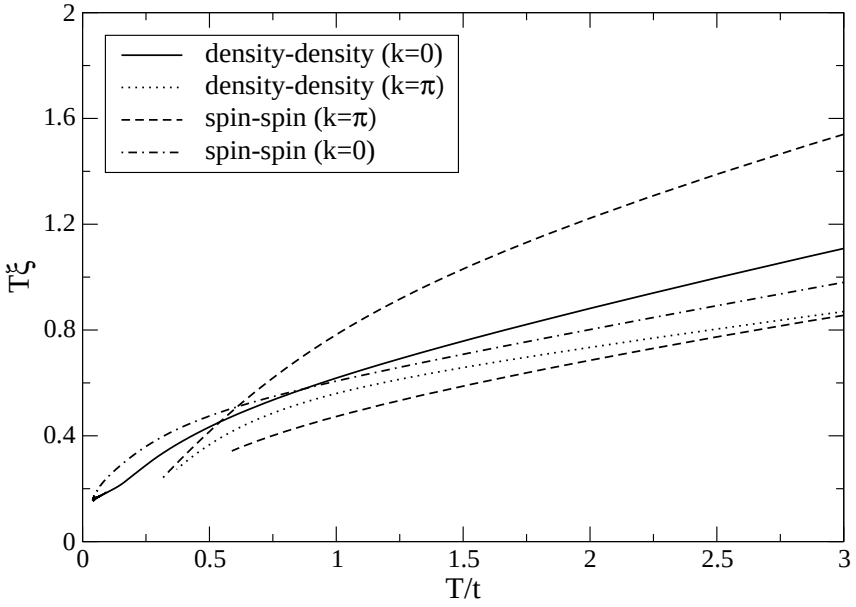

Figure 5.16: Correlation lengths at $J/t = 2.9$ and $\mu = -2.13$. Note that the oscillations of all shown correlation lengths are commensurate over the entire temperature range.

5.5 t-J model with Ising anisotropy

In this section we want to consider the t-J model with modification of Hamiltonian (5.1) by replacing

$$\boldsymbol{S}_i\boldsymbol{S}_{i+1} \to S_i^x S_{i+1}^x + S_i^y S_{i+1}^y + \Delta S_i^z S_{i+1}^z - \frac{\Delta}{4} n_i n_{i+1} \tag{5.17}$$

where $\Delta > 1$. We expect that such an anisotropy enhances superconducting correlations relative to d-d correlations as has been explicitly shown in an exactly solvable anisotropic t-J model by Bariev *et al.* [47]. However, their version includes some unphysical parity breaking terms (keeping PT-symmetry) making it interesting to investigate if the same is true for the model defined here. For the Heisenberg chain it is known that an Ising-like anisotropy promotes long range spin order and causes a spin gap. The situation is more complicated in the t-J model: The charge sector is unaffected and the charge excitations remain critical (i.e. d-d correlations decay algebraically in the ground state). The expected long range spin order could be hidden when the density $n \neq 1$, because the spin operators act on the physical lattice whereas the spins are coupled to the "electron lattice". The long range order would then be visible only in a string order parameter $\langle \tilde{S}_0^z \tilde{S}_r^z \rangle$ where all empty sites between 0 and r are omitted. This has been emphasized also by Pruschke and Shiba [48], who have studied the limit $J/t \to 0$. In any case there has to be a spin gap also in the t-J model if $\Delta > 1$. However, in the Heisenberg chain the gap is given by $\Delta E \propto \exp\{-J/(\Delta - 1)\}$ leading to an exponential small gap and this gap is further reduced in the t-J model for densities $n < 1$ making it often undetectable in the thermodynamical data. In Fig. 5.17 a spin gap $\Delta_s = 0.054 \pm 0.01$ is visible in the susceptibility data for $\mu = -1.5$ corresponding to $n \approx 0.98$ in the low-temperature

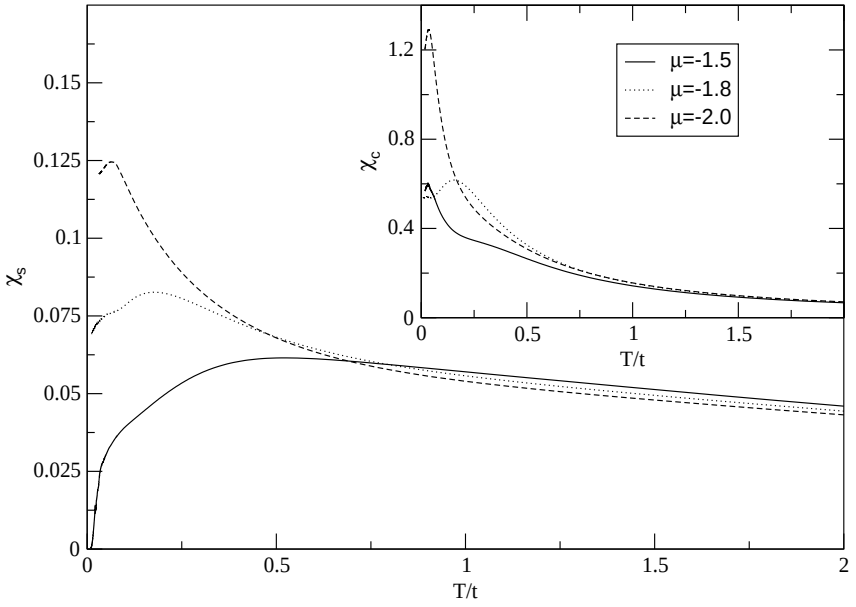

Figure 5.17: Susceptibilities (main figure) and compressibilities (inset) for three different chemical potentials where $J/t = 2.0$ and the anisotropy parameter is given by $\Delta = 1.5$.

limit. This is in agreement with the gap $\Delta^{HB} = 0.043$ for the Heisenberg chain with the same anisotropy. For $\mu = -1.8$ ($n_{T\to 0} \approx 0.54$) and $\mu = -2.0$ ($n_{T\to 0} \approx 0.27$) the spin gap is so small that it is not visible in the accessible temperature range. The specific heat

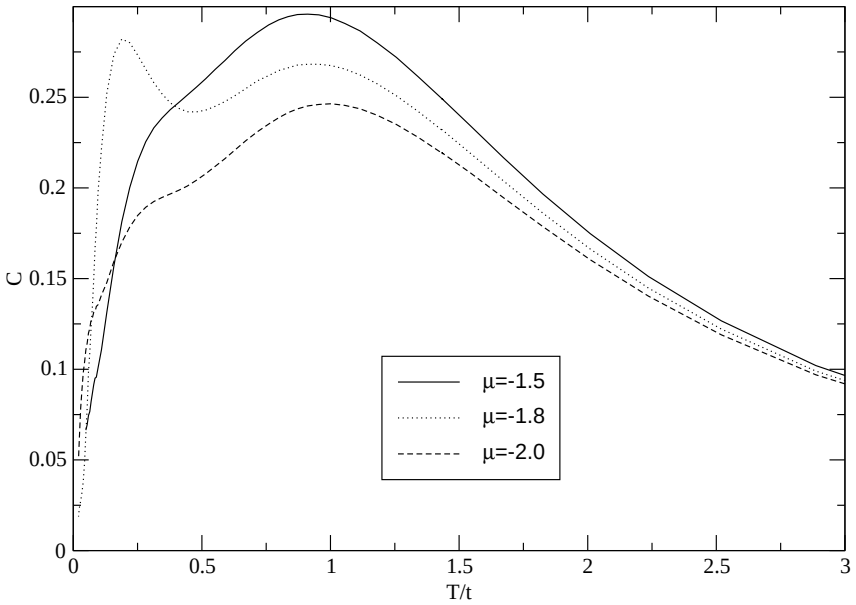

Figure 5.18: Specific heats for the same chemical potentials and same parameters as in Fig. 5.17.

(Fig. 5.18) looks qualitatively similar to the isotropic case. Again two peaks (shoulders) are visible, corresponding to spinon and holon excitations. In Fig. 5.19 several crossovers

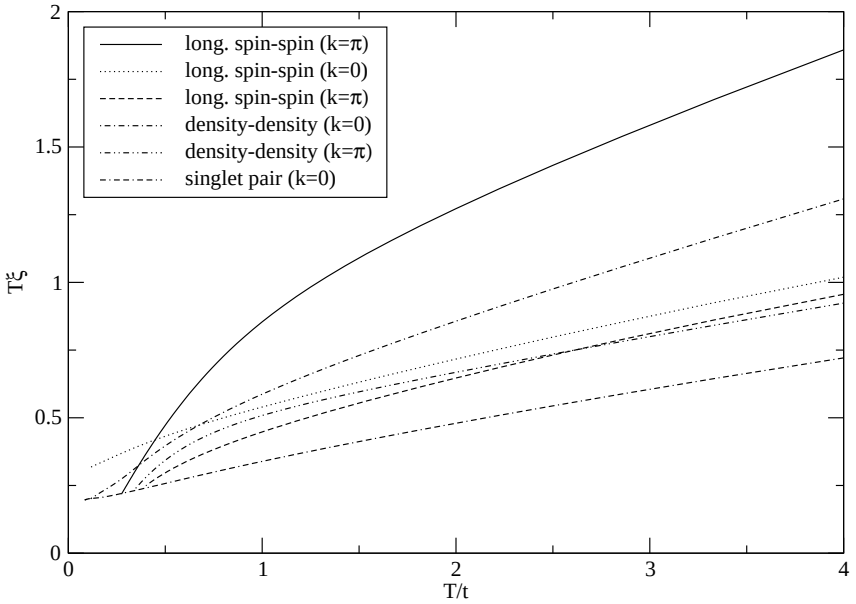

Figure 5.19: Leading d-d and longitudinal s-s CLs for $\mu = -1.8$ and $\Delta = 1.5$. Additionally, the leading singlet pair CL is plotted. The shown CLs have commensurate oscillations.

in the CLs are visible. In the low-temperature regime the leading d-d and longitudinal s-s CLs diverge as $\xi \sim 1/T$ showing that the charge excitations remain critical and that the long-range spin order is hidden. As expected the singlet pair CL dominates at low temperatures over the d-d CL supporting that an Ising-like anisotropy could be a mechanism leading to superconductivity in higher dimensions [47].

5.6 Summary and discussion

At the supersymmetric point of the one-dimensional t-J model we have compared the numerical results for the density, free energy, specific heat, susceptibility and compressibility with Bethe ansatz and have found an excellent agreement. In particular, we have concentrated on the calculation of correlation lengths at the supersymmetric point to study the crossover from the non-universal high-T lattice into the quantum critical regime ($T \ll t$). The non-universal regime is characterized by various crossovers between CLs with different wavevectors whereas the CLs are non-crossing and diverging as $1/T$ in the universal TLL regime. A good coincidence between predictions for the low-temperature asymptotics of CLs by CFT and the numerical results was shown, but it was important to take also the logarithmic corrections into account. Especially, we like to mention that a suggestive picture of the quantum critical regime extending far along the temperature axis, as is often drawn by people who study quantum critical points, is not appropriate. CFT or TLL results can be extended to finite temperatures. However, they are restricted to the very low T regime. This has also been pointed out by Anderson in an amusing comment [49]. For

$J/t = 0.35$, a value often considered physically relevant, we observed properties that were rather similar to the supersymmetric case. In particular, the t-J model at this parameter point also belongs to the TLL universality class. In our grand-canonical description phase separation has the meaning of phase coexistence at one chemical potential μ. This is due to the remaining competition between the Heisenberg and the chemical potential term. If J/t is large enough so that total phase separation occurs, this competition leads to an empty state for $T = 0$ if $\mu < -J \ln 2$ and to a state with $n = 1$ if $\mu > -J \ln 2$. Our data also show that the fully phase separated state is destroyed by introducing holes into the Heisenberg island. By directly calculating the spin susceptibility for small densities and values of J/t near phase separation, we have proved the existence of a spin-gap phase without making additional assumptions. This was also supported by the calculation of s-s and d-d CLs, indicating that all spin CLs are finite at zero temperature, whereas the d-d CLs are unaffected and diverging still as $1/T$. Finally we have studied the t-J model with an additional Ising-like anisotropy and have shown that singlet pair correlations are enhanced so that a tendency towards superconductivity is expected in higher dimensions. Furthermore, we have settled that the expected long range spin order is hidden away from half-filling, because the spins are coupled to the "electron lattice" whereas the operators act on the physical lattice.

Chapter 6

Quantum Spin-Orbital Physics in Transition Metal Oxides

Contrary to a usual band insulator the internal degrees of freedom remain still active in a *Mott insulator*. In most of these insulators the distribution of electrons around every atom is frozen in at the melting point and changes little down to zero temperature so that the spin is the only active internal degree of freedom. This leads to the widely studied spin models as for example the Heisenberg model or the t-J model when hole-doping away from the insulating case is studied. Recently, however, much attention has focused on transition metal oxides which have additionally low-lying electronic states (termed "orbitals") [50, 21] so that temperature or doping can drive marked redistributions of the valence electron density ("orbital orderings"). Examples for compounds showing such phenomena are $LaMnO_3$ [51], $LaTiO_3$ [52, 53] or YVO_3 [22, 54, 55, 56, 57, 58].

The transition-metal ions in these compounds have occupied d-orbital levels and the crystal has perovskite structure. This means that each transition metal ion is surrounded by six oxygen ions (O^{2-}) forming an octahedron and giving rise to a nearly cubic crystal field potential which splits the d-orbital levels. For a single electron state with orbital momentum l the $(2l+1)$ spherical harmonics Y_l^m, which are degenerate in isotropic space, form a basis for the irreducible representation of the three-dimensional rotation group $O(3)$, which is called $\Gamma^{(l)}$ or D_l [59]. The crystal field reduces this symmetry to some finite group of rotations which in our case is approximately the octahedral group O. The originally irreducible representation of the full rotation group can now be reduced with respect to this subgroup, thus partly lifting the degeneracy. Since the spherical harmonics of order l form a basis set for the group of all rotations, they can still be used as basis for a finite group of rotations. The representation D_2, which we are regarding here, must split because there exists no five-dimensional irreducible representation of the octahedral group O. Using the character table of O it follows $D_2 = E \oplus T_2$, where E is a two-dimensional irreducible representation of O and T_2 a three-dimensional one.[1] A suitable basis is received by a unitary transformation of the basis set Y_2^m [59, 60]

$$\left.\begin{array}{rcl} \frac{-\mathrm{i}}{\sqrt{2}}\left(Y_2^2 - Y_2^{-2}\right) & \sim & d_{xy} \\ \frac{-1}{\sqrt{2}}\left(Y_2^1 - Y_2^{-1}\right) & \sim & d_{xz} \\ \frac{\mathrm{i}}{\sqrt{2}}\left(Y_2^1 + Y_2^{-1}\right) & \sim & d_{yz} \end{array}\right\} t_{2g} \qquad \left.\begin{array}{rcl} Y_2^0 & \sim & d_{3z^2-r^2} \\ \frac{1}{\sqrt{2}}\left(Y_2^2 + Y_2^{-2}\right) & \sim & d_{x^2-y^2} \end{array}\right\} e_g \ , \tag{6.1}$$

[1] Including inversion symmetry, i.e. regarding the full octahedral group O_h we get $D_{2g} = E_g \oplus T_{2g}$. The Y_l^m are basis functions of D_{lg} if l is even and of D_{lu} if l is odd and g terms split only into g terms and u terms split only into u terms.

with the t_{2g} triplet being lower in energy.[2] The e_g orbitals of $d_{x^2-y^2}$ and $d_{3z^2-r^2}$ symmetry are bond oriented whereas the t_{2g} level consists of orbitals having d_{xy}, d_{yz}, d_{zx} symmetry and are therefore not bond oriented. Ti^{3+} is in $3d^1$, V^{3+} in $3d^2$ and Mn^{3+} in $3d^4$ configuration and the spins of these electrons are always aligned parallel according to Hund's rule.[3] Therefore one spin is put to the t_{2g} orbitals ($s = 1/2$ system) for $LaTiO_3$, two spins are put to the t_{2g} orbitals ($s = 1$ system) for YVO_3 and three spins to the t_{2g} orbitals and one to the e_g orbitals ($s = 2$ system) for $LaMnO_3$. An additional small tetragonal distortion of the octahedron splits the triplet further into a doublet and a singlet [60]. Such a distortion, although rather weak, is observed in YVO_3 at $T \sim 200\,\mathrm{K}$ [61] and one out of the three orbitals is therefore singled out. The resulting electron configuration for the V^{3+} ion in YVO_3, the compound we are especially interested in, is shown in Fig. 6.1. The level

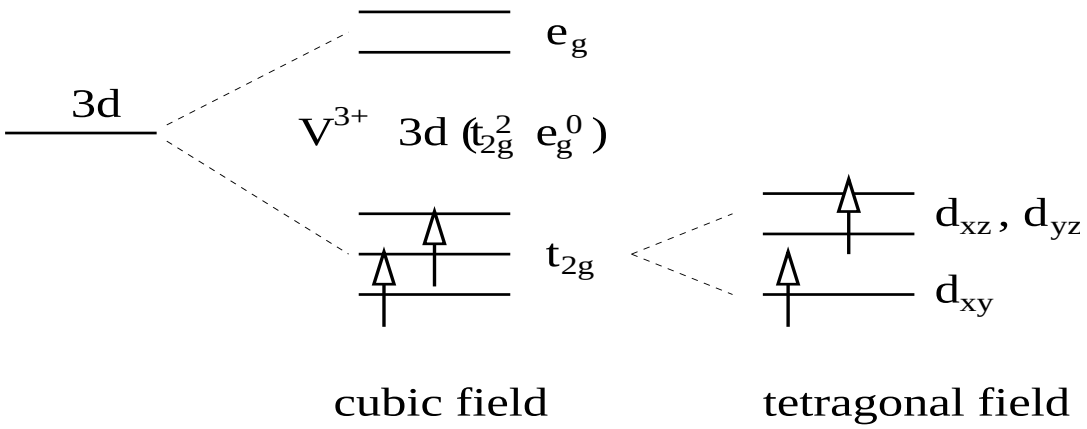

Figure 6.1: Crystal field splitting of the d-level and ground-state electron configuration of the V^{3+} ion.

structure of the split t_{2g} triplet is still controversial and there exist two different points of view. Assuming that the elongation of the octahedra is governed by the Jahn-Teller (JT) effect and arranging the orbital levels accordingly, it is concluded that the singlet is higher in energy than the remaining doublet [61]. However, this kind of elongation of octahedra is observed in many different compounds regardless of the orbital symmetry. Even in oxides without orbital degeneracy such distortions have been observed, suggesting that the JT effect is not the sole origin. Regarding on the other hand the superexchange interaction[4] it turns out that this is best optimized by strong orbital quantum fluctuations if the singlet is lower in energy. In $YTiO_3$ [62, 63] and in YVO_3 [57, 58] the second scenario seems to be in accordance with most of the experimental results and also with considerations based on electronic structure calculations [64, 65] so that we will assume a level structure as shown in Fig. 6.1.

Due to the remaining orbital degeneracy, spin and orbital degrees of freedom have to

[2]For pure d-electron states the nomenclature $d\epsilon$ for the triplet and $d\gamma$ for the doublet is often used.

[3]We assume here that the spin coupling energy is larger than the crystal field energy, i.e. for d^4, d^5, d^6 and d^7 configurations, the high spin state is lower in energy than the low spin state.

[4]This will be discussed in detail in the next section.

be considered on equal footing leading to effective *spin-orbital models*. In such systems a large number of nearly degenerate many-body states is accessible due to these unquenched orbital degrees of freedom ("orbital frustration"). Furthermore, the sign and magnitude of the spin-spin interactions is determined by the orbital occupation resulting in a strong spin-orbital coupling. This leads to unusual magnetic properties as for example *colossal magnetoresistance* [51] or *magnetization reversals* with temperature [54, 55] and makes a microscopic description extremely difficult. For $LaMnO_3$ the two possible choices of the e_g electron can be represented by an *orbital pseudospin* $\boldsymbol{\tau}$ where e.g. $\tau^z = 1/2$ means an occupied $d_{x^2-y^2}$ orbital and $\tau^z = -1/2$ an occupied $d_{3z^2-r^2}$ orbital. The same is also possible for the t_{2g} systems because only two out of the three orbitals are active along a given crystal axis. The transfer integral between two neighbouring transition metal ions is determined by the overlap between their d orbitals and the p orbitals of the oxygen ion between them. Along the c-axis, for example, an electron can hop only between the d_{yz} or d_{xz} orbitals of neighbouring ions through the π-bonding with the oxygen $2p_y$ or the $2p_x$ state, respectively. The d_{xy} is inactive along this direction.

Quite generally, a Hamiltonian for these systems is therefore given by

$$H = \sum_{i,j} \{J_{ij}(\boldsymbol{\tau}_i, \boldsymbol{\tau}_j)\boldsymbol{S}_i\boldsymbol{S}_j + C_{ij}(\boldsymbol{\tau}_i, \boldsymbol{\tau}_j)\} \tag{6.2}$$

with interactions J_{ij} and C_{ij}, which are determined by exchange processes with intermediate virtual states. The simplest of such models is obtained if one regards the usual permutation of nearest neighbour spin states where an additional orbital quantum number is present. Restricted to one dimension, one finds in this case $J_{i,i+1} = \boldsymbol{\tau}_i\boldsymbol{\tau}_{i+1} + 1/4$ and $C_{i,i+1} = 1/4(\boldsymbol{\tau}_i\boldsymbol{\tau}_{i+1} + 1/4)$ leading to

$$H = \sum_i \left(\boldsymbol{S}_i\boldsymbol{S}_{i+1} + \frac{1}{4}\right)\left(\boldsymbol{\tau}_i, \boldsymbol{\tau}_{i+1} + \frac{1}{4}\right) \ . \tag{6.3}$$

This model obviously has a SU(2)×SU(2) symmetry, i.e. SU(2) symmetry in both spin and pseudospin space, but it also obviously has an additional Z_2 symmetry interchanging spin and orbital degrees of freedom. Less obviously the full symmetry of (6.3) is actually the higher symmetry group SU(4), which unifies the spin and orbital degrees of freedom [66, 24]. The one-dimensional version is equivalent to the integrable $q = 4$ Uimin-Sutherland model, which has been solved by Bethe ansatz [67]. The exact ground state and the excitation spectrum consisting of three gapless mixed spin-orbital modes has been obtained. Critical properties are expected here because this model belongs to a class of gapless $SU(N)$ symmetric models which have been investigated by Affleck [23] using CFT. The idea of mixed spin-orbital excitations was also crucial to understand anomalous magnetic properties of $LaTiO_3$ [53], a system showing a coherent orbital-liquid ground state [52]. Thermodynamic properties of the SU(4) symmetric model in 1D have been investigated by the quantum Monte Carlo method [68]. We will return to this model in section 6.2.

In reality, however, the SU(2) symmetry in pseudospin space is always broken due to the Hund's rule splitting of the excited virtual states multiplet. Another aspect has also

been ignored so far: the Jahn-Teller (JT) coupling of the orbitals to the lattice. This is especially dramatic for e_g systems due to the bond orientation of the orbitals. When two neighbouring oxygen ions along an axis move towards the transition metal ion the energy of the respective orbital gets higher and the degeneracy is lifted. A strong JT effect therefore leads to orbital ordering, supporting particular magnetic structures. This is in accordance with the standard Goodenough-Kanamori theory [69, 70] of a successive ordering of orbitals and spins. In this theory orbitals are treated on a mean-field level and that orbital order is frozen, which optimizes the JT and the superexchange energy. Much more challenging from a theoretical point of view are t_{2g} systems because these orbitals are not bond oriented and the JT coupling is therefore relatively weak. In such systems the standard theory fails because orbital fluctuations are strong and a picture of a static orbital ordering is not appropriate. The orbital and spin degrees of freedom remain intimately connected and the classical mean field treatment has to be replaced by a quantum mechanical treatment of spins **and** orbitals.

6.1 A spin-orbital model with $S = 1$: The case of YVO_3

Neutron spectroscopy has shown that the Mott-Hubbard insulator YVO_3 exhibits two magnetic phases [71, 58]. Below $T_{N1} = 75$K the magnetic structure is of G-type (antiferromagnetic in all three directions) whereas a C-type magnetic order (ferromagnetic chains along the c-axis with antiferromagnetic coupling between the chains) is found for $T_{N1} < T < T_{N2} = 116$K. The high temperature phase is especially puzzling: G-type reflections persist indicating a non-collinearity of the magnetic structure with a relatively large canting angle $\sim 16.5^\circ$ away from the ab-plane. The total ordered moment is strongly reduced compared to the free ion moment as well as to the ordered moment of the low temperature phase. This reduction suggests strong quantum fluctuations in the C-type phase. The unusual nature of the high temperature phase is underscored by its magnetic dynamics obtained by inelastic neutron scattering [58]. Whereas the magnon dispersion in the low temperature phase is well fitted by an anisotropic Heisenberg model up to the first order phase transition at T_{N1}, the magnon spectrum in the high temperature phase is unexpectedly split along the ferromagnetic c-axis. A fit by a Heisenberg model is only possible by assuming two different exchange bonds along the c-axis, i.e. a dimerization. However, crystallographically the $V - V$ distances along the c-axis are indistinguishable, which points to orbital correlation effects responsible for the alternation of spin exchange bonds.

Another unusual magnetic property observed in YVO_3 single crystals are temperature-induced magnetization reversals [54, 55]. Upon cooling in a modest magnetic field the magnetization increases rapidly below T_{N2} parallel to the applied field, reaches a maximum and then starts to decrease monotonously. At $T^* \approx 95$K it crosses zero and becomes negative, i.e. antiparallel to the applied field. At $T \approx T_{N1}$ the magnetization suddenly jumps again to a positive value. In an explanation a competition between the single ion magnetic anisotropy and the antisymmetric spin-spin (Dzyaloshinski-Moriya) interaction has been proposed [54, 55].

Here we want to explain the stability of the high temperature phase, the optical-acoustic splitting of the magnon spectrum, the small magnitude and large canting of the ordered moment semiquantitatively based on a microscopic model. A significance of t_{2g} orbital degrees of freedom for understanding the peculiar magnetic behaviour has been emphasized [54, 56, 61, 22]. According to arguments based on electronic structure calculations [72, 64, 65, 73] the t_{2g} triplet is split into a lower-lying singlet of d_{xy} symmetry and a higher-lying doublet of d_{xz} and d_{yz} symmetry. This splitting is established at $T \sim 200$ K, where a structural transition takes place and a c-axis bond becomes shorter than the average of in-plane bonds [61]. Therefore the d_{xy} orbital is always half-occupied and dominates the antiferromagnetic ab-plane interactions. The two degenerated t_{2g} orbitals are active along the c-direction as explained in the previous section. Hence, the interesting spin-orbital physics is restricted to one dimension although the compound has spin-exchange couplings of the same magnitude in all three directions. Calculating

thermodynamic properties for a realistic 1D model and taking into account the coupling between the chains mediated by the d_{xy} orbitals on a mean-field level we could therefore expect to understand much of the physics underlying the magnetic behaviour of YVO_3.

6.1.1 The one-dimensional model

The relevant spin-orbital model to describe magnetism of vanadium oxides has to involve $S = 1$ spins because Hund's coupling J_H is large [74]. For the cubic vanadates $LaVO_3$ and YVO_3 a realistic superexchange model has been derived in Ref. [22], where two out of the three t_{2g} orbitals are active along a given cubic axis, described again by a $\tau = 1/2$ orbital pseudospin. In the simple classical limit $S \gg 1$ and neglecting the splitting of the excited virtual states multiplet by Hund's coupling J_H, Shen *et al.* [75] have shown that the ground state in 1D is an orbital valence bond (OVB) solid formed by orbital singlets and parallel spins, where neighbouring OVBs are noninteracting.

Here we treat a realistic quantum spin-orbital model with $S = 1$ and a twofold orbital degeneracy in 1D, where the effects due to Hund's coupling are included. Thermodynamics of two distinct phases, a 4-site periodic quantum dimer phase, and a ferromagnetic state that occurs at larger J_H, is studied numerically. A critical value of J_H separating the two phases is obtained. The most important observation is that strong dimer correlations develop *at finite temperature on the ferromagnetic side* of the transition, which are driven by large entropy of low-lying dimer states of the model. In section 6.1.3 the relevance of these findings to the intermediate phase of YVO_3 is discussed.

The Hamiltonian of the model is given by

$$H^{(c)} = J \sum_i \left[\frac{1}{2} \left(\boldsymbol{S}_i \cdot \boldsymbol{S}_{i+1} + 1 \right) \hat{J}_{i,i+1} + \hat{K}_{i,i+1} \right] , \tag{6.4}$$

where $\boldsymbol{S}$ being an $S = 1$ spin operator, and $J = 4t^2/U$ represents an overall superexchange energy scale. The operators $\hat{J}_{i,j}$ and $\hat{K}_{i,j}$ describe orbital exchange processes on the bond

$$\begin{aligned} \hat{J}_{i,j} &= (1 + 2R) \left(\boldsymbol{\tau}_i \cdot \boldsymbol{\tau}_j + \frac{1}{4} \right) - r \left(\tau_i^z \tau_j^z + \frac{1}{4} \right) - R \, , \\ \hat{K}_{i,j} &= R \left(\boldsymbol{\tau}_i \cdot \boldsymbol{\tau}_j + \frac{1}{4} \right) + r \left(\tau_i^z \tau_j^z + \frac{1}{4} \right) \, , \end{aligned} \tag{6.5}$$

with $\boldsymbol{\tau}$ acting in a $\tau = 1/2$ orbital pseudospin space. The coefficients $R = \eta/(1 - 3\eta)$ and $r = \eta/(1 + 2\eta)$ originate from the Hund's rule splitting of the excited t_{2g} multiplet by $\eta = J_H/U$. This is exactly the Hamiltonian derived for cubic vanadates in Ref. [22] restricted here to the c-axis. Physically, pseudospin $\boldsymbol{\tau}$ describes the 1D fluctuations of xz and yz orbitals along the c-axis, while the third orbital xy is frozen below the structural transition at ~ 200K as discussed before. Therefore orbital resonance is blocked in ab-planes and by using the same Hamiltonian (6.4) for the a and b axis where τ describes

the respective orbitals, we find

$$H^{(a,b)} = J \sum_i \left[(\boldsymbol{S}_i \boldsymbol{S}_{i+1} + 1) \left(\gamma + \delta \, n_i^{(xz,yz)} n_{i+1}^{(xz,yz)} \right) + \epsilon \, n_i^{(xz,yz)} n_{i+1}^{(xz,yz)} \right] \tag{6.6}$$

with

$$\gamma = \frac{1}{4}(1 - (r + R)) \quad , \quad \delta = \frac{1}{4}(1 + 2R - r) \quad , \quad \epsilon = \frac{1}{2}(r + R) \ . \tag{6.7}$$

Here n_i^{xz} (n_i^{yz}) is the orbital occupation number of the xz (yz) orbital, respectively. Because $J > 0$ and $\gamma + \delta \, n_i^{(xz,yz)} n_{i+1}^{(xz,yz)} > 0$ the spin exchange within ab-planes is antiferromagnetic. Classically we therefore expect $\langle \boldsymbol{S}_i \boldsymbol{S}_{i+1} \rangle + 1 = 0$. Thus, the coupling of the orbitals in ab-planes within this simple approximation is Ising-like and given by the third term in Eq. (6.6). It is proportional to η and therefore rather small for realistic values of J_H and U. *The orbital physics is essentially 1D.* On the other hand the spin-coupling constant J_{ab} is determined on a mean-field level by $J(\gamma + \delta \, \langle n_i^{(xz,yz)} n_{i+1}^{(xz,yz)} \rangle)$ and of the same order as the coupling constant J_c along the c-chains. *The spin-sector has three-dimensional nature.* However, we will first discuss the pure one-dimensional model described by Eqs. (6.4) and (6.5) and will return to the three-dimensional case in section 6.1.3.

To study the thermodynamic properties of the one-dimensional version we again apply the two TMRG algorithms introduced in chapter 2. The spin and orbital degrees of freedom are combined leading to a six-dimensional local Hilbert space. Compared to the t-J model discussed in the previous chapter, where the local basis set only contains 3 states, the numerical effort is therefore drastically increased. It is the novel algorithm which makes calculations for this model on a workstation with a sufficient number of RG-states possible due to the reduction in memory by a factor S^2 needed to store the system and the enlarged system block compared to the traditional one. However, even the novel algorithm needs ~ 2 GB computer memory and more than 2 weeks computational time on an Alpha DS20E workstation if 120 states are retained. A system with 6 local basis states is therefore a kind of boundary for serial TMRG computations today. For systems containing more local states a parallelization of the algorithm is required and can be effectively implemented due to the block structure caused by conservation laws. Here we have renounced to parallelize the algorithm, but we have implemented the conservation laws for spin and orbital quantum numbers in all steps of the algorithm.

First, we consider the Hamiltonian for $\eta = 0$ (referred to as "isotropic" point below) where Eq. (6.4) simplifies to

$$H_0 = \frac{J}{2} \sum_i (\boldsymbol{S}_i \cdot \boldsymbol{S}_{i+1} + 1) \left(\boldsymbol{\tau}_i \cdot \boldsymbol{\tau}_{i+1} + \frac{1}{4} \right) . \tag{6.8}$$

Note that this system has a SU(2)×SU(2) symmetry but not the higher SU(4) symmetry group as possible in the $S = 1/2$ case (see Eq. (6.3)). We therefore expect physics being rather different from the critical properties of a gapless SU(N) symmetric model. Regarding only a single bond, the lowest energy $-J/2$ is obtained if the orbitals form

a singlet with $\langle \boldsymbol{\tau}_i \cdot \boldsymbol{\tau}_{i+1} \rangle = -3/4$ and the spins are ferromagnetically aligned. The first excited state is given by a spin singlet/orbital triplet and is separated by a gap of $J/4$ only. Therefore a strong orbital dimerization in the ground state is expected leading to alternating ferromagnetic-antiferromagnetic spin exchange couplings, which would be given by $-J/4$ and $+J/8$ for perfect dimerization. Due to translational invariance the corresponding classical ground state would be fourfold degenerate. A picture of this classical ground state, where quantum fluctuations are neglected, is shown in Fig. 6.2. We also

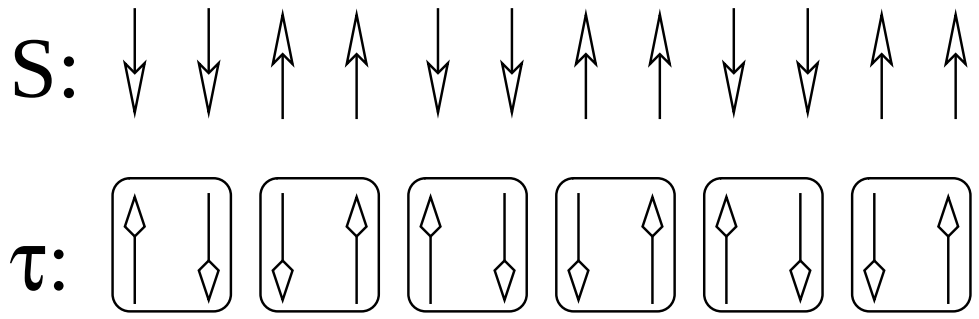

Figure 6.2: The figure shows a classical representation of the expected ground state in the isotropic case ($\eta = 0$). The orbitals form perfect dimers indicated by the boxes and the spins show a Néel order, but with a 4 site periodicity due to the alternating ferromagnetic-antiferromagnetic exchange.

might expect mixed spin-orbital excitations playing an important role in thermodynamics due to the relatively small gap towards the spin singlet/orbital triplet formation. In Fig. 6.3 the temperature dependence of the nearest neighbour spin-spin correlation function $\langle \boldsymbol{S}_i \cdot \boldsymbol{S}_{i+1} \rangle$ and orbital-orbital correlation function $\langle \boldsymbol{\tau}_i \cdot \boldsymbol{\tau}_{i+1} \rangle$ for different η values is shown. A nearest neighbour correlation is easily calculated within the TMRG algorithm as a local expectation value according to Eq. (2.30). First, we want to discuss in more detail the case $\eta = 0$ and turn to finite Hund's coupling later on. Note that in the zero temperature limit the nearest neighbour orbital correlation approaches a value near $-3/8$, the value for perfect dimerization. In the high temperature limit the orbitals are completely disordered and the spin pair correlation is therefore negative. While lowering the temperature orbital singlets are formed and $\langle \boldsymbol{S}_i \cdot \boldsymbol{S}_{i+1} \rangle$ increases due to the ferromagnetic spin interaction within an orbital singlet. The curve reaches a maximum at $T/J \approx 0.13$ corresponding to the energy scale of the orbital gap (see Fig. 6.5) and antiferromagnetic quantum fluctuations of spins in neighbouring orbital singlets are strongly enhanced and dominate below. This emphasizes the differences between a quantum model with $S = 1$ and the classical limit $S \gg 1$ investigated by Shen *et al.* [75], where fluctuations in the antiferromagnetic bonds completely vanish.

An alternating ferromagnetic-antiferromagnetic spin exchange should also show up in the spin-spin correlation function $\langle S_0^z S_r^z \rangle$ showing 4 site periodicity (i.e. $\pi/2$-oscillations) and in a spin dimer correlation function $\langle S_0^z S_1^z S_r^z S_{r+1}^z \rangle$ with long range order and π-oscillations. In Fig. 6.4 numerical results for some leading CLs and the corresponding wavevectors are shown. Because it is known from conformal field theory that CLs ξ

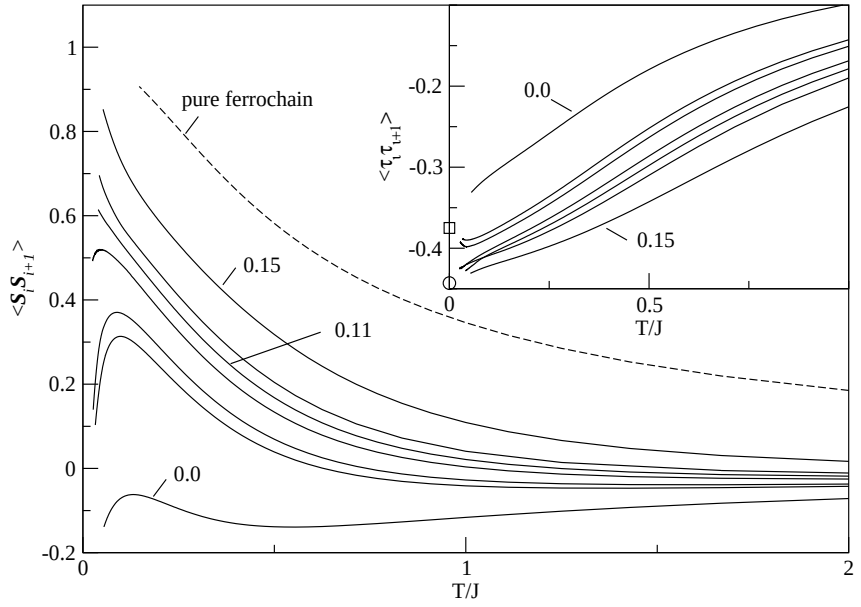

Figure 6.3: The main figure (inset) shows the temperature dependence of nearest neighbour correlations $\langle \boldsymbol{S}_i \cdot \boldsymbol{S}_{i+1} \rangle$ ($\langle \boldsymbol{\tau}_i \cdot \boldsymbol{\tau}_{i+1} \rangle$) for η values 0.0, 0.07, 0.08, 0.1, 0.11, 0.12, 0.15. For comparison the spin only case is shown, where $J_{i,j}$ is fixed by its zero temperature expectation value for $\eta = 0.15$. The circle (square) at $T = 0$ in the inset denotes $-\ln 2 + 1/4$ ($-3/8$).

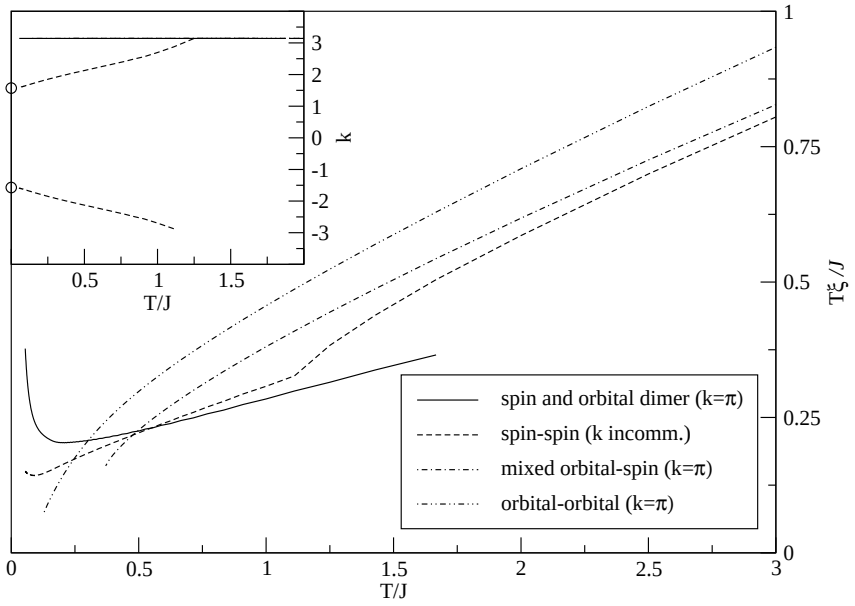

Figure 6.4: The main figure shows the leading CLs times temperature in the isotropic case; the inset shows the corresponding wavevectors with circles denoting $k = \pm\pi/2$.

belonging to critical excitations diverge as $\xi \sim 1/T$ in the low-temperature limit as discussed in detail in chapter 5, CL times temperature versus temperature is plotted,

thus separating correlation functions with long range order at $T = 0$ from short range correlations. A dimer CL showing $k = \pi$ oscillations diverges as $\xi \sim \exp(\Delta_D/T)/\sqrt{T}$ with $\Delta_D \approx 0.08$ in the low-temperature limit indicating long-range dimer order at zero temperature. Second largest at low temperatures is a longitudinal spin-spin CL showing incommensurate oscillations approaching $\pi/2$ at zero temperature. Thus, the numerical results are consistent with the picture above. Note also that at high temperatures the orbitals have a short range antiferromagnetic order and that a spin-orbital CL shows up, indicating the importance of mixed excitations.

For a dimerized orbital pseudospin-1/2 as well as for a $S = 1$ ferromagnetic-antiferromagnetic alternating Heisenberg chain a gap in the excitation spectrum is expected as visible in the numerical data for the uniform spin and orbital susceptibility shown in Fig. 6.5. The

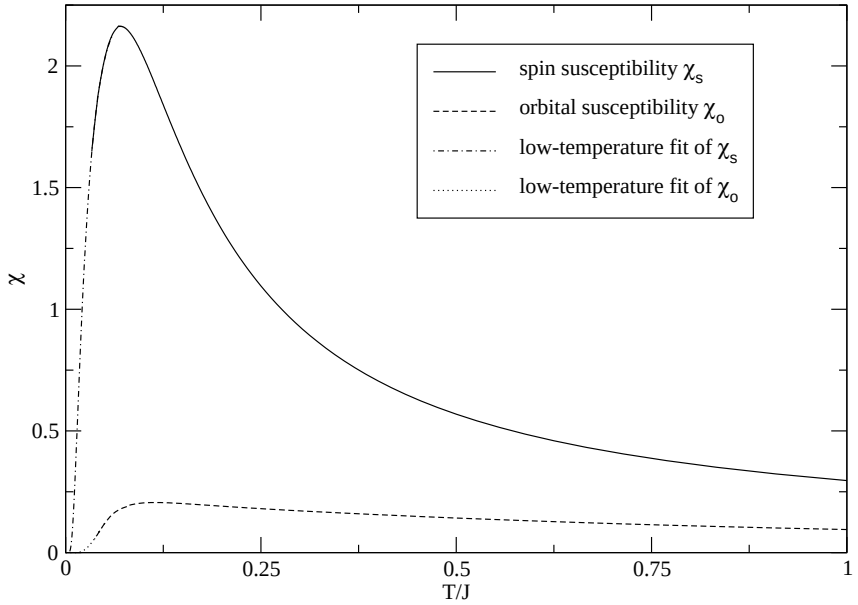

Figure 6.5: Spin and orbital susceptibility for $\eta = 0$ with low-temperature fits as specified in the text.

quadratic dispersion of a gapped system leads in 1D to the low-temperature asymptotics $\chi \sim \exp(-\Delta/T)/\sqrt{T}$. Using this function for a fit, a spin gap $\Delta_s = (0.041 \pm 0.002)J$ and an orbital gap $\Delta_o = (0.120 \pm 0.008)J$ is obtained. Note that the orbital gap is much smaller than the singlet-triplet splitting J of an isolated orbital dimer. The reason is that in the coupled spin-orbital system the spins form a singlet if the orbitals are excited to a triplet configuration and thus, the much smaller gap of the orbital triplet/spin singlet excitation appears in the orbital susceptibility data. Note also that the thermal gap visible here is half of the spectral gap, so that we obtain $\Delta_o^{spectr.} \sim 0.24\ J$. The origin of the factor 1/2 can be understood as follows. The elementary excitations are spinons each with a gap Δ, but they always appear pairwise so that $\Delta^{spectr.} = 2\Delta$. In the thermodynamic data we see an activated behaviour with a characteristic energy which is given by the gap Δ of an elementary excitation irrespective of whether these excitations appear in pairs or not [76].

The value for the spectral gap we have obtained in this way from the susceptibility data is very close to the value $J/4$ for an isolated bond, showing that the orbitals are nearly perfect dimers in the ground state. Dynamic coupling of two sectors also affects the spin gap value. In a simple picture of spin-2 objects coupled antiferromagnetically with $J/32$ [75], one would expect the $S = 2$ Haldane gap of about $0.04(J/32) = J/800$ [77]. However, this mapping is only exact if the ferromagnetic couplings within the dimers tend to $-\infty$. The observed spin gap is in fact much larger due to the coupling between spins and orbitals: A spin excitation introduces additional antiferromagnetic couplings between the orbital singlets, thus also raising the energy of the orbital sector without destroying the dimer state. Note also that the gap Δ_D from the fit of the dimer correlation length is just, as expected, twice the spin gap Δ_s supporting the estimate from the susceptibility data.

In the specific heat of the isotropic model shown in Fig. 6.6 two peaks are visible. The high T peak is due to orbital and mixed spin-orbital excitations whereas the low T peak is caused by spin excitations only.

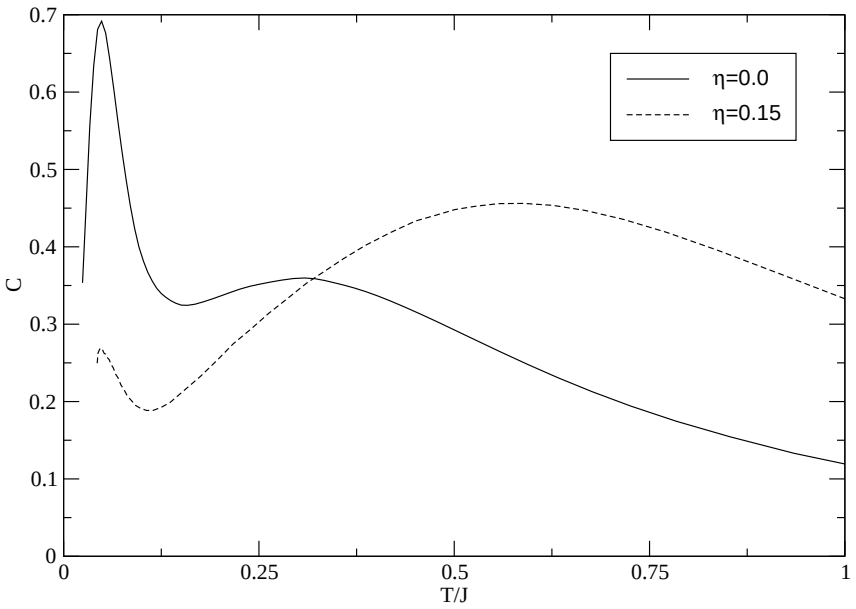

Figure 6.6: Specific heat for the isotropic ($\eta = 0.0$) and the finite Hund's coupling case ($\eta = 0.15$).

Now we will discuss the effects of finite Hund's coupling. As is easily understood from Eqs. (6.4, 6.5), an additional orbital free term R tends to stabilize a ferromagnetic spin order at large values of η.[5] Numerical data for $\eta = 0.15$ indeed show that $\langle \boldsymbol{S}_i \cdot \boldsymbol{S}_{i+1} \rangle$ is monotonously increasing and reaches 1, the value expected for a uniform ferrochain, in the zero temperature limit (see Fig. 6.3). This leads to an exact cancellation of the orbital anisotropy terms in the ground state (see Eqs. 6.4, 6.5) and therefore to an isotropic antiferromagnetic coupling of the orbitals. From the Bethe ansatz result for the Heisenberg

[5]Note, that $\eta < 1/3$ is always needed. Therefore η large means η close to $1/3$ so that $R \gg 1$.

chain one expects $\langle \boldsymbol{\tau}_i \cdot \boldsymbol{\tau}_{i+1} \rangle = -\ln(2) + 1/4$ consistent with the numerical result (see Fig. 6.3).

Regarding the specific heat for finite Hund's coupling a drastic change is visible. The hump is shifted to higher temperatures in comparison to the isotropic case, whereas the low T peak is smaller and shifted to lower temperatures. It is striking that the high T hump contains such a large entropy weight. If it is due to orbital excitations only, its entropy weight would be $\ln(2)$, but in fact it is approximately 1. This could be explained by a formation of an intermediate dimer state at finite temperature. In this case the entropy weight of the hump is given by the total entropy $\ln(6)$ minus a spin entropy of $S = 2$ dimers given by $1/2\ln(5)$ consistent with the numerical data. To support this scenario of a temperature driven dimerization further, we have calculated again the leading CLs (see Fig. 6.7). The dimer CL with π oscillations becomes the leading one

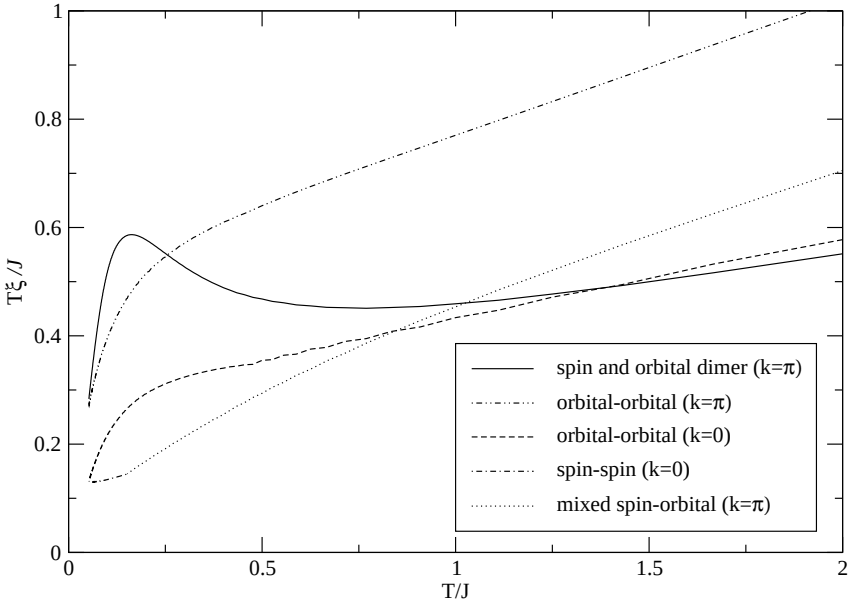

Figure 6.7: The figure shows the leading CLs times temperature for $\eta = 0.15$. Note that all shown CLs have commensurate oscillations over the entire temperature range.

in a certain temperature range before it approaches zero in the low-temperature limit as expected for a uniform ferrochain. This shows that at finite temperatures a dimer state is in fact present just due to entropy reasons. Note also a large orbital CL with π-oscillations indicating antiferromagnetic orbital order. As in the isotropic case a mixed spin-orbital CL shows up at higher temperatures, underlining the importance of such excitations also in the large η limit. At low temperatures there is a non-oscillating spin CL present as expected for a uniform ferrochain. However, this ferromagnetic CL is strongly suppressed at finite temperature due to a disorder effect of low-lying dimerized states. The competition between uniform and dimerized states is also evident from Fig. 6.3: In comparison to the spin only case, where $J_{i,j}$ is fixed by its zero temperature expectation value for $\eta = 0.15$ and therefore all dimerization effects are omitted, $\langle \boldsymbol{S}_i \cdot \boldsymbol{S}_{i+1} \rangle$ shows an

unusually rapid decay of local spin correlations with temperature.

Low temperature asymptotics of spin and orbital expectation values (see Fig. 6.3) suggests first order phase transition between two possible ground states: Spin/orbital dimer phase and spin saturated ferrophase. A critical coupling $\eta_c \sim 0.11$ separating them at zero temperature is just slightly below realistic values for vanadium oxides.[6]

To sum up, the one-dimensional spin-orbital model with $S = 1$ shows an intrinsic tendency towards dimerization. Large Hund's coupling can stabilize a uniform ferromagnetic ground state but strong dimer correlations develop again at finite temperature due to the *orbital Peierls effect*, in which thermal spin fluctuations play a role of lattice degrees of freedom. Dimer states modulate spin and orbital bonds and release high entropy.

6.1.2 Effects of spin-orbit coupling

In the calculations done so far the intra-atomic spin-orbit coupling has been ignored. It is given by

$$H_{SO} = -\Lambda \sum_i \boldsymbol{S}_i \tilde{\boldsymbol{l}}_i \,, \tag{6.9}$$

where $\tilde{l} = 1$ is the effective angular momentum of the t_{2g}^2 state and Λ the spin-orbit coupling constant. The angular momentum $\tilde{l}$ can be represented by

$$\tilde{l}^\alpha = \sum_{m,m'} \sum_\sigma \langle m' | \, \hat{l}^\alpha \, | m \rangle \, d^\dagger_{m'\sigma} d_{m\sigma} \,, \tag{6.10}$$

where $m, m' = xy, xz, yz$, $\hat{l}$ is the angular momentum operator and $d_{m\sigma}$ an annihilation operator for an electron with spin σ and orbital quantum number m. Using the representation by spherical harmonics shown in Eq. (6.1) it is obvious that $\tilde{l}^z$ has matrixelements between xz, yz and $\tilde{l}^\pm$ between xy, xz and xy, yz. The components of $\tilde{\boldsymbol{l}}$ are therefore given by

$$\begin{aligned} \tilde{l}^x &= \mathrm{i}(d^\dagger_{xz} d_{xy} - d^\dagger_{xy} d_{xz}) \\ \tilde{l}^y &= \mathrm{i}(d^\dagger_{yz} d_{xy} - d^\dagger_{xy} d_{yz}) \\ \tilde{l}^z &= \mathrm{i}(d^\dagger_{yz} d_{xz} - d^\dagger_{xz} d_{yz}) = \mathrm{i}(\tau^- - \tau^+) = 2\tau^y \,, \end{aligned} \tag{6.11}$$

where the spin index σ has been suppressed and the pseudospin τ has been used again in the last relation. Because only the xz, yz orbitals are active along the c-axis, we only have to consider the $\tilde{l}^z$ component so that Eq. (6.9) reduces to

$$H_{SO} = -\Lambda \sum_i S_i^z \tilde{l}_i^z = -2\Lambda \sum_i S_i^z \tau_i^y \,. \tag{6.12}$$

[6] A critical value $\eta_c \approx 0.104$ has been recently confirmed by DMRG calculations at zero temperature [78].

This term is difficult to handle within TMRG because it violates the conservation law for the orbital quantum number which is used to reduce the computational effort. However, if $\eta = 0$, the pseudospin space is isotropic (see Eq. (6.8)) and we can replace $S_i^z \tau_i^y$ by $S_i^z \tau_i^z$. In the ferromagnetic ground state for $\eta > \eta_c$ the anisotropy terms cancel each other and we have tested by direct numerical evaluation that their contribution even at finite temperature is rather small. Therefore we have dropped the term $r(\tau_i^z \tau_j^z + 1/4)$ in the operators $\hat{K}_{ij}$ and $\hat{J}_{ij}$ displayed in Eq. (6.5) so that the pseudospin space remains isotropic even for $\eta \neq 0$ and

$$H_{SO} = -2\Lambda \sum_i S_i^z \tau_i^z \tag{6.13}$$

can be used as operator for the spin-orbit coupling in the numerical calculations.

Taking $\Lambda/J = 0.1$ as representative value[7] we have calculated the quantity $\langle S_z^2 \rangle$ and the dimer correlation length as shown in Fig. 6.8. First, we like to mention that the

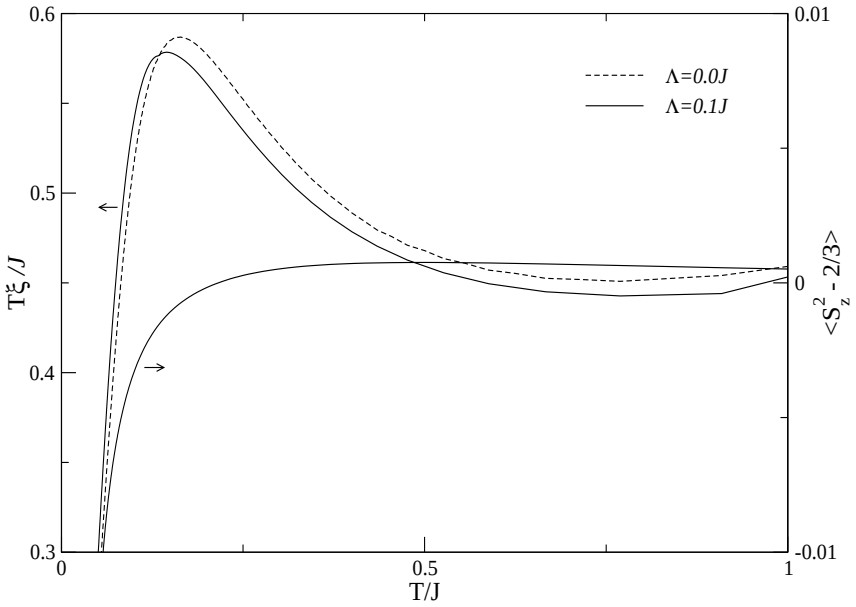

Figure 6.8: For $\eta = 0.15$ and $\Lambda = 0.0J$ (dashed line) and $\Lambda = 0.1J$ (solid line) the dimer correlation length times temperature is shown. Note that the dimerization is only weakly suppressed by the intra-atomic spin-orbit coupling. Additionally the spin-anisotropy $\langle S_z^2 \rangle - \frac{2}{3}$ is shown.

spin-orbit coupling leaves the entropy-driven dimerization almost unaffected. The results and qualitative interpretations derived in the previous section by ignoring this interaction remain valid. For isotropic spin interactions

$$\langle S_z^2 \rangle = \frac{1}{3} S(S+1) = \frac{2}{3} \tag{6.14}$$

[7] $\Lambda/J \sim 0.2$ might be more realistic for YVO_3 [60] but we want to show only qualitatively the effect of spin-orbit coupling in our 1D model.

is expected. The numerical result for finite spin-orbit coupling shows that this quantity is larger than 2/3 for $T/J > 0.2$, approaches this value for $T/J \to \infty$ but becomes smaller than 2/3 for $T/J < 0.2$. Note that the temperature scale where this qualitative change occurs, coincides with the scale where the dimer correlation length becomes leading. The high temperature asymptotics of $\langle S_z^2 \rangle$ is given by

$$\langle S_z^2 \rangle \sim \frac{2}{3} + \frac{\Lambda^2}{9T^2} \tag{6.15}$$

explaining the initial increase when starting at $T/J = \infty$ and lowering the temperature. Physically the spin-orbit term has the tendency to align the z-components of spins and orbital pseudospins at every site. In the high temperature regime spins and orbital pseudospins at different sites are almost uncorrelated and thus the preferred spin direction is the z-axis, i.e. $\langle S_z^2 \rangle > 2/3$. When temperature is lowered, a competition between the superexchange interaction, which prefers antiferromagnetic orbital and ferromagnetic spin correlations, and the spin-orbit coupling, which prefers aligned spins and orbitals at every site, arises. In analogy to a spin-flop transition with a ferromagnetic superexchange for the spins and the τ^z-pseudospin playing the role of a staggered field, the best compromise is a ferromagnetic alignment of spins in the xy-plane while allowing the spins to cant out of the plane in an alternating way to take advantage of the spin-orbit coupling. The interplay between superexchange and spin-orbit coupling therefore leads to an *easy-plane anisotropy*.

6.1.3 Implications for the 3D case and comparison with experimental results for YVO_3

It seems that many of the unusual features of the high temperature C-phase of YVO_3 could be explained semiquantitatively in the one-dimensional spin-orbital model presented here. Especially:

- The dynamical dimerization at $\eta > \eta_c$[8] could explain why in YVO_3 a C-type magnetic order is stable as an intermediate phase. The gain of entropy due to the dimerization lowers the free energy $F = \langle H \rangle - TS$ at finite temperature and stabilizes a formation of alternating weak and strong ferrobonds along one cubic axis (e.g. c-axis). In other words, a dimerization of the *ferromagnetic* spin chain occurs due to the *orbital Peierls effect*, in which thermal spin fluctuations play a role of lattice degrees of freedom. The result is the modulation of the bond couplings in the spin and orbital sector. With $J \sim 40\,\mathrm{meV}$ extracted from the low temperature magnon dispersions [58], the temperature range in which the dimerization is the leading instability in the one-dimensional model coincides with the high temperature phase of YVO_3.

[8] $\eta \sim 0.12 > \eta_c \sim 0.104$ is realistic for YVO_3 [65].

- The dimerization is a natural explanation for the optical-acoustic splitting observed in the magnon spectrum along the c-axis [58]. As the dimerization is of electronic origin, concomitant lattice distortions are expected to be small because t_{2g} orbitals are not bond oriented and only weakly coupled to the lattice. However, the lattice may react to the dimerization of the spin/orbital chains to a certain extent, but this has not been observed until now. A reinvestigation of the crystal structure in the light of the derived results is therefore desirable.

- The strong orbital fluctuations provide an explanation why the ordered moment in the high temperature phase is so small. The numerical results for the nearest neighbour spin correlation (see Fig.6.3) show a substantial suppression in the spin-orbital model when compared to the spin-only ferromagnetic chain.

- The experimentally observed easy-plane anisotropy could be attributed to the intra-atomic spin-orbit coupling as shown in the previous section.

- The canting of the spins away of the ab-plane, $\sim 16.5°$, is a result of the spin-flop transition. Numerically, we find for the on-site correlator $\langle S_i^z \tau_i^z \rangle$ the temperature dependence shown in Fig. 6.9. For the temperature range of interest, $T/J \sim 0.25$,

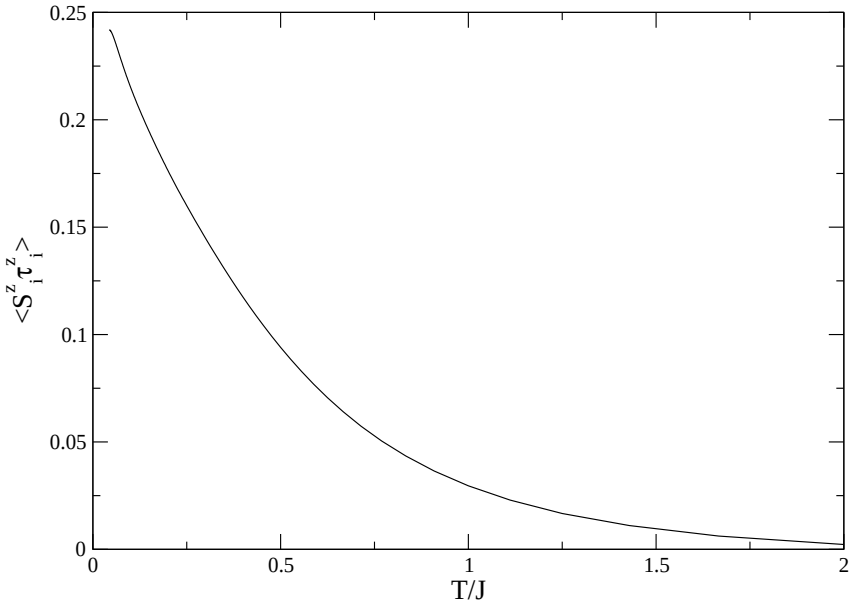

Figure 6.9: $\langle S_i^z \tau_i^z \rangle$ as a function of temperature for $\eta = 0.15$ and $\Lambda = 0.2$.

we find $\langle S_i^z \tau_i^z \rangle \sim 0.15$. In a rather primitive and perhaps not well justified classical estimation this leads to $\sin\theta \sim 0.3$, i.e. a spin canting angle $\theta \sim 17.5°$. Another possible way to explain that the spin-orbit coupling is sufficient to explain the large canting angle is given by the following mean-field approach. $\boldsymbol{S}$ is treated as a

classical spin with

$$\boldsymbol{S} = S \begin{pmatrix} \cos\phi\cos\theta \\ \sin\phi\cos\theta \\ \sin\theta \end{pmatrix} \tag{6.16}$$

and a spin configuration is assumed where the spins are ferromagnetically aligned in the xy-plane and additionally have a small staggered S^z component. This leads to

$$\boldsymbol{S}_i\boldsymbol{S}_{i+1} = S^2(\cos^2\theta - \sin^2\theta) \qquad , \qquad S_i^z = (-1)^i S\,\sin\theta\,. \tag{6.17}$$

Using the Hamiltonian in Eq. (6.4) with this classical spin state and the spin-orbit term (6.13) added, we obtain

$$H = J\sum_i \left[(1-\sin^2\theta)\hat{J}_{i,i+1} + \hat{K}_{i,i+1} - 2\Lambda\sin\theta(-1)^i\tau_i^z\right]\,, \tag{6.18}$$

where $S=1$ has been used. With $H_0 = J\sum_i(\hat{J}_{i,i+1}+\hat{K}_{i,i+1})$ being the Hamiltonian of a spin-1/2 critical system[9] and replacing $\hat{J}_{i,i+1}$ by its zero temperature expectation value we finally derive

$$H = H_0 + J\sum_i \left[0.583\sin^2\theta - 2\Lambda\sin\theta(-1)^i\tau_i^z\right]\,. \tag{6.19}$$

The last term is a staggered magnetic field with strength $h_{\rm eff} = 2\Lambda\sin\theta$ and a perturbation of the critical system H_0. The energy-energy correlation of this perturbation is given by

$$\langle\tau_0^z\tau_r^z\rangle_0 = \frac{(-1)^r}{r} \propto \frac{1}{r^{2x}}\,, \tag{6.20}$$

i.e. the scaling dimension is $x=1/2$. Scaling arguments lead to $E \propto h_{\rm eff}^{d/(d-x)} = h_{\rm eff}^{4/3}$ with some prefactor of the order 1.[10] Therefore we receive for the variation of the energy

$$\Delta E = -(2\Lambda)^{4/3}\sin^{4/3}\theta + 0.583\sin^2\theta\,. \tag{6.21}$$

Minimizing with respect to θ gives

$$\sin\theta \approx 4.892\Lambda^2\,. \tag{6.22}$$

To get a canting of the experimentally observed order, $\Lambda \sim 0.25J$ is needed within this classical approximation. This is in the expected range, thus further supporting that the canting is due to the intra-atomic spin-orbit coupling.

- The model also explains the change of the spin order at T_{N1}: The G-type magnetic order, which is presumably accompanied by a C-type orbital order [56], is favored by the Jahn-Teller coupling to the lattice [22]. This is underscored by a structural transition observed at this temperature [55]. The phase transition to the C-phase is driven by the large entropy content of dimer states as observed in our model.

[9] The anisotropy terms in $\hat{J}_{i,j}$ and $\hat{K}_{i,j}$ again cancel each other.
[10] A more sophisticated argumentation has been given by Schulz [79].

To conclude, the one-dimensional model seems to describe most of the unusual features of YVO_3. However, we have already observed in section 6.1.1 that although the orbital physics is essentially one-dimensional, the spin physics is three-dimensional, i.e. J_{ab} is of the same order as J_c! A one-dimensional model to describe the compound YVO_3 therefore seems to be questionable.

We want to show here that the main results, especially the dimerization, still survive if the coupling J_{ab} between the chains is included on a mean-field level. First of all we need an estimation for J_{ab}. There are three different possibilities leading to different results. In the following discussion we always set $\eta = 0.15$.

- By using formulas (6.6) and (6.7) we get $J_{ab} = \gamma + \delta \langle n_i^{(xz,yz)} n_{i+1}^{(xz,yz)} \rangle = 0.24J + 0.27\langle n_i^{(xz,yz)} n_{i+1}^{(xz,yz)} \rangle J$. Therefore $J_{ab} \approx 0.24J$ if the orbitals are antiferromagnetically ordered, i.e. $\langle n_i^{(xz,yz)} n_{i+1}^{(xz,yz)} \rangle = 0$ or $J_{ab} \approx 0.31J$ if the orbitals are completely disordered, i.e. $\langle n_i^{(xz,yz)} n_{i+1}^{(xz,yz)} \rangle = 1/4$.

- Experimentally $J_{ab}^{\mathrm{exp}} = 2.6\,\mathrm{meV}$ is observed [58]. A fit of the experimental data in the low-temperature G-phase using a Heisenberg model gives an overall superexchange energy scale of $J = 38\,\mathrm{meV}$. Therefore $J_{ab} \approx 0.07J$ is obtained.

- The best way to get an estimation for J_{ab} might be a self-consistent approach. In mean-field approximation the Hamiltonian describing the three-dimensional system (6.4,6.6) transforms into an effective single chain problem and is given by

$$H = H^{(c)} + H^{(a,b)} \rightarrow H^{(c)} + 4J_{a,b}\langle S^z \rangle \sum_i S_i^z - 2NJ_{ab}(\langle S^z \rangle)^2 \,, \tag{6.23}$$

  if an antiferromagnetic order in the ab-plane oriented along the z-direction in spin space is assumed. Here the factor 4 corresponds to the coordination number of the cubic lattice and $J_{a,b}$ is given in units of J. This is the Hamiltonian of a spin chain in an effective magnetic field $h_{\mathrm{eff}} = h + 4J_{a,b}\langle S^z \rangle$. Within linear response $\langle S^z \rangle = \chi_{1D} \cdot h_{\mathrm{eff}}$ leading to

$$\langle S^z \rangle = \frac{\chi_{1D}}{1 - 4J_{ab}\chi_{1D}}\, h \,. \tag{6.24}$$

  This is again the form of a linear response so that we derive for the susceptibility of the three-dimensional system within this approximation [80]

$$\chi_{3D} = \frac{\chi_{1D}}{1 - 4J_{ab}\chi_{1D}} \,. \tag{6.25}$$

  Therefore χ_{3D} diverges if $4J_{ab}\chi_{1D} = 1$. Taking $T_{N1} = 116\,\mathrm{K}$ from experiment, i.e. $T_{N1}/J \approx 0.25$ if $J \sim 40\,\mathrm{meV}$ is assumed, demanding that χ_{3D} diverges at this temperature and using the numerical data for χ_{1D}, we find $J_{ab} = 0.06J$. This is very close to the experimentally obtained value.

Summarizing, the J_{ab} value we get from (6.6) and (6.7) is much larger than that estimated from experiment or self-consistently. The expectation that orbital resonance is completely blocked in the ab-plane might be too naive, giving rise to an overestimation of J_{ab}. Therefore we will use $J_{ab} \sim 0.07J$, which is closer to the experimental and self-consistently estimated value. On the other hand it is also difficult to determine $\langle S^z \rangle$. We will start with $\langle S^z \rangle \sim 0.5$ as observed experimentally [58] leading to a molecular field

$$h_{MF} = 4J_{ab}\langle S^z \rangle \sim 0.15J \; . \tag{6.26}$$

In Fig. 6.10 numerical results for the dimer correlation length with $\eta = 0.15$ and $h_{MF} = 0.15J$ are shown in comparison to the result without molecular field. The maximum in

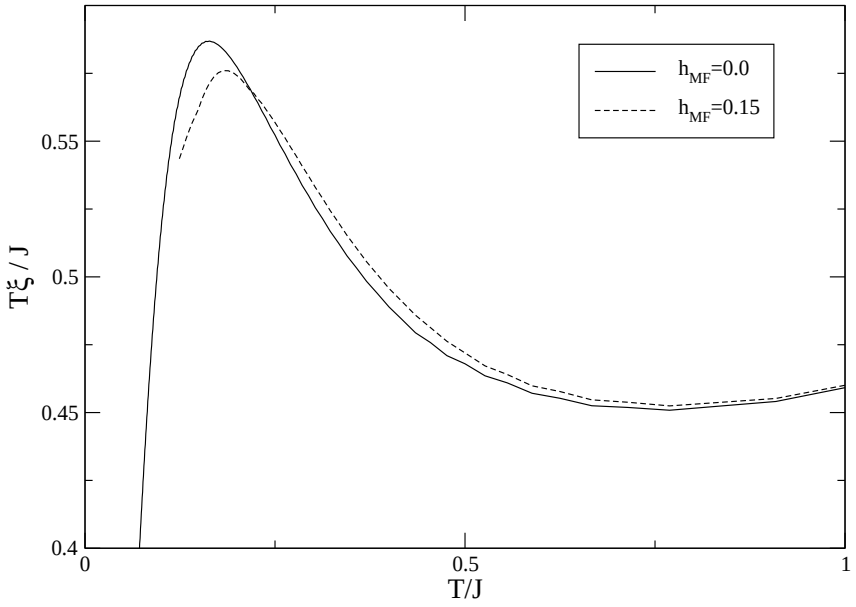

Figure 6.10: Dimer correlation lengths for $\eta = 0.15$ and molecular fields $h_{MF} = 0.0J$ and $0.15J$ showing that the dimerization is only weakly affected by the interchain coupling J_{ab}.

$T\xi$ is only slightly reduced by the molecular field, thus, dimerization along the c-axis still survives if a realistic interchain coupling is included on a mean-field level.

We therefore believe that the one-dimensional model is really appropriate to explain the microscopic origin of the unusual features observed in the high temperature phase of YVO_3 at least qualitatively. The interchain coupling might be important to discuss the numbers in detail, however, the essential physics remains unchanged.

6.2 A one-dimensional spin-orbital model with $S = 1/2$

Whereas the results shown in the previous section present the first theoretical study of a one-dimensional spin-orbital model with $S = 1$, the case $S = 1/2$ has been investigated intensively in the last few years [66, 81, 82, 68, 24, 83]. The Hamiltonian used in most of these works can be displayed as

$$H = \sum_i (\boldsymbol{S}_i \boldsymbol{S}_{i+1} + x)(\boldsymbol{\tau}_i \boldsymbol{\tau}_{i+1} + y) \tag{6.27}$$

with real constants x, y. The model is $SU(2) \times SU(2)$ symmetric and exhibits an additional Z_2 symmetry, interchanging spin and orbital degrees of freedom, if $x = y$. At the special point $(x, y) = (1/4, 1/4)$ the Hamiltonian (6.3) is recovered and the model acquires full $SU(4)$ symmetry and Bethe ansatz integrability [67]. The ground-state phase diagram depending on x, y shows 5 phases [83, 82, 24]: a phase with fully polarized ferromagnetic spins and orbitals (I), phases with antiferromagnetic spin and ferromagnetic orbital states (II) and vice versa (III), a dimerized phase (IV) and a gapless phase (V) which shows $SU(4)$ symmetry up to a rescaling of the spin and orbital velocities (see Fig. 6.11). Although thermodynamic properties of the $SU(4)$ symmetric model have al-

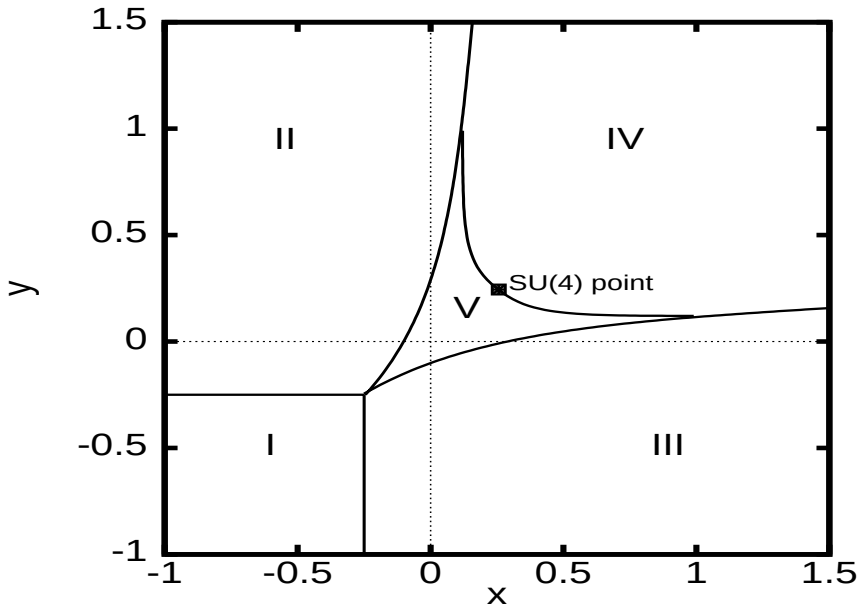

Figure 6.11: Phase diagram for the model Hamiltonian (6.27) taken from Ref. [24]. 5 phases exist as described in the main text.

ready been studied using quantum Monte Carlo algorithms [68], we will start with this special point because it provides a good test for the numerics and allows to compare in detail with Bethe ansatz and conformal field theory. We will concentrate on the comparison of the low-temperature asymptotics of correlation lengths with CFT predictions,

which has not been done in Ref. [68]. Especially logarithmic corrections have not been considered before. In Fig. 6.12 the free energy of the $SU(4)$ model is shown. According

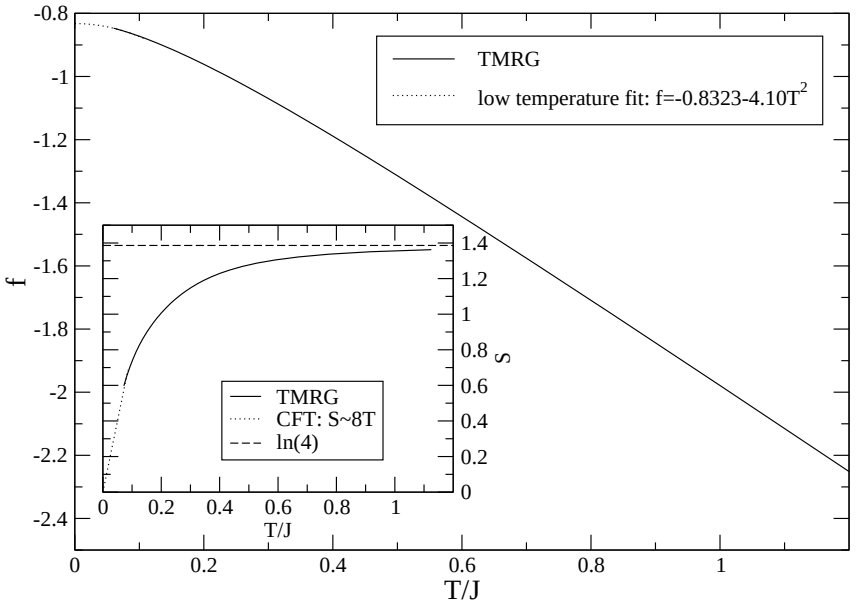

Figure 6.12: Free energy for the $SU(4)$ symmetric model calculated with $N = 248$ states retained. Additionally, the best fit of the low-temperature asymptotics according to Eq. (6.28) is shown. The inset shows the entropy calculated by using numerical derivatives. In the high temperature limit $S \sim \ln 4$ and CFT predicts $S \sim 8T$ for the low-temperature asymptotics.

to Eq. (5.2) we expect for the low-temperature asymptotics from CFT

$$f = e_0 - \frac{\pi c}{6v} T^2 \tag{6.28}$$

with central charge $c = 3$ [23], a velocity $v = \pi/8$ and a ground state energy $e_0 \approx -0.82512$ [67]. By using formula (6.28) for a fit of the numerical data we obtain $e_0 = -0.8323 \pm 0.0004$ and $v = 0.383 \pm 0.009$ in good agreement with the BA results. The error bars have been obtained by a variation of the fit region. The deviation for the ground-state energy is slightly larger due to systematic errors. Contrary to the t-J model (see table 5.1) we obtain reliable results from the fit also for the velocity because the temperature region, where Eq. (6.28) is valid, is larger (see inset of Fig. 6.12).

Next we want to study the leading correlation lengths shown in Fig. 6.13. Due to the $SU(4)$ symmetry the relation

$$\langle S_i^\alpha S_j^\alpha \rangle = \langle \tau_i^\alpha \tau_j^\alpha \rangle = \langle 4 S_i^\alpha \tau_i^\beta S_j^\alpha \tau_j^\beta \rangle \tag{6.29}$$

is valid for the thermodynamic correlation functions with arbitrary components $\alpha, \beta = x, y, z$ [66]. Therefore all CLs shown in Fig. 6.13 have non-zero matrixelements for the spin-spin, orbital-orbital and mixed spin-orbital correlator. In the high temperature limit

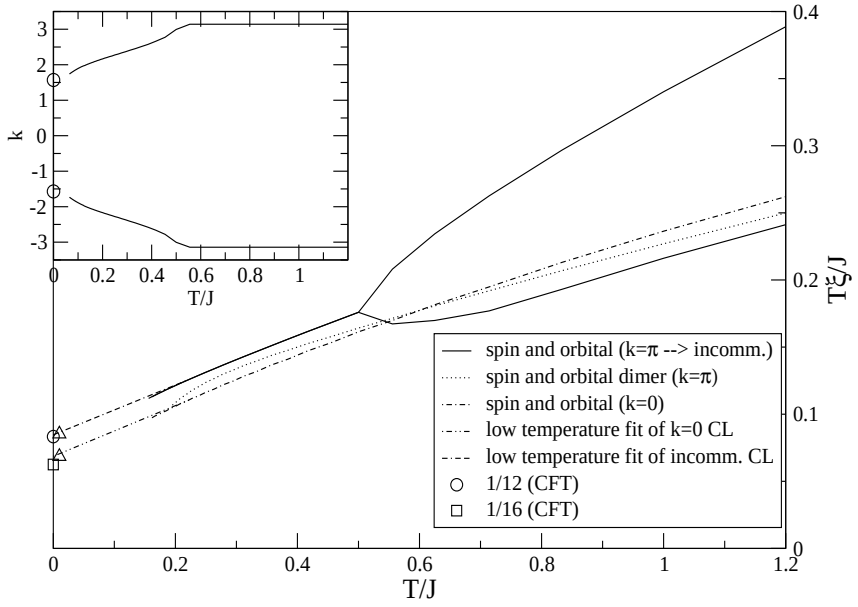

Figure 6.13: Leading spin and orbital correlation lengths for the $SU(4)$ symmetric model. The correlation lengths belonging to critical excitations have non-zero matrixelements for spins and orbitals and diverge $\sim \gamma/T$. The circle (square) denotes the coefficient γ for the $k_F = \pi/2$ (non-oscillating) part as expected from CFT. The triangles illustrate the corrections of the CFT results at finite temperatures due to logarithmic corrections. Additionally a spin and orbital dimer CL is shown which is very close to the leading CL in a certain temperature range. The inset shows the temperature dependence of the wavevector k in the case of incommensurate oscillations.

two of these CLs show π-oscillations (straight lines in Fig. 6.13) and are threefold degenerated. At a temperature $T_c \sim 0.5J$ they merge with a square root singularity[11] and the oscillations become incommensurate at lower temperatures, similar to the behaviour of the longitudinal spin CL in the XXZ-model with finite magnetic field [33]. Additionally a CL is present which is non-oscillating for all temperatures. In the low-temperature limit the CL showing incommensurate oscillations and the non-oscillating CL diverge as

$$\xi = \frac{v}{2\pi x T} \tag{6.30}$$

with the same velocity $v = \pi/8$ but different scaling dimensions x.[12] The possible scaling dimensions for an $SU(N)$ symmetric model are given by $x_p = p(N-p)/N$ with $p = 1, 2, \cdots, N-1$. The dominant mode belongs to $p = 1$ and oscillates at zero temperature at $k_F = 2\pi/N$ [23, 84]. In the case of $SU(4)$, scaling dimensions $3/4, 1, 3/4$ are therefore possible and the dominant mode has $x = 3/4$ and oscillates with $k_F = \pi/2$. Using Eq. (6.30) we obtain $\xi_{\pi/2} = 1/12T$ in good agreement with the low-temperature fit of the numerical data. The non-oscillating CL must belong to the second possible scaling

[11] Note that the number of data points in this temperature region is relatively small.

[12] There are also other CLs diverging like $1/T$ in the low-temperature regime. Here we only discuss the two CLs which are linearly fitted in Fig. 6.13.

dimension $x = 1$ leading to $\xi_0 = 1/16T = 0.0625/T$ in the low-temperature regime. From a fit of the data we obtain $\xi_0 \sim 0.0686/T$ close to the predicted value, but with a significant deviation. This deviation is again as in the t-J model (see Fig. 5.6 in chapter 5) due to logarithmic corrections caused by marginal operators. The multiplicative corrections to the correlator with $k_F = \pi/2$ ($k = 0$) are given by $\ln^{1/8} r$ ($\ln^{1/2} r$). In principle they can be regarded again as an effective correction of the scaling dimension according to Eq. (5.13). However, such a universal logarithmic correction is only obtained at very large length scales by replacing the initial coupling constant of the marginal operator by its long distance renormalization group fixed point [85]. Contrary to the t-J model we are not able to access temperatures where $\xi(T) \gg 1$. Therefore it is not appropriate to apply these universal logarithmic corrections in the temperature region where numerical data have been obtained. Corrections due to marginal operators might be still present there but are determined by the non-universal initial value of the corresponding coupling constant. To illustrate that the logarithmic corrections are of the right order to explain the deviations from the expected CFT values, we have estimated the CLs at $T/J = 0.01$[13] from the linear fits and calculated the effective scaling dimensions by Eq. (5.13). Using the effective scaling dimensions in Eq. (6.30) instead of the "bare scaling dimensions" $x = 3/4, 1$ we obtain the values displayed by the triangles in Fig. 6.13, which are indeed close to the linear fit curves. The logarithmic correction for the non-oscillating CL is more important than the correction for the $\pi/2$-oscillating CL due to the larger exponent $1/2$ compared to $1/8$ in agreement with the numerical results. Finally, we would like to mention that a spin and orbital dimer CL is close to becoming the leading instability even in such a special case with high symmetry. This underlines again that spin-orbital models show an intrinsic tendency towards dimerization, as has also been found in the $S = 1$ spin-orbital model.

Next, we will study the effect of a symmetry breaking perturbation. To understand how the ground state changes when we move away from $(x, y) = (1/4, 1/4)$, it is useful to regard a single bond. At the $SU(4)$ symmetric point the spin singlet/orbital triplet and spin triplet/orbital singlet state are degenerated and lowest in energy. When reducing x with y constant (y with x constant), the spin singlet/orbital triplet (spin triplet/orbital singlet) becomes lower in energy than the spin triplet/orbital singlet (spin singlet/orbital triplet) state. Therefore we expect that a state with antiferromagnetic (ferromagnetic) spins and ferromagnetic (antiferromagnetic) orbitals is stabilized. On the other hand the spin singlet/orbital singlet (spin triplet/orbital triplet) gets lowest in energy if x, y are increased (decreased) far enough along the Z_2 symmetry line [$x = y$] and we therefore expect a dimerized (ferromagnetic spin/ferromagnetic orbital) state. These simple considerations are in agreement with the phase diagram shown in Fig. 6.11. However, one might expect that certain small perturbations $|\delta x| = |x - 1/4| \ll 1$ or $|\delta y| = |y - 1/4| \ll 1$ are irrelevant or only marginal so that the low energy behaviour is still governed by the $SU(4)$ symmetric model. From an RG analysis it is predicted that $\delta x = \delta y < 0$ is irrelevant, $\delta x + \delta y < 0$ with $\delta x \neq \delta y$ is marginal and $\delta x + \delta y > 0$ is relevant [24]. Especially interesting is the marginal case. Lorentz invariance is broken by different spin and orbital velocities but the

[13] At this temperature $\xi \sim 8 \gg 1$ so that the universal logarithmic correction can be applied.

scaling dimensions remain the same as in the $SU(4)$ case. This resembles the Hubbard model [44] or the t-J model [37,38] in that part of the phase diagram where spin and charge excitations are gapless and the low-energy effective theory is given by two independent $c = 1$ Virasoro algebras with different velocities. It is the same kind of generalization of conformal invariance here and the formulas given in chapter 5 are applicable.

In Fig. 6.14 the leading correlation lengths for a system with Hamiltonian (6.27) and $(x, y) = (0.1, 0.25)$, i.e. we consider a marginal perturbation of $SU(4)$ symmetry, are shown. Over a wide temperature range a π-oscillating spin CL is leading. This is expected

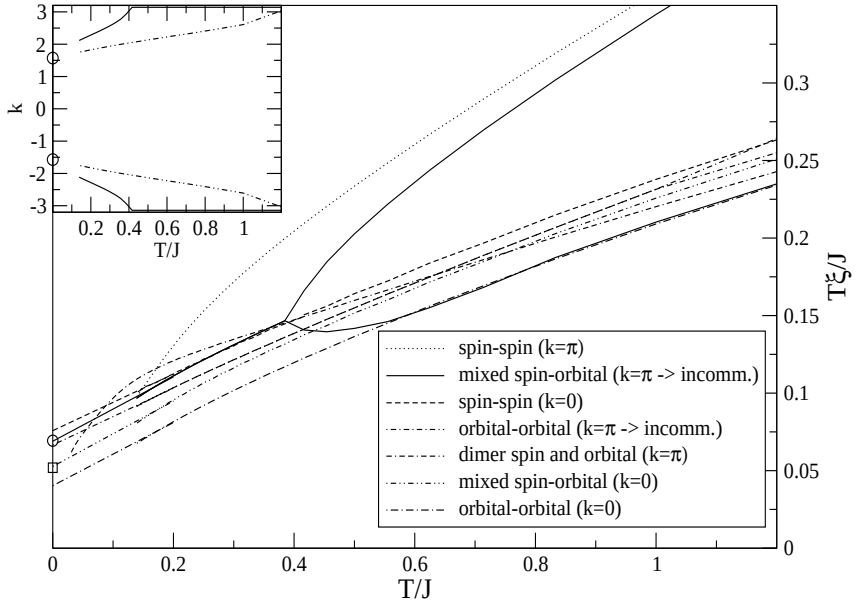

Figure 6.14: Leading spin and orbital correlation lengths for $(x, y) = (0.1, 0.25)$. Numerical data exist down to $T/J \sim 0.15$. The lines at lower temperatures correspond to linear fits of the CLs belonging to critical excitations, i.e. $\xi \sim \gamma/T$. The circle and the square at $T = 0$ display coefficients γ derived by CFT as described in the text. The wavevectors are shown in the inset if incommensurate oscillations occur. The circles in the inset display $\pm\pi/2$.

because antiferromagnetic spin correlations are stabilized with decreasing x as discussed above. As in the $SU(4)$ case two CLs with π-oscillations merge at a temperature $T_c \sim 0.4J$ and show incommensurate oscillations below which approach $\pi/2$ at $T = 0$. However, in the $SU(4)$ case these CLs are threefold degenerate belonging to spin, orbital and mixed spin-orbital correlations. Here no degeneracy is present and the CL only belongs to the mixed spin-orbital correlator. An orbital CL with $\pi/2$ oscillations at $T = 0$ is also present and is diverging with nearly the same factor γ as the mixed spin-orbital CL.[14] At very low temperatures a non-oscillating spin CL is dominating. This CL must belong to a simple particle-hole like excitation with $x_s = 1$ so that $\xi = v_s/2\pi T$ leading to $v_s \approx 0.47$.[15] The corresponding non-oscillating orbital CL is at low-temperatures the smallest CL shown

[14]The deviations are due to different log corrections [24].

[15]We ignore logarithmic corrections here.

in Fig. 6.14. Here we expect $x_o = 1$ and therefore $v_o \approx 0.25$. The fifth CL shown in the low-temperature limit is again a mixed spin-orbital CL, but now with momentum $k = 0$.

We expect that the $SU(4)$ representation is decomposed symmetrically into a spin and orbital sector both with central charge $c = 3/2$ and fundamental fields with scaling dimension $x = 3/8$. The only difference between the two sectors are the velocities. This is completely analogous to Tomonaga-Luttinger liquid theory and the low-temperature asymptotics of CLs is therefore given by Eq. (5.11), where the orbitals play the role of the charge degrees of freedom. The mixed spin-orbital CL and the orbital CL with $k = \pm\pi/2$ at $T = 0$ are given by an excitation with $x_s = x_o = 3/8$ leading to

$$\xi_{\pi/2} = \frac{1}{2\pi\frac{3}{8}(\frac{1}{v_s} + \frac{1}{v_o})T} \approx \frac{0.0693}{T} \tag{6.31}$$

in good agreement with the numerical result (see circle at $T = 0$ in Fig. 6.14). However, from CFT it is expected that also a spin CL with momentum $k = \pm\pi/2$ is present which diverges at low temperatures with the same factor γ [24]. In our numerical data this CL seems to be absent. Numerical data at lower temperatures suggest that the π-oscillating spin CL (dotted line in Fig. 6.14) changes its curvature, merges at very low temperatures with another π-oscillating spin CL and might become the missing CL with incommensurate oscillations. We do not show this data here because the CLs are systematically too small in this very low temperature region due to numerical errors. The mixed spin-orbital CL with $k = 0$ is given by an excitation with $x_s = x_o = 1/2$ leading to

$$\xi_0^{s-o} = \frac{1}{2\pi\frac{1}{2}(\frac{1}{v_s} + \frac{1}{v_o})T} \approx \frac{0.0519}{T} \tag{6.32}$$

which is again in good agreement with the numerics (see square at $T = 0$ in Fig. 6.14). Hitherto we have ignored the dimer CL which is indeed leading in a certain temperature range. This is a little bit astonishing because we have moved away from the dimer phase by $\delta x < 0$. However, the data suggest that this CL remains finite or even vanishes completely at $T = 0$ so that the properties at very low T are really described by the $SU(4)$ correlations with rescaled velocities discussed above. Dimerization is the leading instability in some temperature range although the ground state is not dimerized. The tendency towards dimerization is again stabilized at finite temperatures due to the entropy gain as in the $S = 1$ spin-orbital model with $\eta > \eta_c$ discussed in section 6.1.

In the future it might be interesting to investigate this spin-orbital model in the hole-doped case, where an additional electron hopping term

$$H_{kin} = -t \sum_{\sigma,\tau,i} P\{c^\dagger_{\sigma\tau,i} c_{\sigma\tau,i+1} + h.c.\}P \tag{6.33}$$

is present with σ, τ being the spin and orbital quantum number, respectively, and double occupancy of a site is forbidden.[16] First calculations (data not shown) suggest that low-temperature properties in certain regions of the phase diagram can be described by

[16]The model is therefore a generalized t-J model with additional orbital degrees of freedom.

generalized CFT with three in general different velocities for charge, spin and orbital excitations. However, here the field theory has not yet been performed either and is an interesting topic of future research. Additionally, we found relatively strong superconducting correlations (data not shown) where singlet or triplet pair correlations could be stabilized by the orbital degrees of freedom depending on the parameters x, y. This influence of additional orbital degrees of freedom on superconductivity might be a new avenue for theoretical and experimental research. To perform reliable numerical calculations for this model, further improvements of the algorithm are needed to retain a sufficient number of states within the RG and such improvements seem to be possible in the near future. Apart from TMRG calculations it would also be very interesting to calculate thermodynamics for the $SU(4)$ model by Bethe ansatz.[17] Using the transfer-matrix approach it might be possible to calculate even the correlation lengths analytically so that very low temperatures become accessible and the logarithmic corrections could be studied in detail. Additionally, we would like to mention that also the generalized t-J model in Eq. (6.33) exhibits an integrable point and presents at this special point a generalization of a class of models studied in Ref. [47] by BA.

[17] Astonishingly, up to now only ground-state properties have been calculated by BA.

Chapter 7

A Transfer Matrix Approach to Dynamics at Finite Temperature

The standard approach to calculate dynamical correlation functions at finite temperature is the Matsubara formalism. To evaluate a two-point correlation function $\langle O'_r(t)O_0(0)\rangle$ with operators O, O', one first regards the corresponding imaginary-time correlation function where $\mathrm{i}\,t \to \tau$ and, without loss of generality, $\tau > 0$:

$$\langle O'_r(\tau)O_0(0)\rangle = \frac{\mathrm{Tr}\,\left(\mathrm{e}^{-\beta H}O'_r(\tau)O_0(0)\right)}{\mathrm{Tr}\,\left(\mathrm{e}^{-\beta H}\right)} = \frac{\mathrm{Tr}\,\left(O'_r\mathrm{e}^{-\tau H}O_0\mathrm{e}^{-(\beta-\tau)H}\right)}{\mathrm{Tr}\,\left(\mathrm{e}^{-\beta H}\right)} \tag{7.1}$$

Here the Heisenberg representation $O'_r(\tau) = \exp(\tau H)O'_r\exp(-\tau H)$ and the cyclic invariance of the trace have been used. Due to the cyclic invariance the imaginary-time correlator is β-periodic (β-antiperiodic) if O, O' are bosonic (fermionic) operators. An exact evaluation is possible in a few special cases only. Otherwise perturbation theory or numerical approaches have to be applied. TMRG and QMC are well suited to calculate imaginary-time correlations because these methods directly act in a two-dimensional space, where one direction corresponds to imaginary time (temperature). When using the novel Trotter-Suzuki mapping introduced in chapter 2 the imaginary-time correlation is calculated similarly to the static correlation (see Eqs. (2.36, 2.37, 2.38)) but without performing a τ-integration, i.e.

$$G(r,\tau) = \frac{1}{\Lambda_0^{r+1}}\langle\Psi_0^L|\tilde{T}_M[O(0)]T_M^{r-1}\tilde{T}_M[O'(\epsilon\cdot k)]|\Psi_0^R\rangle \tag{7.2a}$$

for distances $r \geq 1$ and

$$G(r=0,\tau) = \frac{1}{\Lambda_0}\langle\Psi_0^L|\tilde{T}_M[O(0),O'(\epsilon\cdot k)]|\Psi_0^R\rangle\ , \tag{7.2b}$$

where $\tilde{T}_M[O(\epsilon\cdot k)]$ denotes the usual transfer matrix T_M with the considered operator O added at imaginary time position $\tau = \epsilon\cdot k$. A graphical representation for the case $r > 0$ is shown in Fig. 7.1. The calculation of imaginary-time correlations can be easily implemented within TMRG and results with a high accuracy are obtained [86, 87]. The next step is an analytical continuation of the imaginary-time results to real times and presents the crucial problem of this approach. The spectral function $A(\omega)$ is usually obtained by an inversion of

$$G(\tau) = \frac{1}{2\pi}\int_0^\infty K(\tau,\omega)A(\omega)d\omega\ , \tag{7.3}$$

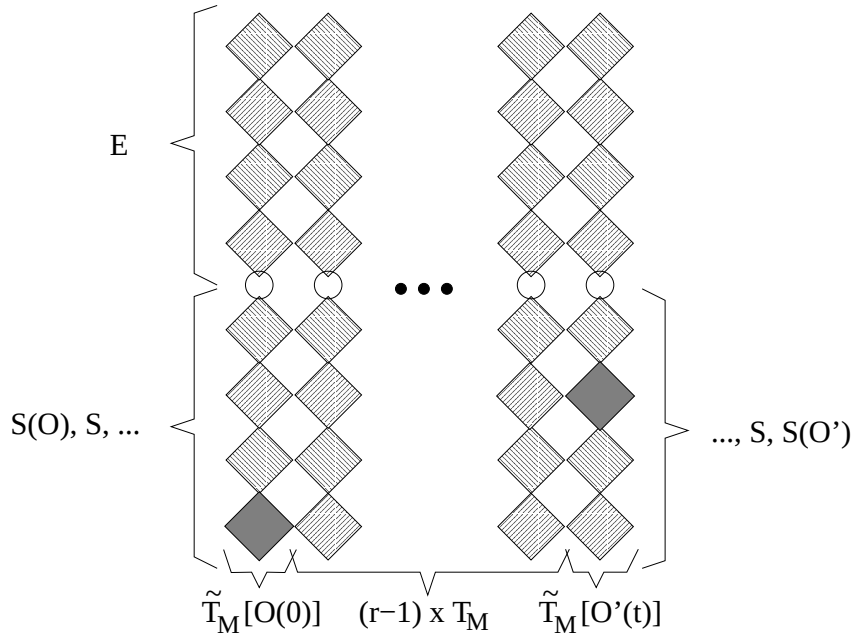

Figure 7.1: To calculate imaginary-time correlations two transfer matrices are modified by adding the considered operators O, O' at position $\tau = 0$ and $\tau = \epsilon \cdot k$, respectively. This is denoted in the figure by the shaded plaquettes. Between the two modified transfer matrices $r-1$ usual transfer matrices exist. Note that the operators have to be added only to the system block due to the β-periodicity. Each modified system block $S(O)$, $S(O')$ has to be stored and renormalized separately. By connecting the modified system block with a usual environment block E the modified transfer matrix $\tilde{T}_M$ is formed.

where e.g. the integration kernel is given by $K(\tau, \omega) = \exp[-\tau\omega] + \exp[-(\beta - \tau)\omega]$ for bosonic operators. A direct inversion via Fourier transform is applicable if $G(\tau)$ is given in an analytic form, but it does not work for numerical results because small errors in $G(\tau)$ are exponentially amplified by the singular integration kernel leading to complete nonsense [86].

The analytical continuation of imaginary-time correlations to real times is an ill-conditioned inversion problem.

In such a case the only thing one can do is to use certain filter functions to find the most probable spectral function $A(\omega)$, i.e. the spectral function which is best compatible with the noisy and incomplete data for $G(\tau)$. Among the different possibilities the maximum entropy method is most popular and has been widely used for the analytical continuation of QMC or TMRG data. We do not want to discuss these methods in detail but just fix the following points: As long as the spectral function is flat this approach is working, but it is not able to reproduce the height or shape of existing peaks and it often produces artificially non-existing peaks at arbitrary positions. This is an inherent property of this approach, which cannot be solved by modifying the filter function and which occurs even for numerical data with a utopian accuracy [88]. To conclude, the Matsubara formalism to

calculate dynamic correlations at finite temperatures is in no way satisfying when applied in numerical calculations and leads to unreliable results.

Because the analytical-continuation problem cannot be solved, we have to elude it. Here we want to propose a new approach also based on the transfer matrix formalism to directly calculate real-time correlations at non-zero temperature. Starting point is the usual formula for a dynamic correlation function

$$\langle O_0(0)O_r'(t)\rangle = \frac{\mathrm{Tr}\,\left(O_0(0)O_r'(t)\mathrm{e}^{-\beta H}\right)}{\mathrm{Tr}\,\left(\mathrm{e}^{-\beta H}\right)} = \frac{\mathrm{Tr}\,\left(O_0\mathrm{e}^{\mathrm{i}tH}O_r'\mathrm{e}^{-\mathrm{i}tH}\mathrm{e}^{-\beta H}\right)}{\mathrm{Tr}\,\left(\mathrm{e}^{\mathrm{i}tH}\mathrm{e}^{-\mathrm{i}tH}\mathrm{e}^{-\beta H}\right)}\ , \tag{7.4}$$

where the Heisenberg representation of the time-dependent operator has been used and a factor 1 has been introduced in the denominator. The idea is now to perform *independent Trotter-Suzuki decompositions for inverse temperature β and for real time t.* Using the novel mapping and defining the row-to-row transfer matrices

$$\begin{aligned} T_{1,2}(\epsilon) &= T_{R,L}\exp[-\epsilon H + \mathcal{O}(\epsilon^2)] \\ U_{1,2}(\delta) &= T_{R,L}\exp[\mathrm{i}\delta H + \mathcal{O}(\epsilon^2)] \\ \tilde{U}_{1,2}(\delta) &= T_{R,L}\exp[-\mathrm{i}\delta H + \mathcal{O}(\epsilon^2)]\ , \end{aligned} \tag{7.5}$$

where $\epsilon = \beta/M$ and $\delta = t/N$ the correlation function (7.4) can be displayed as

$$\langle O_0(0)O_r'(t)\rangle = \lim_{M\to\infty}\lim_{N\to\infty}\frac{\mathrm{Tr}\,\left(O_0[U_1(\delta)U_2(\delta)]^{N/2}O_r'[\tilde{U}_1(\delta)\tilde{U}_2(\delta)]^{N/2}[T_1(\epsilon)T_2(\epsilon)]^{M/2}\right)}{\mathrm{Tr}\,\left([U_1(\delta)U_2(\delta)]^{N/2}[\tilde{U}_1(\delta)\tilde{U}_2(\delta)]^{N/2}[T_1(\epsilon)T_2(\epsilon)]^{M/2}\right)}\ . \tag{7.6}$$

Rearranging the local Boltzmann weights to form a QTM (column-to-column transfer matrix) we find for distances $r > 0$

$$\begin{aligned} \langle O_0(0)O_r'(t)\rangle &= \lim_{\epsilon\to 0}\lim_{\delta\to 0}\lim_{L\to\infty}\frac{\mathrm{Tr}\,\left(\tilde{T}_{2N,M}[O(0)]T_{2N,M}^{r-1}\tilde{T}_{2N,M}[O'(t)]T_{2N,M}^{L-(r+1)}\right)}{\mathrm{Tr}\,\left(T_{2N,M}^{L}\right)} \\ &= \lim_{\epsilon\to 0}\lim_{\delta\to 0}\frac{\left\langle\Psi_0^L\right|\tilde{T}_{2N,M}[O(0)]T_{2N,M}^{r-1}\tilde{T}_{2N,M}[O'(t)]\left|\Psi_0^R\right\rangle}{\Lambda_0^{r+1}}\ , \end{aligned} \tag{7.7}$$

where the transfer matrix $T_{2N,M}$ and the modified transfer matrix $\tilde{T}_{2N,M}$ are depicted graphically in Fig. 7.2. Λ_0 is the largest eigenvalue belonging to $T_{2N,M}$ and $\left\langle\Psi_0^L\right|$, $\left|\Psi_0^R\right\rangle$ are the corresponding left and right eigenvectors. The autocorrelation is given by

$$\langle O_0(0)O_0'(t)\rangle = \lim_{\epsilon\to 0}\lim_{\delta\to 0}\frac{\left\langle\Psi_0^L\right|\tilde{T}_{2N,M}[O(0),O'(t)]\left|\Psi_0^R\right\rangle}{\Lambda_0}\ , \tag{7.8}$$

where both operators are located in the same column-to-column transfer matrix $\tilde{T}_{2N,M}$.

As a consequence the transfer matrices $T_{2N,M}$ and $\tilde{T}_{2N,M}$ now have complex entries. The easiest way to handle these QTMs is to store and renormalize the "real-time" and the

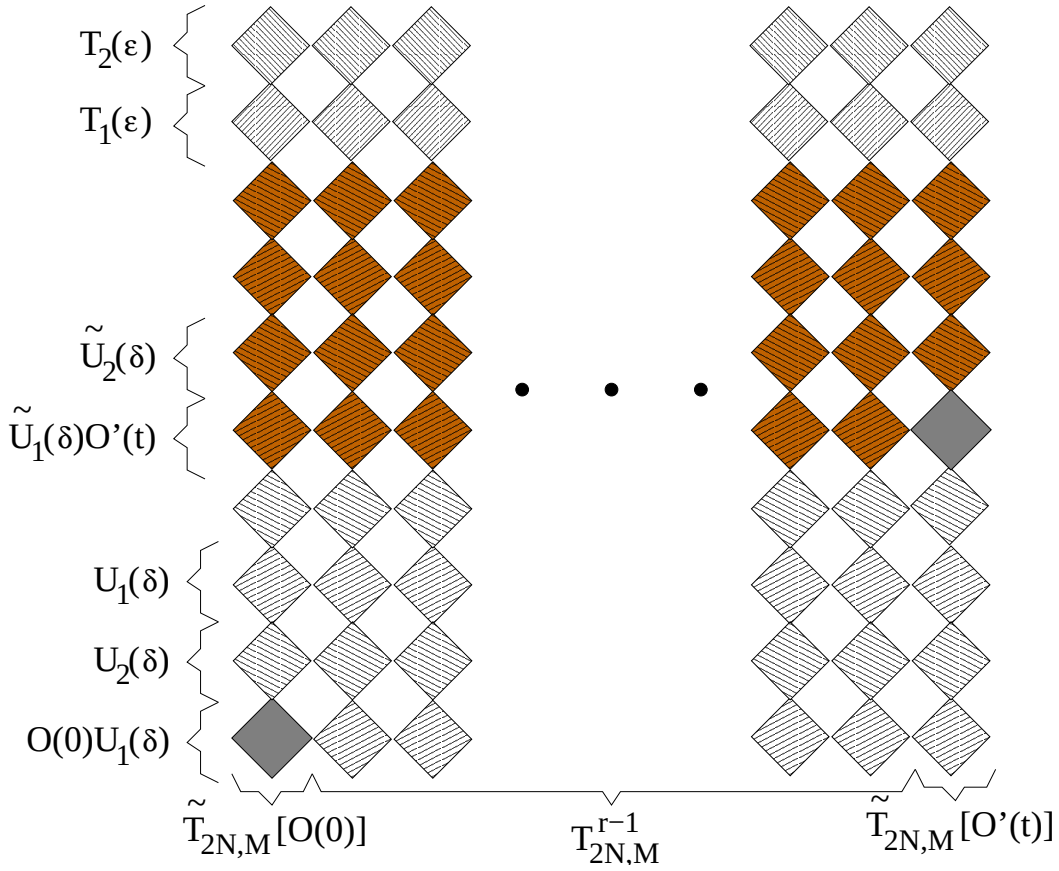

Figure 7.2: The figure shows the QTM, $T_{2N,M}$, and the modified QTM, $\tilde{T}_{2N,M}$, needed to calculate a real-time correlation function for $r > 0$ within the novel approach. $T_{2N,M}$ consists of three parts (from bottom to top): A part describing $\exp(\mathrm{i}tH)$, another describing $\exp(-\mathrm{i}tH)$ and a third part which is just the usual "thermodynamic" transfer matrix for $\exp(-\beta H)$. In the modified QTM, $\tilde{T}_{2N,M}$, the considered operator has been added at the appropriate position.

"thermodynamic" part separately. The complete transfer matrix is only needed to perform matrix-vector multiplications and this can again be implemented by acting consecutively with the parts of the transfer matrix on the vector as in Eq. (3.1). The DMRG algorithm is used to extend both parts as in the usual thermodynamic TMRG. To show that this approach is really promising, we start with the limiting case of infinite temperature, where the "thermodynamic" part of the transfer matrix is absent. This simplifies the problem but keeps the essential feature of the novel approach, namely the real-time transfer matrix representation $O_0 \mathrm{e}^{\mathrm{i}tH} O_r' \mathrm{e}^{-\mathrm{i}tH} = O_0 [U_1(\delta) U_2(\delta)]^{N/2} O_r' [\tilde{U}_1(\delta) \tilde{U}_2(\delta)]^{N/2}$, intact.

7.1 Autocorrelations in the spin-1/2 XXZ-model at $T = \infty$

Although the spin-1/2 XXZ-model is exactly solvable by Bethe ansatz and ground-state as well as thermodynamic properties have been studied intensively over decades, the behaviour of its autocorrelations is still an unsolved problem even at infinite temperature. To test our new approach for a real-time correlation function $\langle O_0(0)O_r'(t)\rangle$, we restrict ourselves to infinite temperature and autocorrelations in a widely studied system, but surprisingly we are still dealing with a serious unsolved problem! This shows impressively that dynamics in quantum systems is very hard to tackle and that not much progress has been achieved so far. So this limiting case is not only a simple test, the results might be a step forward and physically interesting on their own.

Exact results are only known in the free fermion case ($\Delta = 0$), where one finds for the longitudinal spin autocorrelation

$$\langle S_0^z(0)S_0^z(t)\rangle = \frac{1}{4}\left[J_0(Jt)\right]^2 \tag{7.9}$$

when the Hamiltonian (4.2) is used as shown in appendix B (see especially Eq. (B.13)). Here J_0 is the Bessel function of order zero. For $\Delta \neq 0$ no exact results are available yet[1] and all that is known stems from numerical calculations [89, 90, 91]. The aim of these works is to investigate the long-time behaviour of the longitudinal spin autocorrelation function. For this quantity[2] the phenomenological theory of spin diffusion proposed by Bloembergen [92] and de Gennes [93] predicts

$$\langle S_0^z(0)S_0^z(t)\rangle \sim t^{-D/2} \tag{7.10}$$

for the long-time behaviour in any dimension D. This prediction definitely fails at least in the 1D free fermion case because the long-time behaviour of Eq. (7.9) is given by $\langle S_0^z(0)S_0^z(t)\rangle \sim 1/t$. The exact diagonalizations of chains with lengths up to 16 sites in Ref. [91] suggest that the ballistic asymptotic behaviour at the free fermion point holds for all $0 \leq \Delta < 1$. However, exact diagonalization yields only reliable results for relatively short times so that it is questionable if the long-time behaviour is governed by the data. Even if one accepts the assumption that the behaviour at short and long time scales is identical, it is impossible to extract the exact exponent of the decay of the autocorrelation with time from that data. Summarizing, we still have, after much effort, only assumptions about the behaviour of the autocorrelation function in the spin-1/2 XXZ-model at infinite temperature away from the free fermion point.

To prevent possible instabilities due to the separate calculation of the right and left eigensystem in the novel Trotter-Suzuki representation, we have decided to use the traditional checkerboard decomposition. Because we are only interested in autocorrelations of a spin-1/2 system the disadvantages of this Trotter-Suzuki mapping such as the larger amount

[1] Due to the Bethe ansatz integrability it seems to be not impossible to make progress in this direction.
[2] It is important that the considered operator obeys a conservation law.

of memory needed and the unnecessary large repeat length of the QTM have no weight. The formula (7.8) is valid for both mappings where $\tilde{T}_{2N,M}[O(0), O'(t)]$ is replaced by the transfer matrix shown in Fig. 7.3 if the traditional mapping is applied. The easiest way,

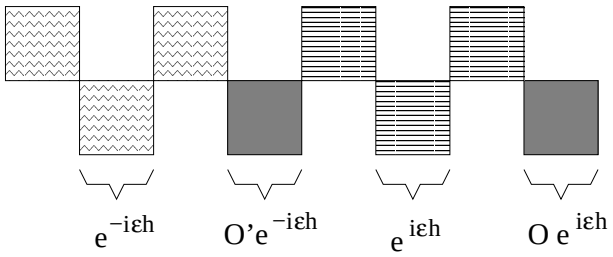

Figure 7.3: Transfer matrix $\tilde{T}_{2N,M}[O(0), O'(t)]$ needed to calculate the autocorrelation at infinite temperature with the traditional algorithm in a 90° rotated view.

but presumably not the numerically best way as discussed later on, to apply the standard transfer matrix DMRG onto $\tilde{T}_{2N,M}$ is to use the part representing $\exp(\mathrm{i}\epsilon H)$ as system block and the part representing $\exp(-\mathrm{i}\epsilon H)$ as environment block. I.e. the transfer matrix shown in Fig. 7.3 is cut exactly in the middle. The advantage is that each block contains only one kind of Boltzmann weights and that the environment block can be constructed from the system block by a 180° rotation and an additional sign change of the imaginary part. All steps of the algorithm can be implemented as described in chapter 2.2; the only thing one has to care for is that all quantities are now complex.

To compare with an exact result we concentrate on the free fermion case. We believe that this point is not special within this approach and that results with a similar accuracy can be obtained for $\Delta \neq 0$, as has been shown for the thermodynamic TMRG in chapter 4. In Fig. 7.4 numerical results with $N = 400$ states retained in the DMRG are shown. The numerical data and the exact result coincide with relatively small numerical errors of the order 10^{-4} to 10^{-3} up to times $t \sim 6$. Above this time scale numerics breaks down rapidly. This shows that the transfer matrix approach is in principle working and even in this first simple implementation we reach the same time scale as the exact diagonalizations of Fabricius, Löw and Stolze [90] and Fabricius and McCoy [91] for the largest investigated chain length of $L = 16$ sites.

For large t we see from the exact result in Eq. (7.9) that the autocorrelation function behaves as

$$\langle S_0^z(0) S_0^z(t) \rangle \sim t^{-d} [A + B \mathrm{e}^{-\gamma(t-t_0)} \cos(\Omega(t - t_0))] \tag{7.11}$$

where we have used the same notation as in Ref. [91] and the parameters d, A, B, γ, t_0 and Ω are given in the first row of table 39. The same ansatz (7.11) has been used in Ref. [91] for a fit of the data from exact diagonalization of the 16 site system and the results obtained there are displayed in the second row of table 39. When we perform such a fit in the same time interval for the data obtained by the transfer matrix approach, we receive the values shown in the third row. They agree perfectly with the exact parameters as well as with that obtained from the exact diagonalization data. Therefore not only

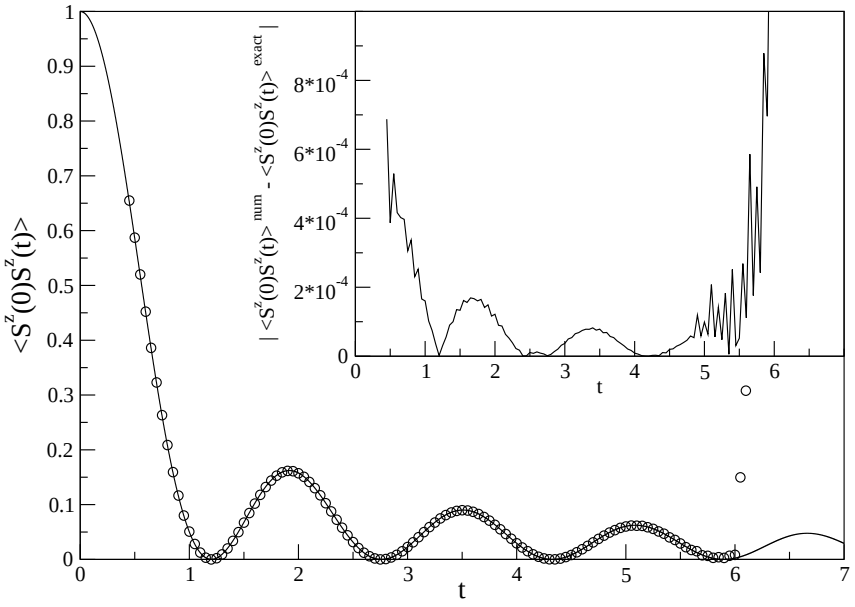

Figure 7.4: The autocorrelation function $\langle S^z(0)S^z(t)\rangle$ for $\Delta = 0.0$ computed with the transfer matrix approach (circles) plotted on the exact result (line). In the DMRG algorithm $N = 400$ states are retained. The inset shows the errors of the numerical data. The normalization $J = 2$ has been chosen in the Hamiltonian (4.2).

method	d	A	B	γ	Ω	t_0	χ^2
exact result	1	$1/2\pi$	$1/2\pi$	0	4	$5\pi/8$	-
exact diag. $L = 16$ [91]	1.000	0.159	0.159	0.000	4.010	1.976	1.199e-07
transfer matrix [here]	1.006	0.159	0.159	0.000	4.011	1.977	4.74e-08

Table 7.1: The large t behaviour of Eq. (7.9) is governed by the asymptotic form (7.11) with parameters displayed in the first row. Using the same formula for a fit of the $L = 16$ exact diagonalization (transfer matrix) data, the parameters in the second (third) row are obtained.

the numerically obtained maximal time but also the precision of the data seems to be comparable in both approaches.

For a first attempt the results of the novel transfer matrix approach are encouraging, nevertheless, we want to discuss why the algorithm breaks down and how the algorithm might be improved. First, we will regard the spectrum of the reduced density matrix used to truncate the Hilbert space when the transfer matrix $\tilde{T}_{2N,M}$ is enlarged. In Fig. 7.5 the spectrum is shown for three different numbers of RG steps M. As in the usual thermodynamic TMRG (see Fig. 3.1) the spectrum becomes denser while increasing the size of the transfer matrix. However, here the spectrum grows up more rapidly and already at $M = 100$ the 10 largest eigenvalues are almost degenerated. Therefore even 400 states are not sufficient to represent the Hilbert space accurately any longer and further RG steps are not possible. Note that we could reach slightly larger times easily by just retaining more states. Although time-consuming, up to $N = 1000$ states are

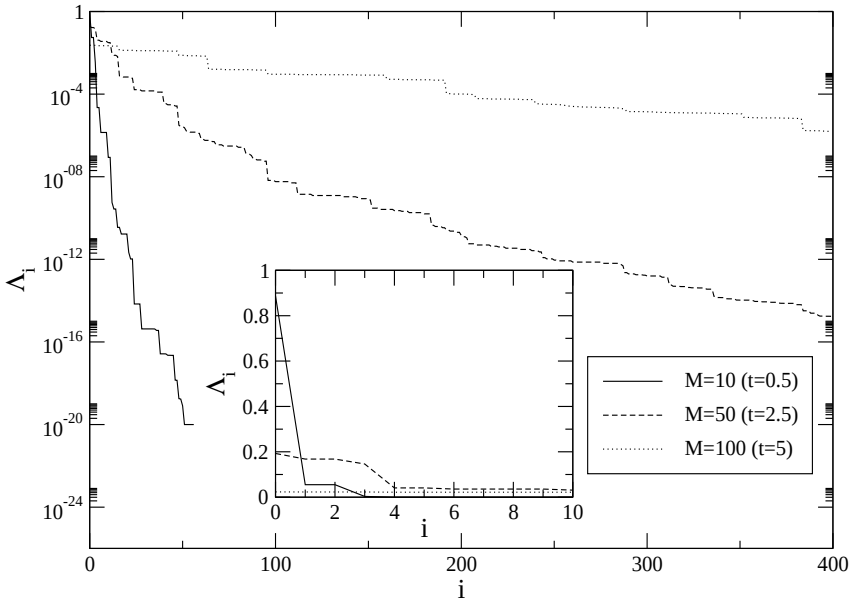

Figure 7.5: Eigenvalue spectrum of the reduced density matrix which is used to truncate the Hilbert space for 10, 50 and 100 renormalization steps. Note that the spectrum is rapidly decaying for a small number of RG steps whereas it becomes dense near the point where the algorithm breaks down. The inset is an enlargement and shows the 10 largest eigenvalues. Note that after 100 RG steps the 10 largest eigenvalues are nearly identical.

possible on a standard PC so that results beyond exact diagonalization could be obtained. However, to receive definite answers about the long-time behaviour of the longitudinal autocorrelation function, we need reliable results for time scales which are at least a factor 2 or 3 larger. This cannot be obtained by only increasing the number of RG states; instead improvements of the algorithm are needed.

The rapid increase of the eigenvalue spectrum of the reduced density matrix suggests that the Hilbert space is truncated in a non-optimal way. This might be a consequence of our asymmetric choice of the system and environment block. Usually the environment acts like a bath and should be completely similar in structure to the system block. However, here the system block represents $\exp(\mathrm{i}\epsilon H)$ and the environment block $\exp(-\mathrm{i}\epsilon H)$. Because the Trotter parameter ϵ is rather small, the difference between the two blocks due to the imaginary parts with opposite sign is negligible for small Trotter numbers M but might be accumulated after many RG steps. Additionally, also the reduced density matrix itself is questionable. It gives the optimal states for adding an $\exp(-\mathrm{i}\epsilon h)$-plaquette to the system block (see Fig. 7.3), but what is really added is an $\exp(\mathrm{i}\epsilon h)$-plaquette. After many iterations this could lead to a representation of the truncated Hilbert space which does not contain the true ground state any longer. Both problems could be solved by taking a symmetric decomposition of the transfer matrix, $\tilde{T}_{2N,M}$, in system and environment block, where each block contains the same number of $\exp(\mathrm{i}\epsilon h)$ and $\exp(-\mathrm{i}\epsilon h)$-weights. However, to keep this structure intact, always 2 weights, an $\exp(\mathrm{i}\epsilon h)$ and an $\exp(-\mathrm{i}\epsilon h)$-weight, have to be added in each RG step. Therefore the implementation requires drastic changes in

the algorithm[3] and we will postpone this possible improvement of the algorithm for future investigations.

We would also like to mention that the kind of breakdown observed here is rather similar to the observations often made in the standard $T = 0$ DMRG (see Noack and White in [26]) when the infinite algorithm is applied. The convergence is often rather poor and it is therefore necessary to additionally apply the so called *finite algorithm*. In the finite algorithm the length of the chain (length of the QTM) remains constant in each RG step by taking the stored system blocks from previous steps as environment. The point where the chain (transfer matrix) is cut into system and environment therefore runs like a zipper from left to right and then back from right to left and each time the direction is changed a new set of stored blocks is used as environment. This procedure improves the representation of the blocks iteratively and an accuracy is obtained which is often orders of magnitude better than that obtained by the infinite algorithm alone. In principle the finite algorithm is also applicable here: The usual (infinite) algorithm is performed until the time is reached where we want to calculate the autocorrelation. Even if we are at time scales where the algorithm fails to converge due to the dense spectrum of the reduced density matrix, it might be possible to find a better representation iteratively by applying the finite algorithm.

We are very optimistic that the possible improvements described here could help to reach larger times t. Especially the alternative symmetric choice of system and environment seems to be very promising. Rather naively, there seems to be not much difference between "dynamic TMRG" with this choice of system and environment block and the usual thermodynamic TMRG and one might expect that a similar number of RG steps are possible which would correspond to $t \sim 100$ in Fig. 7.4! However, even if we could extend by such improvements the time scale only by a factor 2, this would be far beyond the capacities of exact diagonalization for a very, very long time.

[3]Here the structure of the transfer matrix in the novel approach has several advantages.

Chapter 8

Conclusion

The present thesis deals with the transfer-matrix approach to calculate thermodynamics and dynamics of one-dimensional quantum systems. The method is based on a Trotter-Suzuki mapping [13, 14, 15] of the quantum chain onto a two-dimensional classical model. For the classical model a column-to-column transfer matrix, the so called quantum transfer matrix (QTM), is formulated which evolves along the spatial direction. The fundamental advantage of the transfer-matrix approach is that the thermodynamic limit, i.e. chain length $L \to \infty$, can be performed exactly. Thermodynamic potentials, expectation values of local operators and static as well as dynamic correlation functions can be calculated in the exact thermodynamic limit solely from the largest eigenvalue and the corresponding left and right eigenvectors of a suitable QTM. To calculate correlation lengths, the next-leading eigenvalues of the QTM are needed additionally. The method is applicable for every one-dimensional system with short range interactions. Usually a Hamiltonian with nearest neighbour interactions is decomposed into two parts, where one part contains the interactions starting on an even site, the other the interactions starting on an odd site. This decomposition has been proposed by Suzuki [15] and yields a classical model with checkerboard structure. Almost all quantum Monte Carlo algorithms are based on it. If a QTM is formulated for this classical system, it has a repeat length of 2 due to the checkerboard structure and is therefore unnecessarily wide. The consequence are several disadvantages. For example, it is not possible to determine uniquely the wavevector describing the oscillations of a correlation function in the asymptotic limit solely from the leading and next-leading eigenvalue of the QTM. Besides the calculation of correlation functions itself is complicated because even and odd as well as distance 0 and 1 have to be treated separately. In this thesis an alternative mapping of the quantum chain onto a two-dimensional classical model has been proposed, which allows the definition of a QTM with repeat length 1. At first sight the structure of the novel QTM seems to be more complicated because it has alternating rows and additional lattice points in a mathematical auxiliary space. However, this is no disadvantage in practical calculations. On the contrary, the problems of the checkerboard QTM listed above can be solved within this new approach. Additionally, the novel QTM has the further advantage in numerical calculations that less computer memory is needed to store it.

Although one only needs to determine the largest eigenvalue of the QTM to calculate all thermodynamic quantities, this is possible analytically only for Bethe ansatz integrable models [12]. In all other cases numerical methods have to be applied. A very powerful approach to calculate ground-state properties of one-dimensional quantum systems is the density matrix renormalization group (DMRG) invented by White in 1992 [11]. The fundamental idea is to represent approximately the very large Hilbert space of a chain with

finite length L, which is typically of the order $L \sim 100$, by a small number of states typically also of order 100. A density matrix is used to choose the optimal states in an iterative procedure. This concept has been extended successfully to finite temperatures by applying the iterative DMRG scheme to the checkerboard QTM discussed before [16, 17, 18]. The imaginary-time (temperature) direction is treated numerically, while the exact thermodynamic limit is performed in spatial direction by taking only the largest eigenvalue of the QTM into account. Note that an implementation is generally more complicated than in the zero-temperature DMRG due to the tensor structure of the non-symmetric transfer matrix and due to a non-symmetric generalized density matrix. This so called transfer-matrix DMRG (TMRG) often exceeds other numerical techniques with respect to accuracy and accessible temperature range. Compared especially to QMC it has the advantage of acting directly in the thermodynamic limit and it never suffers under the negative sign problem restricting QMC calculations for fermionic systems often to relatively high temperatures and small system sizes. In this thesis it has been explained how the numerical TMRG technique can be effectively used for the checkerboard and for the novel QTM. By modifying the known algorithm [26] it was possible to take advantage of the different structure of the novel transfer matrix and to reduce the amount of computer space needed by a factor $\sim S^2$, where S is the dimension of the local Hilbert space. This allows it to perform TMRG calculations even for systems with a large number of local degrees of freedom, e.g. high spin systems, models with spin and charge degrees of freedom or spin-orbital models, on a standard workstation or even on a PC.

To show how powerful both algorithms are, we have calculated the free energy of the spin-1/2 XXZ-model at the free fermion point $\Delta = 0$ and at $\Delta = 0.5$ and have compared the numerical with exact results. Thereby we have shown that both algorithms yield results with a comparable accuracy over a wide temperature range. We have identified two sources of numerical errors. First, there is the error due to the Trotter-Suzuki mapping with a finite Trotter parameter ϵ. We have investigated this error analytically and numerically for both approaches and have found that it is always $\sim \epsilon^2$ and is dominating at high and intermediate temperatures. Second, there is the error due to the truncation of the Hilbert space. At low temperatures, when many RG steps have been performed, this error is dominating and depending on the number of retained states. However, no clear scaling is detectable. Additionally we have calculated the longitudinal spin-spin correlation length and have compared again with the exact results. Thereby we have settled that the TMRG algorithm is appropriate to calculate also correlation lengths accurately down to low temperatures. The direct calculation of static correlation functions at the free fermion point has shown that TMRG is able to capture the behaviour not only in the asymptotic limit but also at short distances.

Both TMRG algorithms have been applied for the first investigation of thermodynamics of the one-dimensional t-J model in the complete $(J/t, \mu)$-parameter space.[1] Quantities like specific heat, susceptibility, compressibility, particle number and various correlation lengths have been calculated. Based on these results, a phase diagram consisting of a Tomonaga-Luttinger liquid (TLL) phase for small J/t and a phase separated state for

[1] A grandcanonical description has been used with a chemical potential μ.

J/t large has been confirmed. Close to the phase separated state an additional spin-gap (Luther-Emery) phase was found at low densities. These findings are in agreement with predictions in other studies [34, 35, 40, 41, 42], but here the existence of the spin-gap phase has been proved for the first time without using any assumptions about the ground state or the low energy effective theory. We have started with the calculation of several thermodynamic quantities at the supersymmetric point $J/t = 2$, where the t-J model is exactly solvable by Bethe ansatz [36, 39, 37, 38]. By a detailed comparison with the exact results and predictions from conformal field theory (CFT) we have shown that the TMRG algorithm yields reliable results down to $T/t \sim 0.01$. In particular, we have concentrated on the calculation of correlation lengths to study the crossover from the non-universal high-T lattice into the quantum critical regime ($T \ll t$). Characteristic for the quantum critical regime is a $1/T$ divergence of the correlation lengths leading to an algebraic decay of correlations at $T = 0$. We have extended the results for the exponents of these algebraically decaying correlation functions, obtained by a combination of CFT and Bethe ansatz [37, 38], to small finite temperatures by a mapping of the complex plane onto a strip of width $1/T$ with periodic boundary conditions. This allows us to calculate the parameter of the $1/T$ divergence for each correlation length analytically and the results have been compared in detail with the numerics. In principle, a good agreement was found, but it was important to take also logarithmic corrections [45] into account. At elevated temperatures the analytical CFT results are not applicable[2] and the numerics shows that several crossovers between correlation lengths with different wavevectors occur which are driven by temperature. These observations are relevant and experimentally accessible by measurements of the structure factor, because the leading correlation length gives the sharpest peak and indicates the leading instability towards the onset of long range order. Hence, a crossover in the leading correlation lengths indicates a change of the nature of the long range order. We have investigated also $J/t = 0.35$, a value often considered physically relevant. We have shown that the t-J model at this point behaves very similar to the supersymmetric t-J model, in particular, it belongs to the same universality class of TLL. For J/t large enough we have found phase separation. However, in the grandcanonical description this has the meaning of phase coexistence only at one special chemical potential μ. If μ is smaller (larger), we find an empty (half-filled) state for $T = 0$. The existence of a spin-gap phase close to the phase separated state was proved by a direct calculation of the spin susceptibility, which shows an activated behaviour. Additional evidence was given by a calculation of spin and charge correlation lengths. Finally, we have studied the effect of an Ising-like anisotropy and have found that singlet pair correlations are enhanced and that the expected long range spin order is hidden away from the half-filled case.

The second main topic of this thesis has been the investigation of spin-orbital models. In addition to the usual spin degrees of freedom in a Mott insulator, low-lying electronic states (termed "orbitals") exist in many transition metal oxides [21]. Due to the unquenched orbital degrees of freedom a large number of nearly degenerate many-body states is accessible ("orbital frustration") and a microscopic description of such a system

[2] In fact, the temperature region where CFT is valid is rather small.

has to treat spins and orbitals on an equal footing. The sign and magnitude of the spin-spin interactions is determined by the orbital occupation resulting in strong spin-orbital correlations and leading to new interesting magnetic phenomena [51, 53, 54]. In this thesis we have presented the first study of thermodynamics of a realistic one-dimensional spin-orbital model derived in Ref. [22] with spin $S = 1$ and two degenerated orbitals described by a pseudospin $\tau = 1/2$. $SU(2)$ symmetry breaking in the orbital sector due to the Hund's rule splitting of the excited multiplet has been taken into account. We have discussed the relevance of this model for the C-type phase of YVO_3 in detail but we want to emphasize again that the one-dimensional model is also interesting on its own. The phase diagram of the model exhibits two phases. At small Hund's coupling J_H we have discovered dimerization in a pure electronic system solely due to a dynamical spin-orbital coupling. Above a critical value $J_H^c/U \sim 0.11$, a uniform ferromagnetic state is stabilized at zero temperature, but surprisingly we have again found dimerization of the ferrochain at finite temperature, which occurs due to the large entropy released by dimer states. These findings have been settled by a calculation of nearest neighbour spin and orbital correlations, the spin and orbital susceptibility, the specific heat and most important by the calculation of correlation lengths. The novel TMRG algorithm has turned out to be extremely useful here because the local basis for this model contains $S = 6$ states and the factor $\sim S^2$ less computer memory needed within the new approach makes calculations on a usual workstation possible. We have also investigated the effect of spin-orbit coupling and have found that it leaves the entropy driven dimerization at $J_H > J_H^c$ almost unaffected but introduces an easy-plane anisotropy in analogy to a spin-flop transition. We believe that the one-dimensional model can explain semiquantitatively many of the unusual features observed in the C-phase of YVO_3 [71, 61, 58]. We have argued that the orbital physics is essentially one-dimensional, but this is not true for the spin sector where the spin-coupling constants are of the same order in all directions. We have therefore investigated the effect of interchain coupling on a mean-field level and have found that the essential physical property, namely the entropy driven dimerization at finite temperature for $\eta > \eta_c$, is almost unaffected for realistic molecular fields. The microscopic one-dimensional model is therefore really capable of explaining the experimentally observed features in the high-temperature phase of YVO_3 as for example the stability of the C-phase itself, the optical-acoustic splitting of the magnon branches along the c-axis, the small ordered magnetic moment, the easy-plane anisotropy and the canting of the spins away from the ab-plane.

Another spin-orbital model with $S = 1/2$ and an orbital pseudospin $\tau = 1/2$ which exhibits an $SU(4)$ symmetry has already been studied intensively before [66,81,82,68,24,83]. Even thermodynamic properties have been investigated by the QMC loop algorithm [68]. There are several reasons why we have regarded this model again. First, the model is solvable by Bethe ansatz and although thermodynamics has not been obtained yet from Bethe ansatz, it provides the possibility to test the accuracy of the numerically calculated ground-state energy and spin-wave velocity. We have found an excellent agreement showing that the TMRG algorithm works perfectly even for spin-orbital models with a relatively large number of local basis states. Second, much about this model is known from CFT [23, 24] and by extending these results to finite temperatures similar to the

study of the t-J model, an analytical and numerical investigation of the behaviour of correlation lengths at finite temperatures was possible. Again it was important to incorporate also logarithmic corrections. This connection to CFT has not been recognized in detail in Ref. [68]. Renormalization group (RG) and CFT calculations in Ref. [24] predict that certain perturbations of the $SU(4)$ symmetric model are only marginal and leave the critical properties of the model unchanged up to a rescaling of the spin and orbital velocities. This is interesting from a theoretical point of view, because it resembles a Tomonaga-Luttinger liquid where spin and charge velocity are in general different, a phenomenon called spin-charge separation. In analogy, the $SU(4)$ spin-orbital model with a marginal perturbation shows a kind of spin-orbital separation. By calculating again several correlation lengths we have estimated the different velocities and have shown that the RG predictions hold. However, it has turned out that the reconstruction of $SU(4)$ up to the rescaling of velocities is restricted to very low temperatures. In all investigated spin-orbital models we have found an intrinsic tendency towards dimerization, which is present at finite temperature even if the ground state is not dimerized. In the future it might be interesting to study the $SU(4)$ model in the hole doped case, i.e. a generalized t-J model with additional orbital degrees of freedom. From preliminary numerical calculations we expect that physics at low temperatures is described by a generalized CFT with three different velocities for spin, orbital and charge excitations so that the model would present a generalized Tomonaga-Luttinger liquid. Additionally, the preliminary calculations suggest that relatively strong pair correlations are present and that singlet or triplet pair could dominate depending on parameters. This might be an interesting topic within the research on superconductivity in low-dimensional systems.

In the last chapter we have introduced a new promising approach to calculate dynamic correlations in one-dimensional systems at non-zero temperature. The method is based on two independent Trotter-Suzuki decompositions, where one is in temperature (imaginary time) and the other in real time. This eludes the problems connected with the Matsubara formalism in numerical calculations: Due to unpreventable numerical errors the continuation of imaginary-time correlations to real times is an exponentially ill-posed problem leading to unreliable results. However, hitherto alternatives have not been known and the interest in dynamics is so strong that methods giving the "most probable" analytic continuation are widely used. To test our approach we have calculated the spin autocorrelation in the XXZ-model at infinite temperature. Although the XXZ-model is integrable, exact results for this quantity are only known at the free fermion point. The question about the long-time behaviour at any other generic point is still unsolved and presents a serious problem on its own. In a first naive implementation we have shown that our real-time transfer matrix approach is working in principle. At the free fermion point we have compared the numerics with the exact result as well as with exact diagonalization data from Ref. [91]. The accuracy of the data is satisfying and a time scale is reached which is comparable with the best exact diagonalization data. However, we expect that the applicability of the method can be extended by the discussed improvements and we hope that at least the problem of the long-time behaviour of autocorrelation functions in the XXZ-model at infinite temperature can be solved with this novel approach in the near future.

Appendix A

Corrections due to the Trotter-Suzuki Mapping

For two operators A, B and a parameter ϵ the Zassenhaus formula [14] yields

$$\mathrm{e}^{\epsilon(A+B)} = \mathrm{e}^{\epsilon A}\mathrm{e}^{\epsilon B}\mathrm{e}^{\epsilon^2 C_2}\mathrm{e}^{\epsilon^3 C_3}\cdots \tag{A.1}$$

with coefficients C_n which are defined recursively

$$C_n = \frac{1}{n!}\left[\frac{\partial^n}{\partial\epsilon^n}\left(\mathrm{e}^{-\epsilon^{n-1}C_{n-1}}\cdots\mathrm{e}^{-\epsilon^2 C_2}\mathrm{e}^{-\epsilon B}\mathrm{e}^{-\epsilon A}\mathrm{e}^{\epsilon(A+B)}\right)\right]_{\epsilon=0} \tag{A.2}$$

and therefore especially

$$C_2 = \frac{1}{2}[B,A] \qquad , \qquad C_3 = \frac{1}{6}[C_2, A+2B]\ . \tag{A.3}$$

In the traditional Trotter-Suzuki mapping the Hamiltonian is decomposed into a part containing only the interactions starting on an even site and another part which contains the interactions starting on an odd site (see Eq. (2.18)). Therefore each part is a sum of *commuting terms*. Following Eq. (A.1) we find

$$\mathrm{e}^{-\epsilon H} = \mathrm{e}^{-\epsilon(H_o+H_e)} = \mathrm{e}^{-\epsilon H_o}\mathrm{e}^{-\epsilon H_e}\mathrm{e}^{\epsilon^2/2[H_e,H_o]}\cdots = \mathrm{e}^{-\epsilon H_o}\mathrm{e}^{-\epsilon H_e} + \mathcal{O}(\epsilon^2) \tag{A.4}$$

so that we expect a correction $\sim \mathcal{O}(\epsilon)$, if we approximate the partition function $Z = \mathrm{Tr}\{\exp(-\beta H)\}$ by

$$\tilde{Z} = \mathrm{Tr}\left(\mathrm{e}^{-\epsilon H_o}\mathrm{e}^{-\epsilon H_e}\right)^M \tag{A.5}$$

with $\epsilon = \beta/M$. However, due to the cyclic invariance of the trace

$$\tilde{Z} = \mathrm{Tr}\left(\mathrm{e}^{-\epsilon H_o/2}\mathrm{e}^{-\epsilon H_e}\mathrm{e}^{-\epsilon H_o/2}\right)^M \tag{A.6}$$

it turns out that the correction is in fact only of order $\mathcal{O}(\epsilon^2)$, because

$$\begin{aligned}\mathrm{e}^{-\epsilon H} &= \mathrm{e}^{-\epsilon[H_o/2+(H_e+H_o/2)]} = \mathrm{e}^{-\epsilon H_o/2}\,\mathrm{e}^{-\epsilon H_e}\,\mathrm{e}^{-\epsilon H_o/2}\,\mathrm{e}^{\epsilon^2[H_o,H_e]/4}\,\mathrm{e}^{\epsilon^2[H_e,H_o]/4} + \mathcal{O}(\epsilon^3)\\ &= \mathrm{e}^{-\epsilon H_o/2}\,\mathrm{e}^{-\epsilon H_e}\,\mathrm{e}^{-\epsilon H_o/2} + \mathcal{O}(\epsilon^3)\ .\end{aligned} \tag{A.7}$$

H_o, H_e are sums of commuting terms, so we finally derive [14, 15]

$$Z = \mathrm{Tr}\left(\prod_{i=\mathrm{odd}}\mathrm{e}^{-\epsilon h_{i,i+1}}\prod_{i=\mathrm{even}}\mathrm{e}^{-\epsilon h_{i,i+1}}\right)^M\left(1+\mathcal{O}(\epsilon^2)\right)\ . \tag{A.8}$$

As a direct consequence, the error in the free energy due to the mapping is also $\mathcal{O}(\epsilon^2)$.

The situation is more involved in the alternative mapping and we want to consider the Trotter mapping therefore more generally [94]. Every approximant for the density matrix ρ can be displayed as

$$\rho_{\text{approx}} = \mathrm{e}^{-\beta(H+\epsilon C_2+\epsilon^2\tilde{C}_3)} + \mathcal{O}(\epsilon^3) \tag{A.9}$$

with suitably defined operators C_2 and $\tilde{C}_3$. For example, in the traditional mapping $\exp(-\epsilon H_o)\exp(-\epsilon H_e)$ is used as approximant and we find by applying the Zassenhaus formula in the opposite direction

$$\mathrm{e}^{-\epsilon H_o}\mathrm{e}^{-\epsilon H_e} = \mathrm{e}^{-\epsilon(H+\epsilon C_2+\epsilon^2\tilde{C}_3)} + \mathcal{O}(\epsilon^4)\ ,\ \text{where}\ \ \tilde{C}_3 = C_3 - \frac{1}{2}[C_2, H] \tag{A.10}$$

and C_2 and C_3 are defined in Eq. (A.3) with $A = H_o$ and $B = H_e$.

Next we want to expand Eq. (A.9) in orders of ϵ by using the ordering label technique, i.e. $AB = A_1B_0 = B_0A_1$ with the rule that the operator with higher index acts later. In this way we can express Eq. (A.9) as

$$\begin{aligned} & \exp\left\{-\beta\int_0^1 H_s\,ds\right\}\exp\left\{-\beta\epsilon\int_0^1 C_{2,s}\,ds\right\}\exp\left\{-\beta\epsilon^2\int_0^1 \tilde{C}_{3,s}\,ds\right\} \\ = \ & \exp\left\{-\beta\int_0^1 H_s\,ds\right\}\left(1-\beta\epsilon\int_0^1 C_{2,s}\,ds + \beta^2\frac{\epsilon^2}{2}\int_0^1\int_0^1 ds\,ds'\,C_{2,s}C_{2,s'}\right) \\ & \left(1-\beta\epsilon^2\int_0^1 \tilde{C}_{3,s}\,ds\right) + \mathcal{O}(\epsilon^3)\ . \end{aligned} \tag{A.11}$$

In zeroth order there is only one operator and therefore H_s is independent of s leading to $\exp(-\beta H)$. In first order we find

$$\begin{aligned} & \exp\left\{-\beta\int_0^1 H_s\,ds\right\}\left\{-\beta\epsilon\int_0^1 C_{2,s'}\,ds'\right\} \\ = \ & -\beta\epsilon\int_0^1 ds'\exp\left\{-\beta\int_0^1 H_s\,ds\right\}C_{2,s'} \\ = \ & -\beta\epsilon\int_0^1 ds'\exp\left\{-\beta\int_{s'}^1 H_s\,ds\right\}C_{2,s'}\exp\left\{-\beta\int_0^{s'} H_s\,ds\right\} \\ = \ & -\beta\epsilon\int_0^1 ds'\exp\left\{-\beta(1-s')H\right\}C_2\exp\left\{-\beta s'H\right\} \\ = \ & -\epsilon\int_0^\beta d\tau\,\mathrm{e}^{-\beta H}\,\mathrm{e}^{\tau H}C_2\,\mathrm{e}^{-\tau H} = -\epsilon\int_0^\beta d\tau\,\mathrm{e}^{-\beta H}\,C_2(\tau) \end{aligned} \tag{A.12}$$

where the definition $C_2(\tau) = \exp\{\tau H\}C_2\exp\{-\tau H\}$ is used in the last line. Taking also the second order into account we finally derive

$$\begin{aligned} \mathrm{e}^{-\beta(H+\epsilon C_2+\epsilon^2\tilde{C}_3)} \ = \ & \mathrm{e}^{-\beta H}\left[1-\epsilon\int_0^\beta C_2(\tau)\,d\tau\right. \\ & \left. + \ \epsilon^2\left(\int_0^\beta\int_0^\tau C_2(\tau)C_2(\tau')\,d\tau\,d\tau' - \int_0^\beta \tilde{C}_3(\tau)\,d\tau\right)\right] + \mathcal{O}(\epsilon^3)\ . \end{aligned} \tag{A.13}$$

The approximated partition function is therefore given by

$$\tilde{Z} = Z\left(1 - \epsilon\left\langle \int_0^\beta C_2(\tau)d\tau \right\rangle + \mathcal{O}(\epsilon^2)\right) \tag{A.14}$$

and only has $\mathcal{O}(\epsilon^2)$ corrections if the first order term vanishes. In the traditional mapping we have found

$$C_2 \sim [H_e, H_o] = \sum_i (-1)^i [h_{i-1,i}, h_{i,i+1}] \tag{A.15}$$

and it is easy to show that

$$C_2 \sim \sum_i [h_{i-1,i}, h_{i,i+1}] \tag{A.16}$$

holds also in the new approach where we use

$$T_R \prod_i \exp(-\epsilon h_{i,i+1}) T_L \prod_i \exp(-\epsilon h_{i,i+1}) \tag{A.17}$$

as approximant. Because $h_{i,i+1}$ is a Hermitian operator, $C_2 \sim [h_{i-1,i}, h_{i,i+1}]$ is anti-Hermitian. It is now easy to prove that $A := \exp(-\beta H)\int_0^\beta C_2(\tau)d\tau$ is also anti-Hermitian. In the numerical calculations we always use a real representation of the local Hamiltonian and therefore the trace of the operator A vanishes

$$\mathrm{Tr}\, A = \mathrm{Tr}\,(-A^\dagger) = \mathrm{Tr}\,(-A) = -\mathrm{Tr}\, A = 0\ . \tag{A.18}$$

Therefore we find for both Trotter-Suzuki decompositions that the approximated partition functions and free energies only have corrections $\sim \mathcal{O}(\epsilon^2)$ due to the mapping. Quite generally we have shown that in every Trotter-Suzuki like decomposition of the partition function the error is only of the order $\mathcal{O}(\epsilon^2)$ if C_2 is an anti-Hermitian operator and a real representation is used.

Appendix B

Free Spinless Fermions

Here we want to consider the simplest fermionic system in 1D, the model of free spinless fermions on a lattice. For this model it is possible to calculate the free energy, correlation lengths and also correlation functions analytically. The Hamiltonian in real space is given by

$$H = -\tilde{t} \sum_r \left(c_r^\dagger c_{r+1} + c_{r+1}^\dagger c_r \right) \tag{B.1}$$

with a hopping amplitude $\tilde{t}$. By applying a Fourier transformation $c_r = \sum_q \exp(\mathrm{i}qr) c_q$ we receive

$$H = -\tilde{t} \sum_q \cos(q) c_q^\dagger c_q = \sum_q \epsilon_q n_q \tag{B.2}$$

where we have set $2\tilde{t} \to \tilde{t}$, $\epsilon_q = -\tilde{t}\cos(q)$ and $n_q = c_q^\dagger c_q$.
For the corresponding partition function we find

$$Z = \sum_{\{n_q\}} \prod_q \mathrm{e}^{-\beta \epsilon_q n_q} = \prod_q \sum_{n_q=0}^{1} \mathrm{e}^{-\beta \epsilon_q n_q} = \prod_q \left(1 + \mathrm{e}^{-\beta\epsilon_q}\right) \ . \tag{B.3}$$

The free energy $f = -T \ln Z$ can be calculated by evaluating the integral

$$f = -\frac{T}{2\pi} \int_{-\pi}^{\pi} dq \, \ln\left(1 + \mathrm{e}^{-\beta\epsilon_q}\right) \tag{B.4}$$

and the ground-state energy is given by filling up the Fermi sea

$$e_0 = \frac{1}{2\pi} \int_{-\pi/2}^{\pi/2} dq \, \epsilon_q = -\frac{\tilde{t}}{\pi} \sim -0.3183 \, \tilde{t} \ . \tag{B.5}$$

Next we want to calculate the density-density correlation function $\langle \rho_r(t) \rho_{r'}(0) \rangle$ with $\rho_r(t) = c_r^\dagger(t) c_r(t)$. In momentum space the density operator is given by

$$\rho_q(t) = \frac{1}{V} \sum_k c_{k+q/2}^\dagger(t) c_{k-q/2}(t) \ . \tag{B.6}$$

By applying Wick's theorem, the density-density correlation function separates into two-point functions

$$\left\langle c_r^\dagger(t) c_r(t) c_0^\dagger(0) c_0(0) \right\rangle = \frac{1}{V^2} \left(\sum_k n(\epsilon_k) \right)^2 \tag{B.7}$$

$$+ \quad \frac{1}{V^2} \sum_{k,q} \mathrm{e}^{\mathrm{i}qr} \left\langle c_{k-\frac{q}{2}}^\dagger(t) c_{k-\frac{q}{2}}(0) \right\rangle \left\langle c_{k+\frac{q}{2}}(t) c_{k+\frac{q}{2}}^\dagger(0) \right\rangle$$

where $n(\epsilon_k)$ is the Fermi function. By using the Matsubara formalism, inserting the known results for the electrons Green's function and then going back to real time, this is easily transformed into

$$\left\langle c_r^\dagger(t)c_r(t)c_0^\dagger(0)c_0(0)\right\rangle = n^2 + \frac{1}{V^2}\sum_{q,k} \mathrm{e}^{\mathrm{i}qr}\frac{\mathrm{e}^{\mathrm{i}(\epsilon_{k-\frac{q}{2}}-\epsilon_{k+\frac{q}{2}})t}}{(\mathrm{e}^{\beta\epsilon_{k-\frac{q}{2}}}+1)(\mathrm{e}^{-\beta\epsilon_{k+\frac{q}{2}}}+1)}\,. \tag{B.8}$$

Regarding only the connected part and transforming to Matsubara frequencies we get in the free fermion case

$$G(r,z=0) = \frac{1}{(2\pi)^2}\iint dq\,dk\,\frac{n(\epsilon_{k+\frac{q}{2}})-n(\epsilon_{k-\frac{q}{2}})}{\epsilon_{k-\frac{q}{2}}-\epsilon_{k+\frac{q}{2}}}\cos(qr) \tag{B.9}$$

for the static density-density correlation function as defined in Eq. (2.36). Returning to Eq. (B.8) and setting $t=0$ we find

$$\left\langle c_r^\dagger c_r c_0^\dagger c_0\right\rangle = \left[\frac{1}{2\pi}\int_{-\pi}^{\pi} dq \frac{\mathrm{e}^{\mathrm{i}qr}}{\mathrm{e}^{-\beta\cos(q)}+1}\right]\times\left[\frac{1}{2\pi}\int_{-\pi}^{\pi} dk \frac{\mathrm{e}^{-\mathrm{i}kr}}{\mathrm{e}^{\beta\cos(k)}+1}\right]\,. \tag{B.10}$$

Now we can evaluate these integrals in principle by closing the integration path in the upper (lower) half plane and using Cauchy's formula. The poles are at the points

$$q,k = \pm\frac{\pi}{2} \pm \mathrm{i}\,\mathrm{arcsinh}\left((2n+1)\frac{\pi}{\beta}\right) \tag{B.11}$$

and thus, the dominant contribution is

$$\left\langle c_r^\dagger c_r c_0^\dagger c_0\right\rangle \sim M\mathrm{e}^{-r/\xi}(1-\cos(\pi r)) \tag{B.12a}$$

where the matrixelement is given by

$$M = \frac{2}{\pi^2+\beta^2} \tag{B.12b}$$

and the CL by

$$\xi = \frac{1}{2\,\mathrm{arcsinh}(\pi/\beta)}\,. \tag{B.12c}$$

The density-density autocorrelation function at infinite temperature can be calculated from Eq. (B.8) by setting $r=0$ and $\beta=0$. For infinite temperature the Fermi function reduces to $n(\epsilon_k)=1/2$ and we find

$$\begin{aligned}\langle\rho_0(t)\rho_0(0)\rangle &= \frac{1}{4}+\frac{1}{4V^2}\sum_{q,k}\mathrm{e}^{\mathrm{i}(\epsilon_{k-\frac{q}{2}}-\epsilon_{k+\frac{q}{2}})t} = \frac{1}{4}+\left(\frac{1}{2V}\sum_q \mathrm{e}^{\mathrm{i}\epsilon_q t}\right)\left(\frac{1}{2V}\sum_q \mathrm{e}^{-\mathrm{i}\epsilon_q t}\right)\\ &= \frac{1}{4}+\frac{1}{16\pi^2}\Bigg(\underbrace{\int_{-\pi}^{\pi} dq\,\cos(\tilde{t}\cos(q)t)}_{2\pi J_0(\tilde{t}t)}\Bigg)^2 = \frac{1}{4}+\frac{1}{4}\left[J_0(\tilde{t}t)\right]^2\end{aligned} \tag{B.13}$$

with J_0 being the Bessel function of order zero.

Bibliography

[1] for a recent review see the article collection edited by I. S. Osborne, Science **288**, 461–482 (2000).

[2] M. Imada, A. Fujimori, and Y. Tokura, Rev. Mod. Phys. **70**, 1039 (1998).

[3] J. A. Bednorz and K. A. Müller, Z. Phys. B **64**, 189 (1986).

[4] P. W. Anderson, Science **235**, 1196 (1987).

[5] N. D. Mermin and H. Wagner, Phys. Rev. Lett. **17**, 1133 (1966).

[6] P. C. Hohenberg, Phys. Rev. **158**, 383 (1967).

[7] S. Sachdev, *Quantum Phase Transitions*, Cambridge University Press, (Cambridge 1999).

[8] R. J. Baxter, *Exactly Solved Models in Statistical Mechanics*, Academic Press, (London 1982).

[9] K. G. Wilson and J. Kogut, Phys. Reports **12**, 75 (1974).

[10] K. G. Wilson, Rev. Mod. Phys. **47**, 773 (1975).

[11] S. R. White, Phys. Rev. Lett. **69**, 2863 (1992).

[12] A. Klümper, Z. Phys. B **91**, 507 (1993).

[13] H. F. Trotter, Proc. Amer. Math. Soc. **10**, 545 (1959).

[14] M. Suzuki, Commun. Math. Phys. **51**, 183 (1976).

[15] M. Suzuki, Phys. Rev. B **31**, 2957 (1985).

[16] R. J. Bursill, T. Xiang, and G. A. Gehring, J. Phys. Cond. Mat. **8**, L583 (1996).

[17] X. Wang and T. Xiang, Phys. Rev. B **56**, 5061 (1997).

[18] N. Shibata, J. Phys. Soc. Jpn. **66**, 2221 (1997).

[19] for a review see: H. J. Schulz, G. Cuniberti, and P. Pieri, cond-mat/9807366v2 (1998).

[20] U. Ammerahl, B. Büchner, L. Colonescu, R. Gross, and A. Revcolevschi, Phys. Rev. B **62**, 8630 (2000).

[21] Y. Tokura and N. Nagaosa, Science **288**, 462 (2000).

[22] G. Khaliullin, P. Horsch, and A. M. Oleś, Phys. Rev. Lett. **86**, 3879 (2001).

[23] I. Affleck, Nucl. Phys. B **265**, 409 (1986).

[24] C. Itoi, S. Qin, and I. Affleck, Phys. Rev. B **61**, 6747 (2000).

[25] E. Ising, Z. Phys. **31**, 253 (1925).

[26] I.Peschel, X. Wang, M. Kaulke, and K. Hallberg, editors, *Density-Matrix Renormalization, Lecture Notes in Physics*, volume 528, Springer, (Berlin 1999). and references therein.

[27] J. Sirker and A. Klümper, Europhys. Lett. **60**, 262 (2002).

[28] S. Itoh, H. Tanaka, and M. J. Bull, J. Phys. Soc. Jpn. **71**, 1148 (2002).

[29] R. Raupach, *On the spin-Peierls phase transition of frustrated Heisenberg chains*, PhD thesis, Universität zu Köln, (2000).

[30] *see: http://www.caam.rice.edu/software/ARPACK/.*

[31] *see: http://www.netlib.org/lapack/.*

[32] B. Ammon, M. Troyer, T. M. Rice, and N. Shibata, Phys. Rev. Lett. **82**, 3855 (1999).

[33] A. Klümper, J. R. R. Martinez, C. Scheeren, and M. Shiroishi, J. Stat. Phys. **102**, 937 (2001).

[34] M. Ogata, M. U. Luchini, S. Sorella, and F. F. Assaad, Phys. Rev. Lett. **66**, 2388 (1991).

[35] C. S. Hellberg and E. J. Mele, Phys. Rev. Lett. **67**, 2080 (1991).

[36] P. A. Bares and G. Blatter, Phys. Rev. Lett. **64**, 2567 (1990).

[37] N. Kawakami and S. K. Yang, Phys. Rev. Lett. **65**, 2309 (1990).

[38] N. Kawakami and S. K. Yang, J. Phys. Cond. Mat. **3**, 5983 (1991).

[39] G. Jüttner, A. Klümper, and J. Suzuki, Nucl. Phys. B **487**, 650 (1997).

[40] Y. C. Chen and T. K. Lee, Phys. Rev. B **54**, 9062 (1996).

[41] K. Kobayashi, C. Ohe, and K. Iguchi, Phys. Rev. B **54**, 13129 (1996).

[42] M. Nakamura, K. Nomura, and A. Kitazawa, Phys. Rev. Lett. **79**, 3214 (1997).

[43] A. Okiji and S. Suga, Physica B **237**, 81 (1997).

[44] H. Frahm and V. E. Korepin, Phys. Rev. B **42**, 10553 (1990).

[45] T. Giamarchi and H. J. Schulz, Phys. Rev. B **39**, 4620 (1989).

[46] K. Sakai and A. Klümper, J. Phys. A **34**, 8015 (2001).

[47] R. Z. Bariev, A. Klümper, A. Schadschneider, and J. Zittartz, Z. Phys. B **96**, 395 (1995).

[48] T. Pruschke and H. Shiba, Phys. Rev. B **44**, 205 (1991).

[49] P. W. Anderson, cond-mat/0201431v1 (2002).

[50] K. I. Kugel and D. I. Khomskii, Sov. Phys. Usp. **25**, 231 (1982).

[51] Y. Tokura, editor, *Colossal Magnetoresistive Oxides*, Gordon and Breach Science, (New York 2000). and references therein.

[52] G. Khaliullin and S. Maekawa, Phys. Rev. Lett. **85**, 3950 (2000).

[53] B. Keimer, D. Casa, A. Ivanov, J. W. Lynn, M. v. Zimmermann, J. P. Hill, D. Gibbs, Y. Taguchi, and Y. Tokura, Phys. Rev. Lett. **85**, 3946 (2000).

[54] Y. Ren, T. T. M. Palstra, D. I. Khomskii, A. A. Nugroho, A. A. Menovsky, and G. A. Sawatzky, Phys. Rev. B **62**, 6577 (2000).

[55] Y. Ren, T. T. M. Palstra, D. I. Khomskii, E. Pellegrin, A. A. Nugroho, A. A. Menovsky, and G. A. Sawatzky, Nature **396**, 441 (1998).

[56] M. Noguchi, A. Nakazawa, S. Oka, T. Arima, Y. Wakabayashi, H. Nakao, and Y. Murakami, Phys. Rev. B **62**, R9271 (2000).

[57] J. Sirker and G. Khaliullin, submitted to Phys. Rev. Lett. (2002).

[58] C. Ulrich, G. Khaliullin, J. Sirker, M. Reehuis, M. Ohl, S. Miyasaka, Y. Tokura, and B. Keimer, to be resubmitted (2002).

[59] M. Tinkham, *Group theory and quantum mechanics*, McGraw-Hill, (New York 1964).

[60] A. Abragam and B. Bleaney, *Electron Paramagnetic Resonance of Transition Ions*, Clarendon Press, (Oxford 1970).

[61] G. R. Blake, T. T. M. Palstra, Y. Ren, A. A. Nugroho, and A. A. Menovsky, Phys. Rev. Lett. **87**, 245501 (2001).

[62] G. Khaliullin and S. Okamoto, Phys. Rev. Lett. **89**, 167201 (2002).

[63] C. Ulrich, G. Khaliullin, S. Okamoto, M. Reehuis, A. Ivanov, H. He, Y. Taguchi, Y. Tokura, and B. Keimer, Phys. Rev. Lett. **89**, 167202 (2002).

[64] H. Sawada and K. Terakura, Phys. Rev. B **58**, 6831 (1998).

[65] T. Mizokawa and A. Fujimori, Phys. Rev. B **54**, 5368 (1996).

[66] Y. Q. Li, M. Ma, D. N. Shi, and F. C. Zhang, Phys. Rev. Lett. **81**, 3527 (1998).

[67] B. Sutherland, Phys. Rev. B **12**, 3795 (1975).

[68] B. Frischmuth, F. Mila, and M. Troyer, Phys. Rev. Lett. **82**, 835 (1999).

[69] J. B. Goodenough, Phys. Rev. **100**, 564 (1955).

[70] J. Kanamori, J. Phys. Chem. Solids **10**, 87 (1959).

[71] H. Kawano, H. Yoshizawa, and Y. Ueda, J. Phys. Soc. Jpn. **63**, 2857 (1994).

[72] H. Sawada, N. Hamada, K. Terakura, and T. Asada, Phys. Rev. B **53**, 12742 (1996).

[73] T. Mizokawa, D. I. Khomskii, and G. A. Sawatzky, Phys. Rev. B **60**, 7309 (1999).

[74] F. Mila, R. Shiina, F. C. Zhang, A. Joshi, M. Ma, V. Anisimov, and T. M. Rice, Phys. Rev. Lett. **85**, 1714 (2000).

[75] S. Q. Shen, X. C. Xie, and F. C. Zhang, Phys. Rev. Lett. **88**, 027201 (2001).

[76] A. Klümper, Z. Phys. B **91**, 507 (1993).

[77] S. Yamamoto, Phys. Rev. Lett. **75**, 3348 (1996).

[78] N. Kawakami et al., (2002), private communication.

[79] H. J. Schulz, Phys. Rev. Lett. **77**, 2790 (1996).

[80] D. J. Scalapino, Y. Imry, and P. Pincus, Phys. Rev. B **11**, 2042 (1975).

[81] Y. Yamashita, N. Shibata, and K. Ueda, Phys. Rev. B **58**, 9114 (1998).

[82] S. K. Pati and R. R. P. Singh, Phys. Rev. B **61**, 5868 (2000).

[83] P. Azaria, E. Boulat, and P. Lecheminant, Phys. Rev. B **61**, 12112 (2000).

[84] K. Majumdar and M. Mukherjee, cond-mat/0206359v2 (2002).

[85] I. Affleck, D. Gepner, H. J. Schulz, and T. Ziman, J. Phys. A **22**, 511 (1989).

[86] F. Naef, X. Wang, X. Zotos, and W. von der Linden, Phys. Rev. B **60**, 359 (1999).

[87] T. Mutou, N. Shibata, and K. Ueda, Phys. Rev. Lett. **81**, 4939 (1998).

[88] M. Rosenberg, *Untersuchungen zum phänomenologischen Ansatz der Dielektrizitätsfunktion polarer amorpher Systeme*, PhD thesis, Universität Dortmund, (2001).

[89] M. Böhm, H. Leschke, M. Henneke, V. S. Viswanath, J. Stolze, and G. Müller, Phys. Rev. B **49**, 417 (1994).

[90] K. Fabricius, U. Löw, and J. Stolze, Phys. Rev. B **55**, 5833 (1997).

[91] K. Fabricius and B. M. McCoy, Phys. Rev. B **57**, 8340 (1998).

[92] N. Bloembergen, Physica **15**, 386 (1949).

[93] P. G. de Gennes, J. Phys. Chem. Solids **4**, 223 (1958).

[94] R. M. Fye, Phys. Rev. B **33**, 6271 (1986).

Danksagung

An erster Stelle danke ich Herrn Prof. Dr. A. Klümper für die Betreuung der vorliegenden Arbeit. Seine stete Diskussionsbereitschaft und seine zahlreichen Anregungen haben in besonderer Weise zum schnellen Gelingen dieser Arbeit beigetragen.

Besonderer Dank gilt auch Prof. Dr. Giniyat Khaliullin, der die Arbeiten zu den Spin-Orbital Modellen anstieß und im weiteren Verlauf in zahlreichen Diskussionen wesentlich zu einer fruchtbaren Zusammenarbeit beitrug.

Bei Herrn Prof. Dr. W. Weber bedanke ich mich für die Bereitschaft, das Zweitgutachten zu übernehmen.

Weiterhin möchte ich mich bei Prof. Dr. B. Keimer, Andreas Kemper und Michael Bortz für die eine oder andere hilfreiche Diskussion bedanken.

Für das bereitwillige Korrekturlesen dieser Arbeit danke ich Michael Bortz und Frank Geuenich.

Schließlich danke ich auch allen Mitgliedern der Lehrstühle “Theoretische Physik I/II” für die kollegiale Arbeitsatmosphäre sowie für ihre ständige Hilfsbereitschaft.